

DISSERTATION

submitted to the
Combined Faculties for the Natural Sciences and for Mathematics
of the Ruperto-Carola University of Heidelberg, Germany
for the degree of
Doctor of Natural Sciences

Put forward by
Diplom Physics Behnam Nikoobakht
born in Behbahan-Iran

Oral examination: 7. July 2010

Theoretical Considerations for High-Precision Spectroscopy

Referees: Prof. Dr. Ulrich D. Jentschura
Priv.-Doz. Dr. Wolfgang Quint

Abstract

This thesis aims at investigating the possibilities of performing high-precision measurements of the $1S$ bound-electron g factor and analyzing the major systematic effects that influence high-precision spectroscopy in the ultraviolet and visible spectral bands. To measure the $1S$ bound-electron g factor of a ${}^4\text{He}^+$ ion confined in a Penning trap, two excitation schemes based on a double-resonance electronic excitation are proposed. The first excitation scheme relies on exciting the $1S_{1/2}(m_j = +1/2) \Leftrightarrow 2P_{3/2}(m_j = +3/2)$ transition in a ${}^4\text{He}^+$ ion using circularly polarized ultra-violet radiation. The excited state $2P_{3/2}(m_j = +3/2)$ relaxes to the ground state due to its short lifetime and emits a fluorescence photon. The Helium ion in the trap goes through this closed cycle and can be optically detected each time, because of the emitted photons. At the same time, a resonant microwave field produces spin-flip transitions causing quantum jumps between $1S_{1/2}(m_j = +1/2)$ and $1S_{1/2}(m_j = -1/2)$, which results in a pause of the charged particle emission in the closed cycle. These excitation processes yield the resonance spectrum of the Larmor frequency and lead to measuring the $1S$ bound-electron g factor of a Helium ion. In the second excitation scheme, coherent UV light excites a Helium ion stored in a Penning trap. This laser excitation drives the two-photon transition $1S-2S$. At a specific value of the trap magnetic field, the $2S_{1/2}(m_j = -1/2)$ and $2P_{1/2}(m_j = 1/2)$ states become degenerate. Applying an additional static electric field makes it possible to quench these two states and reduce the lifetime of the upper state $2S_{1/2}(m_j = -1/2)$ leading to a $2S$ electron decay to the ground state. The two-photon transition along with the quenching mechanism provides a closed cycle and results in the optical detection of a Helium ion in the trap. Similar to the first excitation setup, a microwave field is simultaneously radiated to the ground state $1S$ to induce the spin-flip transition yielding the resonance spectrum of the Larmor frequency. This excitation scheme, which benefits from the quenching mechanism together with the spin-flip transition, leads to the measurement of the $1S$ bound-electron g factor of the Helium ion. The latter excitation arrangement is also applied to a $1S-2S$ transition frequency determination via a Doppler-free two-photon transition in a Helium ion. In the excitation schemes above, due to the application of the dynamic and static electric fields, major systematic effects, *i.e.*, the AC and DC Stark shifts, are considered. We use this excitation scheme and extend it to a Rydberg state in the high- n region. In this regard, we calculate the AC Stark shift of high- n Rydberg states, which is the main systematic effect in the $1S-n'S$ transition frequency determination, $n' \rightarrow \infty$. Based on the findings of this study, the $1S$ bound-electron g factor in ${}^4\text{He}^+$ ions could be measured with an accuracy level of $10^{-12} \dots 10^{-13}$ in the future.

Zusammenfassung

In dieser Arbeit werden mögliche Hochpräzisionsmessungen des g -Faktors von gebundenen $1S$ -Elektronen untersucht und die bedeutendsten systematischen Effekte, die die Hochpräzisionspektroskopie im ultravioletten und sichtbaren Spektralband beeinflussen, analysiert. Um den g -Faktor des gebundenen $1S$ -Elektrons eines in einer Penning-Falle gefangenen $^4\text{He}^+$ -Ions zu messen, werden zwei Anregungsschemata, die auf einer doppelresonanten elektronischen Anregung aufbauen, vorgeschlagen. Das erste Anregungsschema beruht auf der Anregung des $1S_{1/2}(m_j = +1/2) \leftrightarrow 2P_{3/2}(m_j = +3/2)$ -Übergangs in einem $^4\text{He}^+$ -Ion durch zirkular polarisierte Ultraviolettstrahlung. Der angeregte Zustand $2P_{3/2}(m_j = +3/2)$ geht wegen seiner kurzen Lebenszeit in den Grundzustand über und strahlt dabei ein Fluoreszenzphoton ab. Das Heliumion durchläuft diesen Kreislauf in der Falle und kann dabei jedesmal aufgrund des abgestrahlten Photons nachgewiesen werden. Gleichzeitig löst ein resonantes Mikrowellenfeld eine Umdrehung des Spins aus, was Quantensprünge zwischen $1S_{1/2}(m_j = +1/2)$ und $1S_{1/2}(m_j = -1/2)$ bewirkt und eine Emissionspause des Kreislaufes zur Folge hat. Die Kombination dieser Prozesse ergibt das Resonanzspektrum der Larmorfrequenz und führt zur Messung des g -Faktors des gebundenen $1S$ -Elektrons eines Heliumions. In dem zweiten Anregungsschema regt UV-Licht ein in einer Penning-Falle gespeichertes Heliumion an. Diese Laseranregung treibt den Zweiphotonenübergang $1S-2S$. Bei einem bestimmten Wert des Magnetfelds der Falle werden die Zustände $2S_{1/2}(m_j = -1/2)$ und $2P_{1/2}(m_j = 1/2)$ entartet. Die Anwendung eines zusätzlichen statischen elektrischen Feldes ermöglicht es diese beiden Zustände zu mischen und die Lebenszeit des oberen Zustands $2S_{1/2}(m_j = -1/2)$ zu reduzieren; dies führt zu einem $2S$ -Elektronenzerfall in den Grundzustand. Der Zweiphotonenübergang zusammen mit dem Mischungsmechanismus bietet einen Kreislauf an und ergibt einen optischen Nachweis des Heliumions in der Falle. Wie im ersten Anregungsschema wird gleichzeitig ein Mikrowellenfeld auf den $1S$ -Grundzustand eingestrahlt um eine Umdrehung des Spins auszulösen. Dies ergibt das Resonanzspektrum der Larmorfrequenz. Dieses Anregungsschema, das von dem Mischungsmechanismus zusammen mit dem spinumdrehenden Übergang profitiert, führt zu der Messung des g -Faktors des gebundenen $1S$ -Elektrons eines Heliumions. Das zweite Anregungsschema wird ebenfalls auf eine Frequenzbestimmung des $1S-2S$ -Übergangs durch einen dopplerfreien Zweiphotonenübergang in einem Heliumion angewandt. In den obigen Anregungsschemata sind die bedeutendsten systematischen Effekte in Folge der Anwendung dynamischer und statischer elektrischer Felder, das heißt der AC- und der DC-Stark-Effekt, sorgfältig berücksichtigt. Wir verwenden das zweite Anregungsschema und erweitern es auf Rydbergzustände in dem Bereich großer n . Diesbezüglich berechnen wir den AC-Stark-Effekt auf Rydbergzustände mit großem n ; dies ist der bedeutendste systematische Effekt in der Frequenzbestimmung des $1S-n'S$ -Übergangs, $n' \rightarrow \infty$. Basierend auf den Ergebnissen dieser Arbeit kann der g -Faktor des gebundenen $1S$ -Elektrons in $^4\text{He}^+$ -Ionen mit einem Genauigkeitsgrad von $10^{-12} \dots 10^{-13}$ bestimmt werden.

Contents

1	Introduction	1
1.1	High-precision spectroscopy and reasons for more...	3
1.2	The motivations, goals and outlines of this thesis	5
2	AC Stark shift of the Hydrogen atom ...	9
2.1	Introduction	9
2.2	Classical approach	11
2.3	Treatment in the second quantization	14
2.3.1	Atom and quantized radiation interaction Hamiltonian	14
2.3.2	Quantized field approach	15
2.4	Evaluation of the dynamic Stark shift for $2P_{3/2}$	16
2.4.1	Analytical calculation	16
2.4.2	The numerical results	18
2.5	Partial summary and tentative concluding remarks	18
3	Dynamic polarizability and transition matrix elements ...	21
3.1	Introduction	21
3.2	Dynamic Stark shift of Rydberg states	23
3.2.1	General description	23
3.2.2	Evaluation of the AC Stark shift for Rydberg states	25
3.2.3	The results for S - S transitions	27
3.3	Photoionization cross section of Rydberg states	27
3.4	Two-photon transition matrix elements	32
3.4.1	Results for two-photon transitions	32
3.5	Partial summary and tentative concluding remarks	33
4	Dynamics of a charged particle in a Penning trap (the Geonium atom)	35
4.1	Introduction	35
4.2	Classical electrodynamics of the Geonium atom	39
4.3	Quantum motion of the Geonium atom	45
4.4	A real Penning trap	54
4.4.1	The invariance theorem	55
4.5	Determination of the true cyclotron frequency	58
4.5.1	Determination of the cyclotron frequency based on the invariance theorem	58
4.5.2	Determination of the cyclotron frequency based on one sideband frequency	59

4.6	Partial summary and tentative concluding remarks	60
5	Proposals for measurement of the bound-electron g factor	63
5.1	Introduction	63
5.2	Experimental and theoretical aspects of g factor	64
5.2.1	General description	64
5.2.2	Experimental setup for the measurement of the bound-electron g factor . .	66
5.2.3	Continuous Stern–Gerlach effect and the double-trap technique	68
5.2.4	Theoretical aspects of g factor	68
5.2.5	g factor of an electron in Hydrogen-like atom	71
5.3	Proposal I: Double-resonance excitation setup	72
5.4	Proposal II: Three-photon, double-resonance excitation setup	76
5.5	Proposal III	81
5.5.1	$1S$ – $2S$ transition frequency determination	81
5.5.2	Transition frequency determination of the ground to high-Rydberg states .	84
5.6	Partial summary and tentative concluding remarks	85
6	General conclusion	89
A	Quenching effect on metastable $2S_{1/2}(m_j = -\frac{1}{2})$ state	91
B	Breit–Rabi diagram	93
C	Calculation of relativistic and leading order QED contributions . . .	95
D	Relativistic and QED corrections for absolute . . .	99
E	Publication	103
E.1	W. Quint, B. Nikoobakht and U. D. Jentschura,	104
	Bibliography	111
	Acknowledgments	117

Chapter 1

Introduction

The scientific efforts that led to the birth of modern physics were predominantly accomplished in the first three decades of the 20th century. The majorities of the achievements were related to the special and general relativity theories and the creation of quantum mechanics. The latter still plays the most important role in providing new tools for describing atomic structures and dynamical processes in an exquisite detail.

The driving force for the actual creation of quantum mechanics was the need to understand the structure and properties of atoms. One of the most important movements was Bohr's 1913 paper on the Hydrogen atom, in which he introduced the concept of stationary energy states and quantum jumps along with the emission of monochromatic radiation. Bohr could explain the existence of atomic spectral lines and the exact form of the Hydrogen spectrum by combining the classical description of an electron moving in the field of a proton (planetary-like model) with principles that were unfounded by contemporary standards. Early attempts by Bohr, Sommerfeld and others led to the creation of "old" quantum theory, which could not describe physical phenomena completely. After proposing the fact that the energy quantization could be achieved by associating a wavelength with an electron, the "new" quantum theory was simultaneously established by Heisenberg and Schrödinger in 1924 and 1925, respectively.

During the development of quantum theory, the major features of the nucleus were described and the final constituent (*i.e.*, neutron) was discovered by Chadwick in 1932. The understanding of the nucleus and the creation of quantum mechanics made the foundations of atomic physics.

In 1928, Dirac proposed the relativistic quantum theory for an electron [1]. In his theory, he introduced an equation which was able to describe relativistically the wave behavior of 1/2-spin particle. In his equation, the magnetic moment of electron and electron spin were described in the framework of relativistic quantum theory. Moreover, his theory explained the fine structure splitting with a high precision. The fine structure of Hydrogen atom is influenced by the relativistic variation of electron mass with velocity and partly by the electron spin.

Another triumph of the Dirac theory was the prediction of the positron, which was detected by Carl Anderson few years later after the relativistic quantum theory was born.

According to the Dirac theory, the principal optical spectral line of Hydrogen atom has two components split by small fine-structure intervals. There were suggestions by Houston and Williams [2, 3] that a third component might exist, but the evidence of a possible substructure with a splitting much smaller than the width of the spectral line was hardly certain. In 1947, W. E. Lamb and R. C. Retherford paid careful attention to the proposal of Houston and Williams and showed experimentally that there was a third component in the fine-structure spectrum of Hydrogen, while according to the Dirac theory, these components were degenerate [4]. Their experimental method was based on a microwave technique with a resolution orders of magnitude better than the best achievable by optical spectroscopy at that time. [see Ref. [4]]. In the Lamb experiment, a beam of Hydrogen atoms in the metastable $2S_{1/2}$ state is induced by bombarding atomic Hydrogen, then an electron beam, which is parallel to the magnetic field collides with a beam of Hydrogen atoms in the metastable $2S_{1/2}$ state. After passing through an electric field, the metastable $2S_{1/2}$ states are quenched and no longer exist. In other words, they carry out transitions to the non-metastable $2P_{1/2}$ and $2P_{3/2}$ states and decay to the ground states $1S_{1/2}$ [4]. The observed splitting $2S_{1/2}-2P_{1/2}$ in the Hydrogen atom is 1057.77 MHz, which is in agreement with the theoretical value of the Lamb shift 1057.13 MHz [5]. The Lamb shift is thus a brilliant confirmation of relativistic theory of the electron that stimulates the development of Quantum electrodynamics (QED).

All these efforts carried out by W. E. Lamb, R. C. Retherford and I. I. Rabi paved the way for the creation of the Quantum electrodynamics (QED) by J. Schwinger, R. P. Feynman and others in 1940's. In QED, the Dirac theory of an electron is modified when one quantizes the electromagnetic radiation field. In QED framework, Lamb shift was accurately evaluated by using Feynman diagrams. In principle, the corresponding diagram of the Lamb shift representing the emission and re-absorption of the photon is calculated by using the expansion of the S-matrix theory. Later, the divergence difficulties appeared in the calculation of the diagram amplitudes were removed by H. Bethe, H. Kramers and others [5]. This method of calculation has been extended to the calculation of the other corrections such as vacuum polarization and so on. These processes made it possible to evaluate the Lamb shift in an excellent agreement with experimental results leading the recognition of QED as the most precise theory in Physics.

In recent years, more sensitive and rigorous tests of QED have been performed on systems such as a free electron and Hydrogen atom. The basic requirement for such experiments is to precisely confine the motion of atoms or ions. This is possible by using traps containing magnetic and quadrupole electric fields (or an oscillating electric field). This type of trap holds the charged particle almost indefinitely, which allows atomic spectroscopy with a very high resolution. This ability leads not only to testing the fundamental theories of QED but also measuring the fundamental atomic constants.

Due to development of various kinds of traps and advent of tunable continuous wave (cw) lasers, outstanding advances in the field of high resolution spectroscopy have been taken place. These developments make it possible to immensely increase the atomic spectroscopy resolution, resulting in an extension of spectroscopy from frequency to time domain and control of atom motion. Moreover, the generation of laser light has had enormous

effects on the nature of light matter interactions. The interaction of an intense laser light with matter (*e.g.*, Hydrogen atom) makes it possible to detect higher order radiation processes, such as multiphoton transitions. These multiphoton transitions in Hydrogen atom have yielded the most precise test of QED. For example, in 1975 Hänsch and coworkers observed the Doppler-free $1S-2S$ transition frequency to an accuracy of four parts 10^{13} [6]. Lamb shift obtained from the measured value of the $1S-2S$ transition frequency was in an excellent agreement with QED results.

In low energy tests of QED, comparison is carried out between the experimental and theoretical values of magnetic moment of the free and bound electron. The first measurement of the free-electron g factor¹ was performed by Rabi and Kusch. Their measurement resulted in a g factor which had a discrepancy of one percent relative to the Dirac value, $g = 2$. Several years later, H. Dehmelt carried out the same measurement and was able to reach a precision of three parts in per billion. This experiment was performed by detecting a single electron stored in a trap consisting of a static quadrupole electric and magnetic field (a Penning trap). The difference between the experimental value for the anomaly² and the predication of QED, as evaluated by T. Kinoshita, was found to be -270×10^{-12} [7]. Within this uncertainty, this result shows one the most rigorous low-energy test of QED.

1.1 High-precision spectroscopy and reasons for more accurate measurements

Often in the history of science, new structures and phenomena have been illuminated by high-precision measurements that revealed tiny deviations from the predictions of a previously accepted theory. This is particularly true in atomic spectroscopy, where increasing spectral resolution led to the observation of atomic fine structure and hyperfine structures, respectively. For example, an external magnetic and electric field exhibit Zeeman and DC Stark energy level structures, respectively. In the presence of an electromagnetic field, atomic energy levels give rise to the AC Stark energy level structures. More fine and delicate, QED effects explain to the Lamb shift. By pushing to even higher precision and resolution, we presumably reveal new phenomena. By examining such extremely fine structures, one can ask about the constancy of optical transition frequencies over time, an aspect related to the constancy of the fundamental constants themselves. In additions, at this delicate level of precision, possible asymmetries that may be existed between matter and antimatter can be revealed.

The main advantage of high-resolution spectroscopy of an atom is that it makes possible to investigate the confrontations between experiment and fundamental physical theories. Therefore, high-resolution spectroscopy is a suitable way to test the fundamental theories. There are at least two topics in a high-resolution spectroscopy that make it possible to check the validity of the fundamental theories. The first one is the precise absolute measurements

¹ g factor is the coupling constant of the spin to an external, homogenous magnetic field.

² Anomalous magnetic moment of electron is the deviation of g factor from the Dirac value 2.

between different transition frequencies in Hydrogen atoms. Due to interest in narrow atomic transitions, the $1S$ – $2S$ transition frequency measurement of Hydrogen atoms is one of the most intriguing candidates. The second one is a free- and bound- electron g -factor measurement. Over the past two decades, the accuracy level of these two values (*i.e.*, the $1S$ – $2S$ transition frequency and g factor) has been continuously improved both theoretically and experimentally. One may ask the following question: what can be learned from more accurate measurements of the $1S$ – $2S$ transition frequency and g factor? First, we answer to this question in the case of the $1S$ – $2S$ transition frequency. Testing the fundamental theory like QED, determining the fundamental constants such as Rydberg constant and Lamb shift are the reasons for improving the $1S$ – $2S$ transition frequency determination. The experimental values of the $1S$ Lamb shift obtained from the $1S$ – $2S$ transition frequency are 8172.6(7)MHz for a Hydrogen atom and 8183.7(6)MHz for a deuterium, which are in an excellent agreement with the theoretical (QED) results of 8173.03(9)MHz and 8184.08(12)MHz, respectively [8]. Moreover, the metrology of optical frequency in the $1S$ – $2S$ transition could be a base of the future atomic clocks, which benefits the $1S$ – $2S$ transition in a Hydrogen atom as an oscillator and the frequency comb as the clockwork.

In the case of free and bound-electron g factor, three reasons have been prescribed for obtaining a more accurate g factor. The first reason beyond g itself is an accurate calculation of the fine structure constant³ $\alpha = e^2/4\pi\epsilon_0\hbar$, which is also an important ingredient in the collection of fundamental constants. A Dirac point particle has $g = 2$ [9]. QED predicts that vertex corrections and vacuum polarization slightly increase this value. The result is an asymptotic series that relates g and α :

$$\frac{g}{2} = 1 + A_1\left(\frac{\alpha}{\pi}\right) + A_2\left(\frac{\alpha}{\pi}\right)^2 + A_3\left(\frac{\alpha}{\pi}\right)^3 + A_4\left(\frac{\alpha}{\pi}\right)^4 + \cdots + a_{\mu\tau} + a_{hadronic} + a_{weak} \quad (1.1)$$

According to the standard Model, hadronic and weak contributions are very small and believed to be well understood at the accuracy level needed. QED calculations produced exact answers for A_1 , A_2 , A_3 and a numerical value for A_4 and $a_{\mu\tau}$. Using the newly measured g in Eq. (1.1), α^{-1} is calculated to be 137. 035 999 070 (98) [0.71] ppb [10, 11]. The total uncertainty of 0.70 ppb is 10 times smaller than the value obtained from the most precise methods. In this investigation, α is measured from the mass ratios, optical frequencies, together with rubidium (Rb) or cesium (Cs) recoil velocities [10].

The second reason for a more accurate measurement of the g factor is to test QED. The most rigorous test of QED is comparing the measured and the calculated g factors. Due to the comparison of the measured anomalous magnetic moment of electron a for Cs and Rb, with the theoretical results obtained by Eq.(1.1), the discrepancies $\delta a_{Cs} = -7.9(9.3) \times 10^{-12}$ and $\delta a_{Rb} = 1.9(7.7) \times 10^{-12}$ were obtained [10, 11]. This insignificant difference indicates that quantum electrodynamics is tested more rigorously than it was envisaged by its pioneers. The third application of an accurate g factor relates to a measurement of the muon $g - 2$ as a way to search for physics beyond the standard model. The deviation of the muon

³The fine structure constant yields the strength of electromagnetic interaction.

g factor from the Dirac value is very small (one part in 800). This tiny deviation is originated from the muon's interactions with virtual particles. According to the Heisenberg uncertainty principle, the muon can emit and re-absorb photons, electrons, W and Z bosons⁴ and gluons⁵. This indicates that electromagnetic, strong and weak interactions have contributions in the muon g factor determination. In the framework of the standard model, the muon g factor is evaluated to a precision of 0.6 ppm (part per billion). A comparison of the measured and the calculated muon g factor provides a sensitive test of the standard model. If there is physics not taken into account in the current theory, such a new physics will affect the muon g factor, then the experimental results would not confirm the theory.

1.2 The motivations, goals and outlines of this thesis

Physicists have developed the high-precision frequency comb techniques to bridge large frequency differences in order to probe matter with a high precision. In view of this dramatic progress, the coherent radiation sources can be utilized in the laser spectroscopy of atomic transitions. In this thesis, a series of dynamical processes in the presence of these sources are systematically studied. These processes, that require high-precision spectroscopy setups, offer suitable platforms for the measurement of the bound-electron g factor and the optical frequency of $1S-2S$ transition. The motivation for this thesis is to apply an ultra-high precision atomic laser spectroscopy technique to determine the $1S$ bound-electron g factor and $1S-2S$ transition frequency in a Helium ion. In order to do a sound and an accurate spectroscopy measurement, the theoretical background is necessary to describe the underlying physics of interest.

There are two main objectives for this thesis. The first one is to develop pathways for high-precision determination of the $1S$ bound-electron g factor, $1S-2S$ transition frequency and $1S-n'S$ transition frequency, $n' \rightarrow \infty$ in the Helium ion. In doing so, we use properties of one-electron bound systems in combination with two atomic transitions, *i.e.*, Lyman- α and spin-flip transitions. This combination is used to examine certain properties of systematic effects that are related to the ultra-high-precision spectroscopy in UV and visible spectral regions. The second objective is to deal with a laser interaction with the Rydberg state in the high- n region and obtain the major systematic effects that are related to the $1S-n'S$ and $2S-n'S$, $n' \rightarrow \infty$ transitions.

In Chapter 2, the interaction of a Hydrogen-like atom in the presence of a circularly polarized laser light yielding AC Stark shift is handled via two different methods. The first method relies on time-dependent perturbation theory. The second one is relied on the quantum nature of the radiation field and the time-independent field operator. It is shown that both the classical treatment and the fully quantized approach give the same physical result in the limit of large occupation photon numbers. Subsequently, the dynamic Stark shift for the reference state $2P_{3/2}(m_j = 3/2)$ in $^4\text{He}^+$ ion in the presence of the circularly polarized laser light is calculated. We use the obtained numerical results in

⁴W and Z bosons are the elementary particles that mediate the weak interaction.

⁵Gluon is the elementary particle that mediates the strong interaction.

Chapter 5, where the dynamic Stark shift of reference state $2P_{3/2}(m_j = 3/2)$ serves as a major systematic effect in the proposed excitation arrangement related to the measurement of the bound-electron g factor in Helium ion.

In Chapter 3, based on the time-dependent perturbation theory, we study the Hydrogen-like Rydberg atom (ion) in the presence of a linearly polarized laser light driving transitions $1S-n'S$ and $2S-n'S$, $n' \rightarrow \infty$. Dynamic Stark shifts of initial and final states, as a major systematic effects in high-precision spectroscopy, are investigated. We also evaluate the corresponding two-photon transition amplitudes. All these calculations are performed in a unified formalism, *i.e.*, the Sturmian representation of the radial Green's function. This is followed by evaluating light frequency shift (AC Stark shift coefficients) in S.I. units and calculating the photoionization cross sections for high- n Rydberg state using two different methods. Due to introducing the Z -scaling for the AC Stark shift coefficients and the transition matrix elements, we are able to generalize these results to Helium ion. They serve as the major systematic effect in the proposed excitation arrangement for determination of the $1S-n'S$, $n' \rightarrow \infty$ two-photon transition frequency in Helium ion, which the excitation arrangement shall be introduced in the Chapter 5.

In Chapter 4, due to the significant application of a Penning trap in the measurement of a free and bound-electron g factor, dynamics of a charged particle (an ion) in the Penning trap is studied. We pay attention to the classical motion of a charged particle in the ideal trap. We consider motion of the charged particle in the Penning trap with and without an additional electric field in the framework of classical electrodynamics. We study the effect of an additional electric field on the charged particle stored in the trap. This additional electric field is responsible for the quenching mechanism in the excitation arrangement related to the $1S$ bound-electron g factor determination [see Chapter 5]. We deal with the quantum mechanical motion of a charged particle in the Penning trap. This investigation is performed based on two methods: (*i*) using the Schrödinger equation, (*ii*) using raising and lowering operators. The imperfections in a real Penning trap, which could be considered as systematic effects are discussed. The systematic effects influence on a free- and bound-electron g factor accuracy level, which is related to the thesis goal and is elaborated precisely in Chapter 5. The effect of imperfections on g factor accuracy level is dealt with by introducing the invariance theorem and one sideband frequency method, that have an extensive application in the highly precise measurement of bound-electron g factor.

In Chapter 5, the experimental setup for measuring bound-electron g factor, which is performed in a Penning trap is introduced. The theoretical aspects of the free- and bound-electron g factor are studied. We consider individual contributions to the $1S$ bound-electron g factor that are relevant at 10^{-12} level of accuracy. We propose two excitation arrangements to improve the accuracy level of $1S$ bound-electron g factor for spinless $^4\text{He}^+$ ion (nuclear spin $I = 0$) in comparison with the current accuracy level of bound-electron g factor. They are double-resonance, two-photon excitation arrangement and double-resonance, three-photon excitation arrangement. The excitation arrangements are based on the two simultaneous Lyman- α and spin-flip transitions among the Zeeman sub-levels of $^4\text{He}^+$ ion that lead to the detection of a charged particle in a Penning trap and

measuring the Larmor frequency of an electron. The major systematic effect, *i.e.*, AC Stark shift, which was handled in Chapters 2 and 3, in the excitation arrangements are calculated. The idea, double-resonance, three-photon excitation arrangement, can also be applied to $1S \Leftrightarrow 2S$ and $1S \Leftrightarrow n'S$, $n' \rightarrow \infty$ transition frequency determination.

Chapter 6 is reserved for the general conclusion.

Five appendixes are attached. In Appendix A, the quenching mechanism for the metastable $2S_{1/2}$ level of the helium ion, as implied by the magnetic-field-induced degeneracy with respect to the $2P_{1/2}$ level, is calculated. In Appendix B, the Breit-Rabi formula for the $2S_{1/2}$ and $2P_{1/2}$ levels is evaluated. The Breit-Rabi formula is necessary for an accurate calculation of the energy shifts in the magnetic fields of the trap. In Appendix C, we discuss the evaluation of the leading radiative and relativistic corrections to the bound-electron g factors for the atomic energy levels relevant to our investigation. The relativistic and QED corrections for absolute transition frequencies of ${}^4\text{He}^+$ are investigated in Appendix D. The publications due to this thesis are attached in Appendix E.

Chapter 2

AC Stark shift of the Hydrogen atom in a circularly polarized laser field

2.1 Introduction

It is well known that the physical properties of atoms can be modified by their interaction with an electromagnetic radiation [12]. For instance, the virtual emission and reabsorption of photons result in a shift of the atomic energy levels. This effect either occurs spontaneously (in the absence of a light source) causing to the Lamb shift, or is induced by an external light, which result into the so-called AC Stark shift. Classically, the AC Stark shift of the energy levels of hydrogen-like atom that is irradiated by an intense, nonresonant and monochromatic laser field can be evaluated in the framework of the time-dependent perturbation theory. In this classical picture, the Hydrogen-like atom and the laser field are described by the quantum and classical equations, respectively. The AC Stark shift can also be expressed in a framework relying on the fully quantized method, which concurs with the classical field description in the limit of high photon density [13].

The AC Stark shift is more generally named stimulated radiative corrections, as it is stimulated by the external electromagnetic field and are also dependent on the field intensity [14, 13]. This fact shows that in the case of monomode oscillating electric field, the AC Stark shift is nearly similar to the self-energy like formalism. As opposed to the self-energy like formalism, where all photon modes are unoccupied in the unperturbed state, in the AC Stark shift, there is one occupied mode of the photon field [12, 13]. In this chapter, we emphasize this important point that the AC Stark shift can be described in terms of the stimulated radiative correction.

Before description of the physics underlying the process of the disturbance of the atomic levels by an electromagnetic field, we would like to discuss shortly of the similarity and dissimilarities of the Stark effect in the laser field (*i.e.*, AC Stark shift) and the analogous in its stationary electric field (*i.e.*, DC Stark shift). As a similarity, DC and AC Stark shift are connected with dipole polarizability of atom in a stationary electric field and oscillating electric field, respectively. The corresponding shifts depend on the individual properties of

an atom, *i.e.*, eigenfunctions and eigenvalues. The differences between these two important issues are as follows: First, it is important to know that the energy is not conserved in a time-dependent field (AC Stark shift), but its conservation is valid in the stationary electric field (DC Stark shift). Second, the DC Stark shift is evaluated in the time-independent perturbation theory, while the AC Stark shift is formulated in time-dependent perturbation theory. Third, in the DC Stark shift, the perturbation of the nondegenerate bound atomic states only results into the splitting of energy levels. This splitting only depends on the strength of the electric field, but we have totally different situation in the AC Stark shift. The time-dependent Schrödinger equation of a quantum system (*e.g.*, an atom) in the presence of the periodic external perturbation $V = eE_z \sum_{i=1}^N z_i \cos \omega t$ with the period $T = 2\pi/\omega$ has obviously the solutions with the same period T . If we substitute the resulting ansatz

$$\psi(t) = e^{-(i/\hbar)\varepsilon t} \Phi_\varepsilon(t), \quad \Phi_\varepsilon(t+T) = \Phi_\varepsilon(t) \quad (2.1)$$

in the time-dependent Schrödinger equation $\partial\psi(t)/\partial t = H\psi(t)$, where $H = \sum_{i=1}^N H_i + V$, then we will reach an equation for the evaluation of the periodic function $\Phi_\varepsilon(t)$,

$$\left(H - i\hbar \frac{\partial}{\partial t}\right) \Phi_\varepsilon(t) = \varepsilon \Phi_\varepsilon(t). \quad (2.2)$$

If we assume that $\mathcal{H} = H - i\hbar \partial/\partial t$, then Eq. (2.2) is an eigenvalue equation. The corresponding eigenvalues and eigenfunctions are named quasi-energies and quasi-energies states or Floquet states, respectively. The Floquet states are a complete set. This indicates that any solution of the time-dependent Schrödinger equation can be expressed in terms of a superposition of the Floquet states with time-independent coefficients. The eigenstate ϕ_ε of the Hamiltonian \mathcal{H} is related to a whole group of eigenstates $\phi_\varepsilon e^{ik\omega t}$ with eigenvalues $\varepsilon + k\hbar\omega$, $k = 0, \pm 1, \pm 2, \dots$. These eigenstates are part of the Floquet state Eq. (2.1). The quasi-energy method, that is summarized in Eqs. (2.1) and (2.2), has been applied to the dynamics of a monochromatic laser interaction with atoms. Due to this interaction, an initial nondegenerate state is transformed into the Floquet states in which the separation between the adjacent quasi-energy levels is equal to the photon energy of the radiation field $\hbar\omega$. Moreover, the entire quasi-energy spectrum is displaced with relation to the initial unperturbed level. If the population of only one quasi-energy level is taken place, this leads to the AC Stark shift of that particular atomic level.

In this chapter, we focus on the off-resonant, two-photon transition in which the frequency of the incident radiation is close to half of the atomic transition frequency as demonstrated in Ref. [13]. Our aim is to calculate the AC Stark shift due to the interaction of the Hydrogen-like atom with the circularly polarized laser light as the authors performed in the case of the linearly polarized laser light in Ref [13]. We assume that the laser light is monochromatic, implying that the finite band width effect of the laser light and the result dependence on the laser power are automatically negligible [15, 16, 17].

This chapter is organized as follow: in Sec. 2.2, the dynamic Stark shift for Hydrogen-like atom in the presence of the circularly polarized laser light is dealt with in the framework of time-dependent perturbation theory. As mentioned, we apply the semiclassical description, in which Hydrogen-like atom is described in the framework of the quantum mechanics

and the laser field is characterized in the framework of the classical mechanics. In Sec. 4.3, a fully quantized-field treatment is employed, which goes to a classical result when the photon number in the laser mode is large enough. In Sec. 2.4, for an important example, the dynamic Stark shift of the reference state $2P_{3/2}(m_j = 3/2)$ is evaluated by using the analytical result obtained in Sec. 2.2. The corresponding numerical results serve as the major systematic effect in an excitation arrangement of g factor determination, which will be introduced in Chapter. 5. Finally, the partial summary and tentative concluding remarks are presented in Sec. 2.5.

2.2 Classical approach

Consider a Hydrogen-like atom (ion) that is adiabatically embedded in the remote past and future in circularly polarized laser field [18]

$$\mathbf{E}(t) = \frac{\mathcal{E}_L e^{-\epsilon|t|}}{\sqrt{2}} [\mathbf{e}_x \cos(\omega_L t) + \mathbf{e}_y \sin(\omega_L t)]. \quad (2.3)$$

We have assumed that the field energy density is normalized as \mathcal{E}_L^2 . ϵ is an infinitesimal damping parameter [see, *e.g.*, Ref. [13]]. Here, we have adopted the dipole approximation which implies that the wavelength of the radiation is far greater than the atom size. The evolution of the unperturbed Hamiltonian of the atom H_0 with the eigenfunction $|\phi\rangle$ in the monochromatic laser field is determined by

$$i\hbar \frac{\partial \psi}{\partial t} = H\psi, \quad (2.4)$$

where the Hamiltonian of the atom + laser reads

$$H = H_0 + V(x, y, t). \quad (2.5)$$

In Eq. (2.5), the unperturbed Hamiltonian of the atom H_0 is,

$$H_0 = \frac{\mathbf{p}^2}{2m_e} - \frac{Ze^2}{4\pi\epsilon_0 r}, \quad (2.6)$$

and $V(x, y, t)$ describes the interaction of the Hydrogen-like atom in the presence of the circularly polarized laser light (in the length gauge),

$$V(x, y, t) = e^{-\epsilon|t|} [V(x) \cos(\omega_L t) + V(y) \sin(\omega_L t)], \quad (2.7)$$

with $V(x) = -\frac{e\mathcal{E}_L x}{\sqrt{2}}$ and $V(y) = -\frac{e\mathcal{E}_L y}{\sqrt{2}}$. In this investigation, we shall take into account only the solutions of Eq. (2.4) corresponding the adiabatic switching of the perturbation $V(x, y, t)$ at the remote past and future ($t \rightarrow \pm\infty$). This indicates that the solution of Eq. (2.4) turns at $t \rightarrow \pm\infty$ into the eigenstate of the unperturbed Hamiltonian H_0 , which for simplicity shall be assumed to be nondegenerate.

To describe the effect of the off-resonance perturbation by a time-dependent electric field Eq. (2.3) on the reference state $|\phi\rangle$ of the bare atom, we use the interaction picture, in which the field-atom interaction is represented as

$$V_I(x, y, t) = e^{\frac{i}{\hbar} H_0 t} V(x, y, t) e^{-\frac{i}{\hbar} H_0 t}. \quad (2.8)$$

From which we obtain the expansion of the time evolution operator in the interaction picture [19]

$$\begin{aligned} U_I(x, y, t) &= T \exp \left[-\frac{i}{\hbar} \int_{-\infty}^t U_I(\tau) d\tau \right] = \\ &= 1 - \frac{i}{\hbar} \int_{-\infty}^t dt' V_I(x, y, t') + \left(\frac{-i}{\hbar} \right)^2 \int_{-\infty}^t dt' \int_{-\infty}^{t'} dt'' V_I(x, y, t') V_I(x, y, t'') + \dots, \end{aligned} \quad (2.9)$$

where T is the time-ordering operator. Due to the laser-atom interaction, the reference state $|\phi\rangle$ evolves into a time dependent atomic state $|\psi_I(t)\rangle$,

$$|\psi_I(x, y, t)\rangle = U(x, y, t) |\psi(x, y, t = -\infty)\rangle = U(x, y, t) |\phi\rangle. \quad (2.10)$$

Since the interaction is weak compared to the Coulomb field of atom, we may expand $|\psi_I\rangle$ in a complete set $\{|m\rangle\}$ of eigenstates of H_0 ,

$$|\psi_I\rangle = \sum_m c_m(t) |m\rangle, \quad (2.11)$$

where $c_m(t) = \langle m | \psi_I(t) \rangle$ are expansion coefficients, that satisfy the initial condition $c_\phi(-\infty) = 0$, $c_m(-\infty) = 0$ ($m \neq \phi$). To obtain the energy shift and ionization rate of the reference state, we calculate the projection

$$c_\phi(t) = \langle \phi | \psi_I(t) \rangle = \langle \phi | U_I(r, t) | \phi \rangle \quad (2.12)$$

We now substitute Eqs. (2.7), (2.8) and (2.10) into Eq. (2.12). Since $\langle \phi | x | \phi \rangle = \langle \phi | y | \phi \rangle = 0$, the expansion may be taken up to the second order,

$$c_\phi(t) = 1 - \frac{1}{\hbar^2} M, \quad (2.13)$$

where

$$\begin{aligned} M &= \int_{-\infty}^t dt' \int_{-\infty}^{t'} \langle \phi | V_I(x, y, t') V_I(x, y, t'') | \phi \rangle \\ &= \sum_m \int_{-\infty}^t dt' \int_{-\infty}^{t'} dt'' \langle \phi | V_I(x, y, t') | m \rangle \langle m | V_I(x, y, t'') | \phi \rangle. \end{aligned} \quad (2.14)$$

The sum counts all bound and continuum states. Since the time dependence of the potentials is harmonic, the integrations can be easily worked out, yielding

$$M = -\frac{\hbar}{4i} \sum_{m,\pm} \frac{e^{2\epsilon t}}{2\epsilon} \left[\frac{\langle \phi | V(x) | m \rangle \langle m | V(x) | \phi \rangle}{E_\phi - E_m \pm \hbar\omega_L + i\hbar\epsilon} + \frac{\langle \phi | V(y) | m \rangle \langle m | V(y) | \phi \rangle}{E_\phi - E_m \pm \hbar\omega_L + i\hbar\epsilon} \right. \\ \left. \pm i \frac{\langle \phi | V(x) | m \rangle \langle m | V(y) | \phi \rangle}{E_\phi - E_m \pm \hbar\omega_L + i\hbar\epsilon} \mp i \frac{\langle \phi | V(y) | m \rangle \langle m | V(x) | \phi \rangle}{E_\phi - E_m \pm \hbar\omega_L + i\hbar\epsilon} \right] \quad (2.15)$$

Inserting this result into Eq. (2.13), and considering

$$\frac{\partial}{\partial t} \ln c_\phi(t) = -\frac{i}{4\hbar} \sum_{m,\pm} \left[\frac{\langle \phi | V(x) | m \rangle \langle m | V(x) | \phi \rangle}{E_\phi - E_m \pm \hbar\omega_L + i\hbar\epsilon} + \frac{\langle \phi | V(y) | m \rangle \langle m | V(y) | \phi \rangle}{E_\phi - E_m \pm \hbar\omega_L + i\hbar\epsilon} \right. \\ \left. \pm i \frac{\langle \phi | V(x) | m \rangle \langle m | V(y) | \phi \rangle}{E_\phi - E_m \pm \hbar\omega_L + i\hbar\epsilon} \mp i \frac{\langle \phi | V(y) | m \rangle \langle m | V(x) | \phi \rangle}{E_\phi - E_m \pm \hbar\omega_L + i\hbar\epsilon} \right], \quad (2.16)$$

here $e^{2\epsilon t}$ has been replaced by 1. The solution of Eq. (2.16) is

$$c_\phi(t) = e^{-\frac{i}{\hbar} \Delta E_{AC}(\phi)t}, \quad (2.17)$$

where we have defined the dynamic stark shift $\Delta E_{AC}(\phi)$ of the reference state $|\phi\rangle$,

$$\Delta E_{AC}(\phi) = \frac{1}{4} \sum_{m,\pm} \left[\frac{\langle \phi | V(x) | m \rangle \langle m | V(x) | \phi \rangle}{E_\phi - E_m \pm \hbar\omega_L + i\hbar\epsilon} + \frac{\langle \phi | V(y) | m \rangle \langle m | V(y) | \phi \rangle}{E_\phi - E_m \pm \hbar\omega_L + i\hbar\epsilon} \right. \\ \left. \pm i \frac{\langle \phi | V(x) | m \rangle \langle m | V(y) | \phi \rangle}{E_\phi - E_m \pm \hbar\omega_L + i\hbar\epsilon} \mp i \frac{\langle \phi | V(y) | m \rangle \langle m | V(x) | \phi \rangle}{E_\phi - E_m \pm \hbar\omega_L + i\hbar\epsilon} \right]. \quad (2.18)$$

Considering Eq. (2.11), the wavefunction of the system in the Schrödinger picture reads

$$|\psi(t)\rangle = e^{-\frac{i}{\hbar} H_0 t} |\psi_I(t)\rangle = e^{-\frac{i}{\hbar} H_0 t} \left[c_\phi(t) |\phi\rangle + \sum_{m \neq \phi} c_m(t) |m\rangle \right]. \quad (2.19)$$

Thus we obtain the projection

$$\langle \phi | \psi(t) \rangle = e^{-\frac{i}{\hbar} [E_\phi + \Delta E_{AC}(\phi)]t}, \quad (2.20)$$

which shows the perturbative effect on the time-evolution of the reference state. In view of the fact that $\Delta E_{AC}(\phi)$ is generally complex, we may define the energy shift and ionization rate of the reference state $|\phi\rangle$:

$$\Delta E_\phi = \text{Re} [\Delta E_{AC}(\phi)], \\ \gamma_\phi = -\frac{2}{\hbar} \text{Im} [\Delta E_{AC}(\phi)]. \quad (2.21)$$

They respectively arise from the fact that the atomic system may exchange virtual and real photons with the laser field in the course of interaction. Introducing the complex coordinates

$$x_{+1} = -\frac{1}{\sqrt{2}}(x + iy), \quad x_{-1} = \frac{1}{\sqrt{2}}(x - iy), \quad (2.22)$$

we may cast the dynamic Stark shift of Eq. (2.18) into a more concise form:

$$\Delta E_{\text{AC}}(\phi) = -\frac{e^2 \mathcal{E}_L^2}{4} \sum_{\pm} \langle \phi | x_{\mp 1} \frac{1}{H_0 - E_{\phi} \pm \hbar \omega_L} x_{\pm 1} | \phi \rangle. \quad (2.23)$$

Here we have used the closure relation over the spectrum of H_0 . If we define the dynamic polarizability

$$P_{\omega_L}(\phi) = \sum_{\pm} \langle \phi | x_{\mp 1} \frac{1}{H_0 - E_{\phi} \pm \hbar \omega_L} x_{\pm 1} | \phi \rangle, \quad (2.24)$$

then the dynamic Stark shift reads

$$\Delta E_{\text{AC}}(\phi) = -\frac{1}{4} e^2 \mathcal{E}_L^2 P_{\omega_L}(\phi) = -\frac{e^2}{2\varepsilon_0 c} I_L P_{\omega_L}(\phi), \quad (2.25)$$

where $I_L = c\varepsilon_0 \mathcal{E}_L^2/2$ is the intensity of the laser field. Eq. (2.24) can be interpreted as the sum of the amplitudes of two-photon processes. In the first process the atom absorbs one quantum and goes into a virtual state (the term involving $-$ sign in the denominator) and after emitting the same $\hbar \omega_L$ quantum it returns to the initial state. In the second process (the term involving $+$ sign in the denominator) the atom emits the $\hbar \omega_L$ quantum first and goes into the virtual state and after absorbing the same quantum, it returns to the initial state. The result is the shift of an energy level.

2.3 Treatment in the second quantization

In the preceding section, we dealt with the interaction between Hydrogen-like atomic energy levels and the electromagnetic radiation and assumed that the field to be classical. In this section, in view of light being a photon field, we discuss the interaction of the quantized radiation field with a Hydrogen-like atom. As we explain later, the atom + laser system can be described by a perturbed Hamiltonian. Note that we choose the length gauge [see Ref. [20]] and take the dipole approximation into account throughout the calculations.

2.3.1 Atom and quantized radiation interaction Hamiltonian

The interaction of a monochromatic laser mode of angular frequency ω_L with a Hydrogen-like atom can be formulated in a general way [see *e.g.*, Ref. [18, 21]]. One can characterize the Hamiltonian corresponding to the atom + laser system in terms of three parts, *i.e.*,

$$H_I = H_0 + \hbar \omega_L a_L^\dagger a_L + H_L, \quad (2.26)$$

where the first two terms are the Hydrogen-like atom H_0 and the quantized field Hamiltonians, respectively. In Eq. (2.26), H_0 reads

$$H_0 = \frac{\mathbf{p}^2}{2m_e} - \frac{Ze^2}{4\pi\epsilon_0 r} = \sum_m |m\rangle\langle m|, \quad (2.27)$$

where $|m\rangle$ represents a complete set of atomic energy eigenstates including both the discrete and continuum region of the spectrum (m_e and e are electron mass and charge, respectively). Since we restrict ourselves to a single-mode field with the frequency ω_L , the corresponding Hamiltonian of the laser field can be written in terms of the creation and annihilation operators a_L^\dagger and a_L , respectively. The corresponding eigenstates are called Fock states [21]. Note that the energy eigenvalues are discrete, in contrast to the classical electromagnetic theory, where the energy is continuous.

The last part of the Eq. (2.26) denotes the perturbed term of the Hamiltonian which is responsible for the interaction between a Hydrogen-like atom and the monomode electromagnetic radiation. In the framework of the length gauge and dipole approximation, this term H_L reads

$$H_L = -e\mathbf{r} \cdot \mathbf{E}. \quad (2.28)$$

In the following, without the loss of generality, we concentrate on a circularly polarized field. Therefore, H_L reads

$$H_L = -e\varepsilon_L \left[-x_{+1}a_L + x_{-1}a_L^\dagger \right], \quad (2.29)$$

Where $\varepsilon_L = \sqrt{\hbar\omega_L/2\varepsilon_0\mathcal{V}}$, \mathcal{V} is the normalization volume and x_{+1} and x_{-1} are given in Sec. 2.2 [see Eq. (2.22)]. Eq. (2.22) indicates that $x_{+1}^\dagger = -x_{-1}$ and $x_{-1}^\dagger = -x_{+1}$, *i.e.*, Hamiltonian H_L is hermitian.

The Hamiltonian H_L represented by Eq. (2.29) may describe two physical processes. In the first one, the atom absorbs a photon of the laser field and jumps to the upper energy level (the first term in Eq. (2.29)), while the second one describes the opposite process [the second term in Eq. (2.29)].

2.3.2 Quantized field approach

We are now in a position to discuss the interaction between circularly polarized laser light and the Hydrogen-like atom from the quantum nature point of view of the radiation field by using Eqs. (2.26) and (2.29). Working in the Schrödinger picture, perturbation theory leads to the second-order energy shift of the unperturbed eigenstate $|\phi, n_L\rangle$:

$$\begin{aligned} \Delta E_{AC}(\phi) &= \sum_m \left[\frac{\langle \phi, n_L | H_L | m, n_L - 1 \rangle \langle m, n_L - 1 | H_L | \phi, n_L \rangle}{E_\phi + n_L \hbar\omega_L - (E_m + (n_L - 1)\hbar\omega_L)} \right. \\ &\quad \left. + \frac{\langle \phi, n_L | H_L | m, n_L + 1 \rangle \langle m, n_L + 1 | H_L | \phi, n_L \rangle}{E_\phi + n_L \hbar\omega_L - (E_m + (n_L + 1)\hbar\omega_L)} \right] \\ &= \frac{e^2 \hbar\omega_L}{2\varepsilon_0 \mathcal{V}} \sum_m \left[\frac{\langle \phi | x_{-1} | m \rangle \langle m | x_{+1} | \phi \rangle}{E_\phi - E_m + \hbar\omega_L} n_L + \frac{\langle \phi | x_{+1} | m \rangle \langle m | x_{-1} | \phi \rangle}{E_\phi - E_m - \hbar\omega_L} (n_L + 1) \right] \end{aligned} \quad (2.30)$$

In nonrelativistic quantum mechanics, the classical description is trustworthy whenever the noncommutativity of dynamical variables is unimportant [see, *e.g.*, textbook [22]]. Likewise, in the quantum theory of radiation, if we could ignore the right-hand-side of $[a_L, a_L^\dagger] = 1$ then we would return to the classical description. Due to the proportionality of the nonvanishing matrix elements of a_L and a_L^\dagger to the occupation number $\sqrt{n_L}$, the classical description Eq. (2.25) can be obtained again from Eq. (2.30) in the limit of a large occupation number. In other words, in the classical limit, $n_L \rightarrow \infty$, $\mathcal{V} \rightarrow \infty$, whereas $n_L/\mathcal{V} = \text{const}$, Eq. (2.30) becomes

$$\Delta E_{\text{AC}}(\phi) = -\frac{e^2 n_L \hbar \omega_L}{2\varepsilon_0 \mathcal{V}} P_{\omega_L}(\phi), \quad (2.31)$$

where $P_{\omega_L}(\phi)$ is given by Eq. (2.24). Comparing Eq. (2.31) with the classical result Eq. (2.25), we find

$$I_L = wc, \quad (2.32)$$

where

$$w = \frac{n_L \hbar \omega_L}{\mathcal{V}} \quad (2.33)$$

is the energy density of the field in the quantum version.

2.4 Evaluation of the dynamic Stark shift for $2P_{3/2}$

This section is devoted to the evaluation of the dynamic Stark shift for the reference state $2P_{3/2}$ in Hydrogen-like atom. In Chapter 5, as we shall introduce, in the excitation arrangement related to the bound-electron g factor measurement, a circularly polarized laser light drives transition between $1S_{1/2}(m_j = +1/2)$ and $2P_{3/2}(m_j = +3/2)$ states [see Sec. 5.3 and Fig. 5.4]. Due to the shift of $2P_{3/2}(m_j = +3/2)$ state in the presence of the circularly polarized laser light, AC Stark shift of the reference state $2P_{3/2}(m_j = +3/2)$ serving as a major systematic effect in the proposed excitation arrangement for bound-electron g factor measurement must be calculated.

2.4.1 Analytical calculation

In this section, we try to obtain analytical solution for the dynamic Stark shift of the reference state $2P_{3/2}(m_j = +3/2)$. To do so, one has to calculate the matrix element appeared in Eq. (2.24). The calculation method is based on the Sturmian representation of the radial Green's function for Hydrogen-like atom described in the Chapter 3.

The starting point of the calculation is to calculate the dipole polarizability in Eq. (2.24). In other words, the following matrix element has to be evaluated,

$$M = \left\langle \phi \left| x_{-1} \frac{1}{H_0 - E_\phi + \hbar \omega_L} x_{+1} \right| \phi \right\rangle. \quad (2.34)$$

One can divide Eq. (2.34) in two angular and radial components, *i.e.*,

$$M = M_{l'=2}^{\text{ang}} M_{l'=2}^{\text{rad}}, \quad (2.35)$$

where

$$\begin{aligned} M_{l'=2}^{\text{rad}} &= \int_0^\infty r_1^3 r_2^3 R_{21}^*(r) R_{21}(r) g_2(r_1, r_2, \eta), \\ M_{l'=2}^{\text{ang}} &= -\frac{18}{25}. \end{aligned} \quad (2.36)$$

In this case, the indexes l' and m' , appeared in Eq. (2.36), refer to the possible angular momentum and magnetic quantum numbers of the virtual intermediate state. The D and S states are possible intermediate states. In this calculation, due to Hydrogen-like atom interaction with a circularly polarized laser light, the only possible intermediate state is D states. $g_l(r_1, r_2, \eta)$ will be defined in Chapter 3 [see Eq. (3.8)]. The dimensionless parameter η , chosen such that for the eigenstate reference state $|\phi\rangle$ of H_0 with principle quantum number n we have $\eta = nt$. The parameter t reads [23]

$$t = \left(1 \pm \frac{2n^2\omega}{(Z\alpha^2)m_e}\right)^{-1/2}, \quad (2.37)$$

where α and m_e refer to the fine-structure constant and the electron mass, respectively. Putting Eq. (3.8) in Eq. (2.36), the radial part of the matrix element reads

$$M_{l'=2}^{\text{rad}}(t) = \frac{m_e}{12\hbar^2 a_B^{10} t^5} \sum_{k=0}^{\infty} \frac{k!}{(k+5)!(k+3-2t)} \times \left| I_{l'=2} \right|^2, \quad (2.38)$$

where $I_{l'=2}$ is

$$I_{l'=2} = \int_0^\infty r^6 e^{-\frac{1+t}{2a_B t} r} L_k^5\left(\frac{r}{a_B t}\right). \quad (2.39)$$

By using Eq. (3.16), one can find the result of Eq. (2.39) as follows:

$$I_2 = \frac{768 a_B^7 t^7}{(1+t)^7} \frac{(k+5)!}{k!} {}_2F_1\left(-k, 7, 6, \frac{2}{1+t}\right). \quad (2.40)$$

Therefore, $M_{l'=2}^{\text{rad}}$ reads

$$M_{l=2}^{\text{rad}}(t) = m a_0^4 \left[\frac{16t^2 \chi_2(t)}{3(t-1)^7(t+1)^5} - \frac{2^{16} t^{11} (4t^2 - 1)}{3(t^2 - 1)^7} {}_2F_1\left(1, -2t, 1 - 2t, \left(\frac{1-t}{1+t}\right)^2\right) \right], \quad (2.41)$$

where ${}_2F_1$ is designated for Hypergeometric function and $\chi_2(t)$ is

$$\begin{aligned} \chi_2(t) &= -45 + 90t + 165t^2 - 420t^3 - 174t^4 + \\ &\quad + 768t^5 - 34t^6 - 700t^7 - 37t^8 - 1274t^9 + 4733t^{10}. \end{aligned} \quad (2.42)$$

Table 2.1: Dynamic Stark shift coefficients β_{AC} and ionization coefficients β_{ioni} for $1S_{1/2}(m_j = +1/2) \Leftrightarrow 2P_{3/2}(m_j = +3/2)$ (on two-photon resonance) in nonrelativistic dipole approximation, evaluated for nuclear charge number $Z = 1$ and infinite nuclear mass based on Eqs. (2.24-2.25).

Process	$\beta_{AC}(2P_{3/2})[\text{Hz}(\text{W}/\text{m}^2)^{-1}]$	$\beta_{\text{ioni}}(2P_{3/2})[\text{Hz}(\text{W}/\text{m}^2)^{-1}]$
$1S_{1/2} \Leftrightarrow 2P_{3/2}$	1.8674×10^{-6}	6.35232×10^{-6}

In Eq. (2.41), the following contiguous relations for Hypergeometric function are employed [24]:

$$\begin{aligned}
 {}_2F_1(a, b, c, z) &= {}_2F_1(b, a, c, z) \\
 [b - 1 - (c - a - 1)z]F + (c - b)F(b - 1) - (c - 1)(1 - z)F(c - 1) &= 0 \\
 (c - b - 1)F + bF(b + 1) - (c - 1)F(c - 1) &= 0
 \end{aligned} \tag{2.43}$$

Where F denotes ${}_2F_1(a, b, c, z)$. $F(b \pm 1)$ and $F(c \pm 1)$ stand for ${}_2F_1(a, b \pm 1, c; z)$ and ${}_2F_1(a, b; c \pm 1; z)$, respectively.

2.4.2 The numerical results

The non-relativistic numerical results of the dynamic Stark shift for Hydrogen-like atom based on Eqs. (2.24) and (2.25) are shown in Table 2.1. The Z -scaling of the dynamic Stark shift coefficients (β_{AC} and β_{ioni}) enables us to generalize the results in Table 2.1 to any Hydrogen-like atoms (ions) such as ${}^4\text{He}^+$ (see Chapter 3 for more details about Z -scaling of the dynamic Stark shift).

$$\beta_{\text{ioni}}(Z) = \frac{1}{Z^4} \beta_{\text{ioni}}(Z = 1). \tag{2.44}$$

The results shown in Table 2.1 are for Hydrogen atom. According to the Eq. (2.44), if we put $Z = 2$, the corresponding results related Helium ion in the presence of a circularly polarized laser light will be obtained. These numerical results play as the major systematic effect in the excitation arrangement related to the bound-electron g factor determination, that will be introduced in Sec. 5.3.

Finally, we have taken notice of an ionization cross section for this transition for any Hydrogen-like atom that is

$$\sigma_{\text{ioni}} = \frac{1}{Z^2} 6.52536 \times 10^{-6} \text{ cm}^2. \tag{2.45}$$

2.5 Partial summary and tentative concluding remarks

In this chapter, the non-relativistic interaction of a Hydrogen atom or Hydrogen-like atom with a circularly polarized laser light was examined from two different points of view,

leading to two analytical expressions for the dynamic Stark shift [see Eqs. (2.25) and (2.31)]. The first was obtained via the classical method, which relied crucially on the assumption of an adiabatic vanishing of the source as $|t| \rightarrow \infty$ [see Eq. (2.3)] in the framework of time-dependent perturbation theory [see sec. 2.2]. The second treatment was described in the framework of the quantum nature of the radiation field, based on time-independent field operators [see sec. 2.3]. In the limit of a large occupation number of the laser mode, these two derivations are equivalent to each other [see Eqs. (2.25) and (2.31)]. We have found that the AC Stark shift is a complex quantity. The origin of this finding is that each initially bound state can couple to and decay into continuum states for sufficiently large n , *i.e.*, by coupling to a sufficient large number of photons.

If the sum over virtual modes of the photons is limited to a single mode of an electromagnetic field, it is safe to conclude that the AC Stark shift has a similar structure as the self-energy like formalism. This fact indicates that Eq. (2.30) can be interpreted as a stimulated radiative correction [12].

In Sec. 2.4, as an application of Eq. (2.25), the dynamic Stark shift of the reference state $2P_{3/2}(m_j = 3/2)$ for ${}^4\text{He}^+$ ion in the presence of the circularly polarized laser light was obtained. These results were listed in Table 2.1 and the ionization of the Helium ion taking place via channel $2P_{3/2} \Rightarrow \varepsilon D_{5/2}$ was evaluated. For this channel, the ionization cross section was also obtained [see Eq. (2.45)]. The corresponding numerical results serve as a major systematic effect in the proposed excitation arrangement of the bound-electron g factor, which will be introduced in Sec. 5.3.

Chapter 3

Dynamic polarizability and transition matrix elements of high- n Rydberg atoms

3.1 Introduction

The comparison between the experimental and theoretical values of the g factor plays an important role for examining the most precise theory in physics, *i.e.*, quantum electrodynamics (QED). Moreover, there is another tool to test QED: the two-photon transitions in a Hydrogen-like atom. Like the g factor, the comparison of the theoretical results with the experimental ones are the basis for the touchstone of quantum electrodynamics. In addition, two-photon transitions in Hydrogen-like atoms can be utilized for more precise determinations of the fundamental constants in physics such as the Rydberg constant [see Refs. [25, 26, 16, 27]].

In order to deal with high-precision spectroscopy, one has to know about the major systematic effects, which can improve the accuracy levels of the measured quantities. The dynamic Stark shift induced by the interaction of laser light with a Hydrogen-like atom can be considered as the dominant systematic effect along with the saturation effect in high-precision spectroscopy experiments [16]. Due to the interaction between the laser light and the atom, one can observe the metastasis of the atomic energy levels. Experimentally, this shift can not be suppressed and we need a very precise study on understanding the aforementioned physical effect, which may broaden or shift the spectral lines [16, 15, 17]. Consequently, interest has been directed towards the interaction between time-varying fields and Hydrogen-like atoms giving a non-vanishing second-order shift in the energy levels or spectral lines [see *e.g.*, Ref. [13]].

Recently, many attempts have been done in order to compute the dynamic Stark shift and two-photon transition matrix elements and deal with the absorption spectrum in two-photon resonance spectroscopy for $1S-n'S$ and $2S-n'S$, ($n' \leq 20$) for Hydrogen-like atoms [16, 14, 27]. It is important to generalize this study for a highly excited Rydberg

state, *i.e.*, $n' \rightarrow \infty$, and evaluate the dynamic Stark shift and two-photon transition matrix elements for this important case. Similar studies related the Lamb shift and Bethe logarithms of highly excited Rydberg states in a Hydrogen atom were performed by others [see *e.g.*, Refs. [28, 29, 30, 31, 32]]. Our motivations for this investigation are originated from the fact that the atomic structure can be apprehended relatively simple and systematically if one electron performs a transition to a highly excited state in the presence of an external field while the rest of electrons are considered to be more tightly bound to the atomic nucleus. As a result, this case accords asymptotically to a one-electron problem in the presence an attractive Coulomb potential. In addition, the highly excited Rydberg states have long lifetime allowing for high spectral resolution.

In the current survey, the dynamic Stark shift and two-photon transition matrix elements for $1S-n'S$ and $2S-n'S$ transitions, $n' \rightarrow \infty$ are investigated in a unified treatment. The results are compiled in SI units for the convenience of experimentalists. The dependency of the nuclear charge Z is taken into account in our results, so that they can be readily utilized for the other light Hydrogen-like atoms. The $n'S$ state $n' \rightarrow \infty$ is envisaged as an excited state of a Hydrogen-like atom driven by a linearly polarized laser field on two-photon resonance with the $1S-n'S$ transition $n' \rightarrow \infty$. If the absorption of an additional photon takes place, the bound two-body Coulomb system will be ionized. The same is exploited for the $2S-n'S$ transition $n' \rightarrow \infty$. In order to detect the two-photon transitions, they have to occur in the transient regime, because outside the transient regime all atoms are ionized by the driving laser in the limit of an infinite interaction time [14]. Thus, one of the aims in this chapter is to calculate the ionization cross sections for these two-photon transitions in the presence of the laser field.

In this Chapter, we obtain the dynamic Stark shift coefficients (*i.e.*, β_{AC} , β_{ioni}) and the two-photon transition matrix elements β_{if} for $1S-n'S$ and $2S-n'S$ transitions $n' \rightarrow \infty$ driven by the linearly polarized laser field in a Hydrogen-like atom. In Sec. 3.2, we discuss the properties of a Rydberg atom in the presence of a strong laser field and the dynamic Stark shift of the Rydberg state. In Sec. 3.2.2, we describe our calculational method based on the Sturmian representation of the radial Green's function in detail. The numerical results for $S-S$ transitions are presented in Sec. 3.2.3. In the following, we obtain the photoionization cross section using two different methods which is introduced in Sec. 3.3. In Sec. 3.4, the two-photon transition matrix elements of highly excited Rydberg states of Hydrogen-like atom (β_{if}) are calculated in such a way that the dynamic Stark shifts are calculated. We have compiled all results in SI units. Due to introducing Z -scaling in Sec. 3.4.1, these results can be appropriate for light Hydrogen-like systems. For instance, we can evaluate the dynamic Stark shift coefficients, photoionization cross sections and the generalized Rabi frequencies for a Helium ion. Thus, one can calculate AC Stark shift as a dominant systematic effect in the experimental setup, which will be applied for determination of the $1S-n'S$ transition frequency $n' \rightarrow \infty$ in Chapter 5. Section 3.5 is devoted to the partial summary and tentative concluding remarks.

3.2 Dynamic Stark shift of Rydberg states

In this section, we evaluate one of the most important systematic effects that shift the energy levels in a high-precision two-photon spectroscopy experiment *i.e.*, AC Stark shift. In this investigation, we restrict ourselves to the Rydberg state, which received considerable attentions in the contexts of high-resolution spectroscopy [33, 34].

3.2.1 General description

Rydberg atoms are those in which the valance electron is in a state of high principle quantum number. According to the Bohr model, the size of the orbits increases with the square of the principle quantum number. This fact indicates that states with a high n (Rydberg atoms) have a very large orbit and are of comparable size with a biological cell or even a manufactured object (wire, slit, \dots) [35]. Due to these unique properties, Rydberg atoms have attracted a lot of attention since two decades ago. Especially, because of their large size, these atoms are very sensitive to any external fields and can be rapidly ionized. In the case of electromagnetic radiation, one can reveal some interesting properties of Rydberg atoms, which open up the possibility of gaining further insight into the dynamics of photoionization of Rydberg atoms as well as the dynamic Stark shift of Rydberg atoms (discuss below).

In the following, we continue with discussion of the dynamic Stark shift of Hydrogen-like Rydberg atoms. Photoionization of Hydrogen-like Rydberg atoms in the presence of the strong laser field will be treated later [see Sec. 3.3]. We assume that a monochromatic laser field which is on two-photon resonance with the $1S$ – $n'S$ or $2S$ – $n'S$ transition $n' \rightarrow \infty$ interacts with the Hydrogen-like Rydberg atom, as schematically shown in Fig. 3.1. The lower state $|i\rangle$, which is $1S$ or $2S$ state and the excited state $|f\rangle$, which is $n'S$ for $n' \rightarrow \infty$ are shifted as a result of the interaction of the Hydrogen-like Rydberg atom with the strong laser field. As mentioned in Chapter 2, this displacement of the energy levels the so-called AC Stark shift is generally investigated within the framework of both a classical field method, and a fully quantized method. The calculation in the former one is based on time-dependent perturbation theory. We showed in Chapter 2 that these two methods give the same physical result at the limit of large photon numbers.

In two-photon transitions, the perturbation in a system including an atom and a laser is off-resonant [13]. Consequently, the influence of the linearly polarized laser light on the Hydrogen-like atom can be handled in the framework of the time-dependent perturbation theory *i.e.*,

$$H = H_0 + V(z, t), \quad (3.1)$$

where

$$V(z, t) = e\varepsilon_L z \cos(\omega_L t), \quad (3.2)$$

where the Hamiltonian of the bare atom H_0 is defined in Eq. (2.6). The classical electric field and the laser frequency have been denoted by ε_L and ω_L , respectively. The time-dependent perturbation $V(z, t)$ is chosen to be in the length gauge. We just recall that in

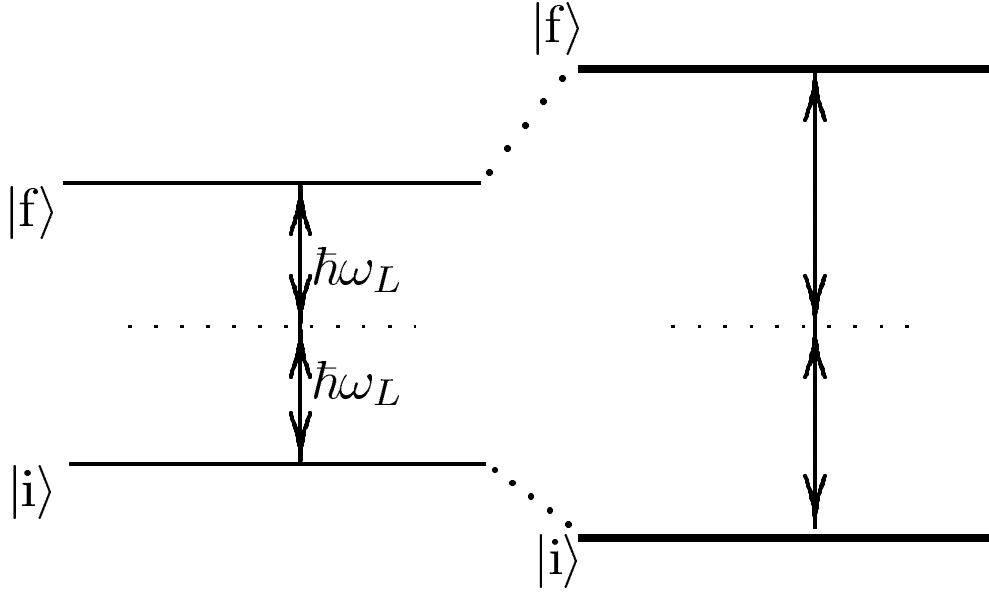


Figure 3.1: Schematic sketch of the shifting of hydrogen-like energy levels expose to a linearly polarized laser light. The location of the bare and dressed states is at the L.H.S. and R.H.S. in this figure, respectively. $|i\rangle$ represents either $1S$ or $2S$ state and $|f\rangle$ refers to $n'S$, $n' \rightarrow \infty$.

Eq. (2.5), laser + atom Hamiltonian is written in the presence of the circularly polarized laser light, while in Eq. (3.1), laser + atom Hamiltonian is considered for a linearly polarized laser light. Using the dipole approximation enables one to express the dynamic Stark shift of the reference state $|\phi\rangle$ in the first nonvanishing order of the time-dependent perturbation theory as follows [14, 13]

$$\Delta E_{AC} = \frac{-e^2}{2\varepsilon_0 c} I_L P_{\omega_L}(\phi), \quad (3.3)$$

where I_L is the intensity of the linearly polarized laser light and $P_{\omega_L}(\phi)$ is the dipole polarizability, which reads

$$P_{\omega_L}(\phi) = \sum_{\pm} \left\langle \phi \left| z \frac{1}{H_0 - E_{\phi} \pm \hbar\omega_L} z \right| \phi \right\rangle. \quad (3.4)$$

In Eq. (3.4), E_{ϕ} is the energy of the reference state $|\phi\rangle$ and reads

$$E_{\phi} = -\frac{(Z\alpha)^2 m_e c^2}{2n'^2}. \quad (3.5)$$

The frequency of the laser light in the two-photon resonant spectroscopy of the transition $i \Leftrightarrow f$ is $\omega_L = \frac{1}{2\hbar}(\omega_f - \omega_i)$.

As it is clear from Fig. 3.2, the upper state $|C\rangle$ is in the continuum region, which implies that the energy E is positive and thus the energy parameter $\eta = \frac{Z\hbar}{a_0} \sqrt{-(2m_e E)^{-1}}$

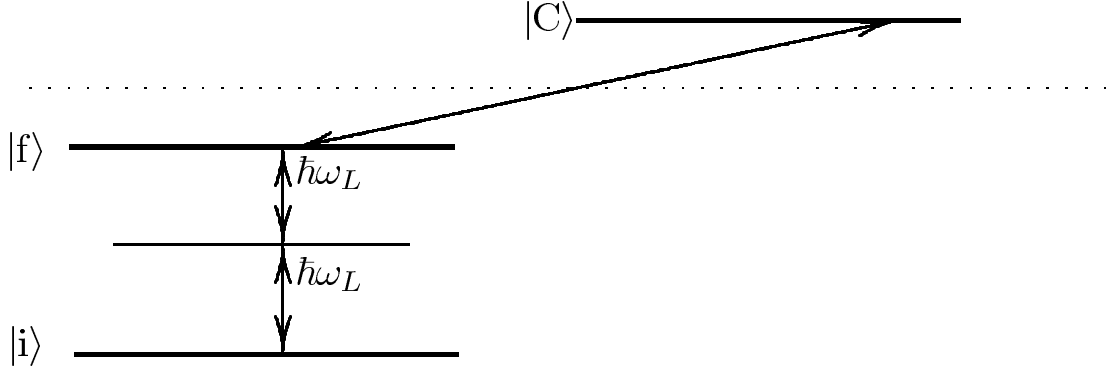


Figure 3.2: Schematic representation of the excitation including ionization channels. The dotted line represents the ionization threshold, and $|C\rangle = |\varepsilon P\rangle$ are electronic continuum states. The state $|i\rangle$ denotes either $1S$ or $2S$. $|f\rangle$ refers to the excited state, which is $n'S$ ($n' \rightarrow \infty$).

is complex. Therefore, the dynamic polarizability $P_{\omega_L}(\phi)$ is a complex quantity. Its real part refers to a shift of the atomic energy levels and its imaginary part is proportional to the ionization rate of the population in the reference state $|\phi\rangle$ (for more details see Chapter 2 and Ref. [14]):

$$\Delta\nu_{AC} = \frac{1}{\hbar} \text{Re}[\Delta E_{AC}(\phi)] = \beta_{AC}(\phi) I_L, \quad (3.6a)$$

$$\gamma_{\text{ioni}} = -\frac{2}{\hbar} \text{Im}[\Delta E_{AC}(\phi)] = 2\pi\beta_{\text{ioni}} I_L. \quad (3.6b)$$

Note that $\beta_{AC}(\phi)$ and $\beta_{\text{ioni}}(\phi)$ are intensity-independent constants and the ionization rate is given in units of angular frequency.

3.2.2 Evaluation of the AC Stark shift for Rydberg states

This section is devoted to the evaluation of the AC Stark shift for Rydberg states. Our starting point is the evaluation of the dipole polarizability Eq. (3.4). The usual approach to obtain the dipole polarizability is based on the Sturmian representation of the radial Green's function for the Hydrogen-like atom [see Ref. [36]]. In the spherical coordinate, the Green's function is given,

$$\frac{1}{H - E(\eta)} = \sum_{l'm'} g_{l'}(r_1, r_2; \eta) Y_{l'm'}(\theta_1, \varphi_1) Y_{l'm'}^*(\theta_2, \varphi_2), \quad (3.7)$$

where the radial component of the Schrödinger-Coulomb propagator reads [36]

$$g_{l'}(r_1, r_2; \eta) = \frac{2m_e}{\hbar^2} \left(\frac{2}{a_0\eta} \right)^{2l'+1} (r_1 r_2)^{l'} e^{-(r_1+r_2)/a_0\eta} \sum_{k=0}^{\infty} \frac{L_k^{2l'+1} \left(\frac{2r_1}{a_0\eta} \right) L_k^{2l'+1} \left(\frac{2r_2}{a_0\eta} \right)}{(k+1)_{2l'+1} (l'+1+k-\eta)}, \quad (3.8)$$

containing associated Laguerre polynomials $L_k^{2l'+1}$ and the Bohr radius a_0 . In Eq. (3.8), $(a)_n = \Gamma(a+n)/\Gamma(a)$ is the Pochhammer symbol. We have used the dimensionless parameter $\eta = \frac{Z\hbar}{a_0} \sqrt{-(2m_e E)^{-1}}$ [14]. The index l' is summed over possible angular momentum quantum numbers of the virtual state, *i.e.*, P states in the propagator.

After substituting Eqs. (3.7) and (3.8) in Eq. (3.4), one can divide it to radial and angular parts that are represented by the following relations, respectively.

$$M_{l'=1}^{\text{ang}} = \frac{1}{3},$$

$$M_{l'=1}^{\text{rad}} = \lim_{n' \rightarrow \infty} \int_0^{n'} r_1^3 r_2^3 R_{n'S}^*(r_1) R_{n'S}(r_2) g_1(r_1, r_2, \eta) dr_1 dr_2. \quad (3.9)$$

The radial part of the reference state $n'S$, $n' \rightarrow \infty$ can be expressed in terms of the ordinary Bessel function $J_\nu(z)$, *i.e.*, [37]

$$\lim_{n' \rightarrow \infty} R_{n'l}(r) = \frac{1}{a_0} \sqrt{\frac{2}{r}} J_{2l+1} \left(\sqrt{\frac{8r}{a_0}} \right), \quad (3.10)$$

where l is the angular momentum quantum number and the normalization condition for the wave functions with a large principal quantum number n' is

$$\int \psi_{lm}^*(\mathbf{r}) \psi_{l'm'}(\mathbf{r}) d\mathbf{r} = n'^{-3} \delta_{ll'} \delta_{mm'}. \quad (3.11)$$

Simplifying further, one obtains

$$M_{l'=1}^{\text{rad}} = \frac{32m_e}{\hbar^2 a_0^3 \eta^3} \sum_{k=0}^{\infty} \frac{\Gamma(k+1)}{\Gamma(k+4)(2+k-\eta)} \times |I|^2, \quad (3.12)$$

where I reads:

$$I = \int_0^\infty r^{7/2} J_1 \left(\sqrt{\frac{8r}{a_0}} \right) L_k^3 \left(\frac{2r}{a_0 \eta} \right) e^{-\frac{r}{a_0 \eta}} dr. \quad (3.13)$$

The major challenge in this calculation is to solve the radial integral in Eq. (3.13). There is no analytical solution to this integral. Hence, one has to solve it numerically.

To do so, this integral must be regularized and the following form of the Bessel function should be applied [38],

$$J_1(x) = \frac{-i}{2\pi} \int_0^{2\pi} \cos \theta e^{ix \cos \theta} d\theta. \quad (3.14)$$

As a result, Eq. (3.13) can be rewritten as follows,

$$I = \frac{-i}{2\pi} \int_0^{2\pi} \cos \theta \int_0^\infty r^{7/2} e^{i\sqrt{\frac{8r}{a_0}} \cos \theta} L_k^3 \left(\frac{2r}{a_0 \eta} \right) e^{-\frac{r}{a_0 \eta}} dr d\theta. \quad (3.15)$$

The following useful relation is used in the numerical calculations [see Ref. [24]].

$$\int_0^\infty dr e^{-\lambda r} r^\gamma L_n^\mu(r) = \frac{\lambda^{-1-\gamma} \Gamma(\gamma+1)}{n! \Gamma(\mu+1)} \Gamma(\mu+n+1) {}_2F_1(-n, \gamma+1, \mu+1, \lambda^{-1}), \quad (3.16)$$

where the symbol ${}_2F_1$ designates the Hypergeometric function.

Table 3.1: Dynamic Stark shift coefficients β_{AC} and ionization coefficients β_{ioni} for $1S \Leftrightarrow n'S$ and $2S \Leftrightarrow n'S$, ($n' \rightarrow \infty$) transitions (on two-photon resonance) in the nonrelativistic dipole approximation, evaluated for the nuclear charge number $Z = 1$ and an infinite nuclear mass. The results obtained in this work based on the nonrelativistic hydrogen Green's function (Sturmian function method) are in good agreement with those obtained in Ref. [16], which relies on an extrapolation technique.

$n' \rightarrow \infty$	$\beta_{AC}(1S)[\text{Hz}(\text{W}/\text{m}^2)^{-1}]$ this work	$n'^3 \cdot \beta_{\text{ioni}}(n'S)[\text{Hz}(\text{W}/\text{m}^2)^{-1}]$ this work	$\beta_{AC}(1S)[\text{Hz}(\text{W}/\text{m}^2)^{-1}]$ Ref. [16]
$1S \Leftrightarrow n'S$	-3.43809×10^{-5}	3.63479×10^{-4}	- -
$2S \Leftrightarrow n'S$	-2.43599×10^{-3}	3.47952×10^{-2}	-2.43342×10^{-3}

3.2.3 The results for S – S transitions

The nonrelativistic numerical results of the asymptotic dynamic Stark shift coefficients β_{AC} and the ionization coefficient β_{ioni} using Eqs. (3.6a) and (3.6b) are presented in Table 3.1. These results are only valid for a laser frequency on two-photon resonance with a S – S transition. It is important to note that two important approximations for obtaining these results have been considered: (i), the dipole approximation, (ii), employing only up to the second-order in perturbation theory. The negative sign for the energy shift of $|1S\rangle$ indicates that the ground state of the unperturbed atom + field Hamiltonian is always downwards, as we expect from any second-order perturbation theory [see Table 3.1].

Before ending this section, it should be mentioned that some of the results have been obtained via an extrapolation technique in the literature [see Ref. [16]]. Our results obtained by the direct calculation yield those appeared in Table Ic in Ref. [16] by using the following conversion factor,

$$\beta_{AC}(\phi)[a.u.] = \beta_{AC}(\phi)[SI] \frac{\hbar^2}{m_e a_0^4 \alpha}. \quad (3.17)$$

Note that the same relation can be used for $\beta_{\text{ioni}}(\phi)$.

3.3 Photoionization cross section of Rydberg states

This section is dedicated to the calculation of the photoionization cross section for the Hydrogen-like atom in the presence of the laser field driving the transition $1S$ – $n'S$ and $2S$ – $n'S$, $n' \rightarrow \infty$. Due to the presence of $V(z, t)$ in the Hamiltonian H [see Eqs. (3.1) and (3.2)], the Hamiltonian H has discrete energy states along with the continuous background at $E_\phi + \hbar\omega_L$. $V(z, t)$ results in the transition between the discrete and continuous part of the energy states. This fact indicates that the Hydrogen-like atom is ionized by the laser field $V(z, t)$. That is to say, the excited state $n'S$, $n' \rightarrow \infty$ of a Hydrogen-like atom driven

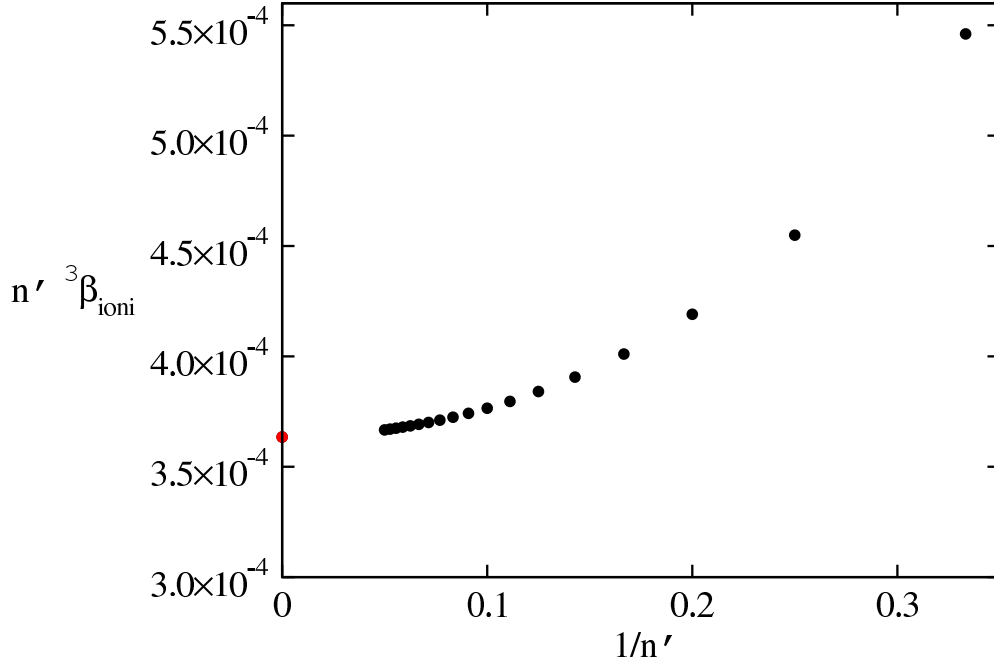


Figure 3.3: The ionization coefficients $\beta_{\text{ioni}}(1S \leftrightarrow n'S)$ for $l = 0$ are in excellent agreement with its asymptotic limit $n' \rightarrow \infty$. We plot $n'^3\beta_{\text{ioni}}$ as a function of the inverse of the principle quantum number n' . The asymptotic value is shown by red circle. The black circles refer to the numerical data for principle quantum numbers less than 20 extracted from Ref. [14].

by the laser field on two-photon resonance with the $1S$ – $n'S$ transition $n' \rightarrow \infty$ leads to the ionization of the Hydrogen-like atom if the absorption of one additional photon from the laser field happens. This ionization, as shown in Fig. 3.2, takes place through the channel $n'S \Rightarrow \varepsilon P$, $n' \rightarrow \infty$, where εP are the electronic continuum states. The same applies to the $2S$ – $n'S$ transition, $n' \rightarrow \infty$.

We therefore evaluate the corresponding ionization cross sections in two different methods. The first method is based on the proportionality of the imaginary part of the dynamic Stark shift with the ionization cross section [see Eq. (3.6b)],

$$\sigma_{\text{ioni}} = 2\pi\beta_{\text{ioni}}\hbar\omega_L. \quad (3.18)$$

Therefore, the ionization cross section reads:

$$n'^3\sigma_{\text{ioni}}^{1S \leftrightarrow n'S}[n' \rightarrow \infty] = 2.489 \times 10^{-17}/Z^2 \text{ cm}^2, \quad (3.19a)$$

$$n'^3\sigma_{\text{ioni}}^{2S \leftrightarrow n'S}[n' \rightarrow \infty] = 5.957 \times 10^{-16}/Z^2 \text{ cm}^2. \quad (3.19b)$$

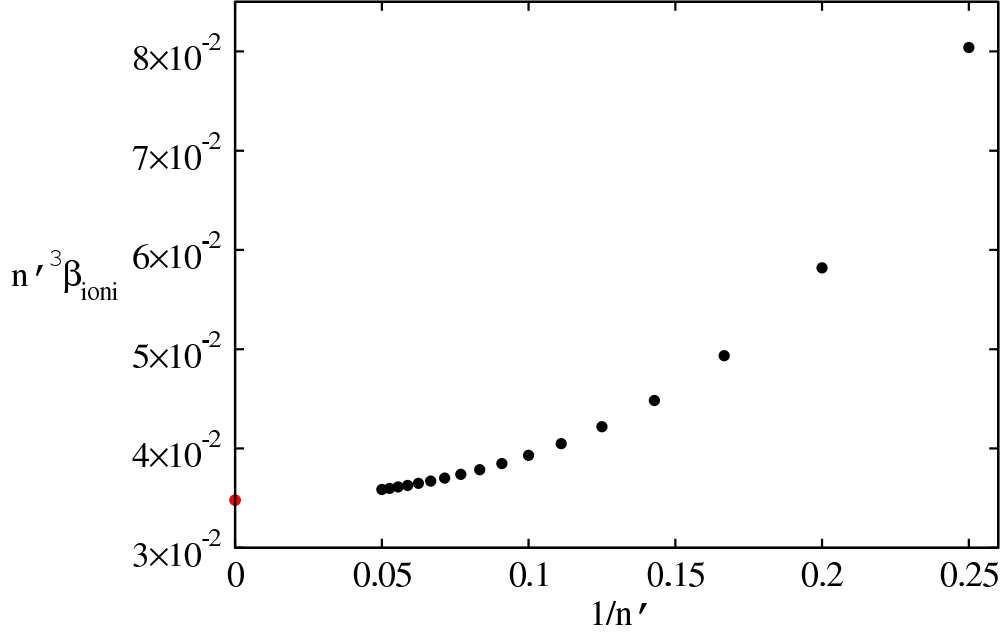


Figure 3.4: The ionization coefficients $\beta_{\text{ioni}}(2S \Leftrightarrow n'S)$ for $l = 0$ are in excellent agreement with its asymptotic limit $n' \rightarrow \infty$. We plot $n'^3 \beta_{\text{ioni}}$ as a function of the inverse of the principle quantum number n' . The asymptotic value is shown by red circle. The black circles refer to the numerical data for principle quantum numbers less than 20 extracted from Ref. [14].

The factor n'^3 is originated from the fact that the radial wave functions for large quantum number are renormalized in a way that their norms inversely proportional to their splitting in the energy (*i.e.*, $r^2 R_{n'l}^2 \propto n'^{-3}$) [see Eqs. (3.10) and (3.11)]. The results obtained from Eq. (3.19) indicate that the Z -scaling of the ionization cross section for the scheme with the nuclear charge number Z is Z^{-2} .

In the following, we introduce the second method of the cross section calculation. This calculation is based on a dipole transition from the bound state $n'S$, $n' \rightarrow \infty$ to the continuum εP state. Such an ionization cross section can be expressed in terms of the intensity of the laser field, the laser frequency and the ionization rate γ_{ioni} , *i.e.*,

$$\sigma_{\text{ioni}} = \frac{\hbar \omega_L}{I_L} \gamma_{\text{ioni}}, \quad (3.20)$$

where the ionization rate can be expressed in terms of the square of the transition matrix element and reads

$$\gamma_{\text{ioni}} = \lim_{n' \rightarrow \infty} \frac{\pi e^2 I_L}{\varepsilon_0 c \hbar} \left| \langle u_w | z | n'l \rangle \right|^2. \quad (3.21)$$

In Eq. (3.21), the radial wavefunction of discrete states is introduced in Eq. (3.10) and u_w

the radial wavefunction of the continuum state reads

$$u_w = R_w(r)Y_{l'm'}(\theta, \varphi)$$

$$R_w(r) = \frac{2\sqrt{Z}}{\sqrt{1 - e^{-2\pi n}}} \sqrt{1 + n^2} (2kr)^{-l'-1} \times \frac{1}{2\pi} \oint e^{-2ikr\xi} \left(\xi + \frac{1}{2}\right)^{-in-l'-1} \left(\xi - \frac{1}{2}\right)^{in-l'-1} d\xi, \quad (3.22)$$

where $n = i/\sqrt{2E_w}$ is the generalized principal quantum number for the continuum state.

The main task is to calculate the transition matrix element appearing in Eq. (3.21), *i.e.*,

$$M = \lim_{n' \rightarrow \infty} \langle u_w | z | n'l \rangle. \quad (3.23)$$

To do so, the matrix element should be separated into its angular and radial parts:

$$M_{l'=1}^{\text{ang}} = \frac{1}{\sqrt{3}},$$

$$M_{l'=1}^{\text{rad}} = \lim_{n' \rightarrow \infty} \int_0^\infty r^3 R_{\varepsilon P}^*(r) R_{n'S}(r) dr. \quad (3.24)$$

Now, by substituting Eq. (3.10) and Eq. (3.22) into Eq. (3.24), we obtain

$$M_{l'=1}^{\text{rad}} = \frac{\sqrt{2}\sqrt{1+n^2}}{\pi\sqrt{1-e^{-2\pi n}}} \times \int_0^\infty r^{1/2} J_1\left(\sqrt{\frac{8r}{a_0}}\right) e^{-2ikr\xi} \frac{1}{4k^2} \oint \left(\xi + \frac{1}{2}\right)^{-in-2} \left(\xi - \frac{1}{2}\right)^{in-2} d\xi. \quad (3.25)$$

The first radial integral in Eq. (3.25) could be obtained using [see Ref. [39] page 187, Eq. (27)]

$$\int_0^\infty e^{-pt} t^{\frac{1}{2}} J_1(2a^{\frac{1}{2}} t^{\frac{1}{2}}) dt = a^{\frac{1}{2}} p^{-2} e^{-\frac{a}{p}}. \quad (3.26)$$

Therefore, the first integral in Eq. (3.25) reads

$$I^{\text{rad}}(\xi) = \frac{i}{2\sqrt{2}} \frac{n^2}{\xi^2} e^{\frac{in}{\xi}}. \quad (3.27)$$

After substituting Eq. (3.27) in Eq. (3.25), $M_{l'=1}^{\text{rad}}$ reads

$$M_{l'=1}^{\text{rad}} = \frac{n^4 \sqrt{1+n^2}}{4\pi\sqrt{3}(1-e^{-2\pi n})} I_C, \quad (3.28)$$

where I_C is

$$I_C = \oint \frac{\left(\xi + \frac{1}{2}\right)^{-in-2} \left(\xi - \frac{1}{2}\right)^{in-2} e^{in/\xi}}{\xi^2}. \quad (3.29)$$

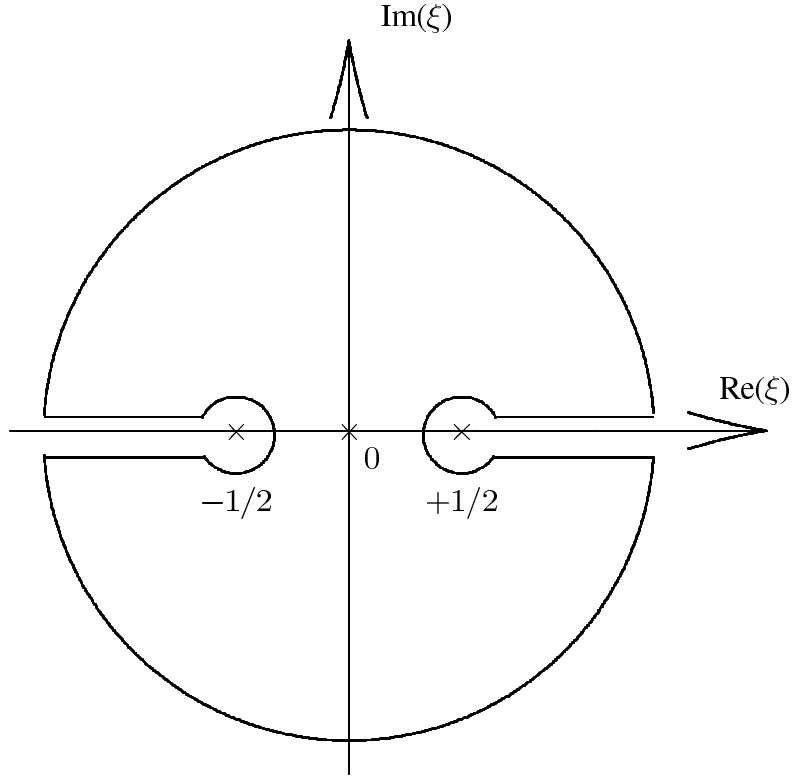


Figure 3.5: Definition of the contour of the integral form of Eq. (3.29) (Ref. [5])

In Eq. (3.29), I_C should be solved by using Cauchy's residue

$$\oint_C f(\xi) d\xi = 2\pi i \sum_{k=1}^m \text{Res}(a_k). \quad (3.30)$$

Eq. (3.29) has an isolated essential singularity at $\xi = 0$ but no other singularity at a finite. From the expansion of the exponential term in Eq. (3.29), one can evaluate this integral [40] using the contour shown in Fig. 3.5. Accordingly, the integral must be taken around the two branch point $\xi = \pm 1/2$. Therefore, I_C reads [for $1S \Leftrightarrow n'S \ n' \rightarrow \infty$]

$$I_C = \frac{-128}{407\ 698\ 691\ 540\ 765\ 625} \pi n e^{-n\pi} \chi(n). \quad (3.31)$$

$\chi(n)$ is defined as follow:

$$\begin{aligned} \chi(n) = & -407\ 698\ 691\ 540\ 765\ 625 - 271\ 799\ 127\ 693\ 843\ 750n^2 - 72\ 479\ 767\ 385\ 025\ 000n^4 \\ & - 10\ 699\ 394\ 233\ 027\ 500n^6 - 1\ 010\ 772\ 266\ 253\ 750n^8 - 66\ 538\ 149\ 678\ 000n^{10} - \\ & - 3\ 230\ 756\ 474\ 400n^{12} - 120\ 544\ 464\ 600n^{14} - 22\ 309\ 003\ 620n^{16} + 24\ 103\ 866\ 264n^{18} \\ & - 7\ 076\ 888\ 000n^{20} + 735\ 105\ 488n^{22} - 32\ 293\ 040n^{24} + 636\ 832n^{26} - \\ & - 5\ 440n^{28} + 16n^{30}. \end{aligned} \quad (3.32)$$

For the case of an incident laser with angular frequency of one half of the $1S \Leftrightarrow n'S$ transition $n' \rightarrow \infty$, the generalized quantum number of the continuum state is $n = i\sqrt{2}$, and leads to the nonrelativistic result

$$n'^3 \sigma_{\text{ioni}}^{1S \Leftrightarrow n'S} [n' \rightarrow \infty] = \frac{1}{Z^2} 2.489 \times 10^{-17} \text{ cm}^2. \quad (3.33)$$

This result is within the given accuracy identical to the result obtained in Eq. (3.19a).

3.4 Two-photon transition matrix elements

This section is dedicated to the calculation of two-photon transition matrix elements for $1S \Leftrightarrow n'S$ and $2S \Leftrightarrow n'S$ transitions $n' \rightarrow \infty$ in a Hydrogen-like atom. The interacting system of atom + laser has been described by a Hamiltonian which is presented in Sec. (3.2.1), [see Eqs. (3.1) and (3.2)]. Similar to the dynamic Stark shift, the time-dependent perturbation $V(t)$ is chosen to be in the length gauge, and the dipole approximation is considered in the calculation. Therefore, the two-photon transition matrix element β_{if} , as obtained in Ref. [14] reads

$$\beta_{if} = -\frac{e^2}{2\hbar c \epsilon_0} \left\langle f \left| z \frac{1}{H_0 - E_i - \hbar\omega_L} z \right| i \right\rangle, \quad (3.34)$$

where $|i\rangle$ refers to the initial state $|1S\rangle$ or $|2S\rangle$ and $|f\rangle$ is for $|n'S\rangle$, $n' \rightarrow \infty$.

To obtain β_{if} for transition the schematically shown in Fig. 3.2, we apply the same calculational technique as for the dynamic Stark shift [see Eqs. (3.7) and (3.8)]. The only difference is that in the case of the calculation of two-photon transition matrix elements, the intermediate states are in the bound area indicating, that the parameter η introduced in Sec. 3.2.2 is real and thus the two-photon transition matrix elements are real quantities, while η is an imaginary parameter for the AC Stark shift.

The two-photon transition matrix element is an important input parameter in the determination of the generalized Rabi frequency. Due to the two-photon nature of the excitation process in $1S \Leftrightarrow n'S$ and $2S \Leftrightarrow n'S$ transitions in Hydrogen-like atoms, it is defined by [14]

$$\Omega_{\text{Rabi}} = 4\pi\beta_{if}I_L, \quad (3.35)$$

where the intensity of the linearly polarized laser field I_L is

$$I_L = \frac{1}{2} \epsilon_0 c \epsilon_L^2. \quad (3.36)$$

3.4.1 Results for two-photon transitions

Our numerical results for the two-photon transition matrix element β_{if} for the transitions $1S \rightarrow n'S$ and $2S \rightarrow n'S$, $n' \rightarrow \infty$ within the nonrelativistic framework are shown in Table 3.2.

Table 3.2: Two-photon transition matrix elements β_{if} in units $[\text{Hz}(\text{W}/\text{m}^2)^{-1}]$ for $1S \Leftrightarrow n'S$ and $2S \Leftrightarrow n'S$ transitions $n' \rightarrow \infty$, as described in Eq. (3.34), obtained for the Hydrogen atom, in the nonrelativistic dipole approximation. The results obtained in this work (β_{if}) based on the nonrelativistic Hydrogen Green's function (Sturmian function method) are in a good agreement with those obtained in Ref. [16], which relies on an extrapolation technique.

$n' \rightarrow \infty$	$n'^{3/2} \cdot \beta_{if} [\text{Hz}(\text{W}/\text{m}^2)^{-1}]$ this work	$n'^{3/2} \cdot \beta_{if} [\text{Hz}(\text{W}/\text{m}^2)^{-1}]$ Ref. [16]
$1S \Leftrightarrow n'S$	3.00998×10^{-5}	- -
$2S \Leftrightarrow n'S$	-2.68478×10^{-3}	-2.68479×10^{-3}

Due to the proportionality of the position operator and the laser frequency ω_L with Z^{-1} and Z^2 in Eq. (3.34), respectively, β_{if} must be scaled by a factor $1/Z^4$ [14, 5], *i.e.*,

$$\beta_{if}(Z) = \frac{1}{Z^4} \beta_{if}(Z = 1). \quad (3.37)$$

Regarding this scaling factor, the numerical results can be easily generalized for a bound two-body Coulomb system with nuclear charge Z where $1 \leq Z \leq 10$ (for more details see Ref. [14]). This scaling law can be applied for the Stark coefficients β_{AC} and β_{ioni} discussed in Sec. 3.2.

3.5 Partial summary and tentative concluding remarks

In this chapter, we dealt with the two-photon transitions $1S \rightarrow n'S$ and $2S \rightarrow n'S$ $n' \rightarrow \infty$ in the bound two-body Coulomb system. These transitions are driven by the linearly polarized laser field on two-photon resonance with $1S \rightarrow n'S$ and $2S \rightarrow n'S$ transitions $n' \rightarrow \infty$. This process leads to the shift of the energy levels (due to interaction of the Hydrogen-like atom with the laser field) and an ionization of the Hydrogen-like atom (due to the absorption of one additional photon from the laser field). In the framework of time-dependent perturbation theory, a unified treatment, *i.e.*, the Sturmian representation of the radial Green's function, was employed for the calculation of both the dynamic Stark shift and the two-photon transition matrix elements for the Rydberg state [see Secs. 3.2.2 and 3.4]. The radial integral which appeared in the matrix elements was numerically solved, where we profited from the integral representation of the Bessel function. The corresponding results were shown in Tables 3.1, 3.2, Fig. 3.3 and Fig. 3.4. We found an agreement between our results and those obtained by others.

In Sec. 3.3, the photoionization cross sections were obtained by two different methods. The first method relied on the Sturmian representation of the radial Green's function. This

calculation was done in the framework of time-dependent perturbation theory. Considering the fact that the imaginary part of the dynamic Stark shift is proportional to the ionization cross section yielded the value of ionization cross section in S.I. units. The second one was based on the one-photon ionization cross section of the $n'S \ n' \rightarrow \infty$ state. The consistency of the results obtained from these two methods was verified in Table. 3.1 and Sec. 3.3. The Z -scaling of the dynamic Stark shift coefficients (β_{ioni} and β_{AC}), the two-photon transition matrix element β_{if} and the ionization cross section was introduced [see Eq. (3.37)], which enables to generalize easily our results to any Hydrogen-like atoms with $Z \leq 10$. This is especially useful when we need the major systematic shift, *i.e.*, AC Stark shift, in the excitation arrangement related to the determination of the $1S$ – $n'S$ transition frequency $n' \rightarrow \infty$ via Doppler-free, two-photon laser spectroscopy in the Helium ion [see Chapter 5].

Chapter 4

Dynamics of a charged particle in a Penning trap (the Geonium atom)

4.1 Introduction

The main objective of this thesis is to introduce new mechanisms in order to determine the bound-electron g factor in a Penning trap [see Chapter 5]. Therefore, it is worthwhile to study the dynamics of a charged particle in a Penning trap in detail. This is the main goal of the present chapter. However, before dealing with this subject, we would like to briefly explain various kinds of electromagnetic traps.

Electromagnetic traps are generally divided into two groups. In the first group, neutral particles or atoms are trapped. The force applied for the trapping mechanism comes from a magnetic dipole in a non-uniform magnetic field. Two well-established examples of this kind of trap are Ioffe-Pritchard and TOP traps [41, 42]. In the second group, charged particles (ions) are trapped and that is why they are called ion traps [43]. The famous ion traps are rf (Paul), Penning, combined and Kingdon traps as well as the electron beam ion trap (EBIT). We briefly explain various types of ion traps. In the rf (Paul) trap, the AC voltage between the ring electrode and two endcap electrodes along with the magnetic field \mathbf{B} traps a charged particle. Due to applying the AC voltage with the angular frequency Ω , the charged particle starts to oscillate with the same angular frequency about its mean position. Moreover, since the charged particle is affected by the inhomogeneous magnetic field, there is no balance between an inward force during one half of the oscillation period and an outward force during the other half of the oscillation period. This can be observed as a micromotion for the charged particle in the trap [44]. The combined trap is a combination of the Penning trap (explained below) and (rf) Paul trap. In this trap, two AC and DC voltages between endcaps and electrodes along with the magnetic field \mathbf{B} confine the charged particle in the trap. The major advantage of the combined trap is that two charged particles can be simultaneously stored in the trap. Therefore, this kind of trap is normally suitable to capture anti-Hydrogen, because the antiproton and the positron can be trapped at the same time. The linear and ring traps are a new generation

of the traps. Similar to the Paul trap, an AC voltage and a magnetic field \mathbf{B} are used. The most outstanding advantage of this trap is that more than one ion can be stored along the axis of the trap with no micromotion. With the aid of this technology, one can cool a large number of ions to low temperatures by a laser cooling technique, which is a base for the development of quantum computers [45]. The Kingdon trap is made of a cylinder in which a central thin wire attracts ions. This trap was used by Prior and others for spectroscopic investigations of $^3\text{He}^+$ [46]. The EBIT, developed at Lawrence Livermore National Laboratory, is used to study X-rays induced by highly charged ions that interact with electrons. In this trap, due to the presence of space-charge field coming from an intense electron beam as well as an axial magnetic field, charged particles are trapped. This type of trap has been generally utilized in the dielectronic recombination and the electron impact excitation of ions [44].

Another ion trap is the Penning trap, which is of interest to us, because of its application in studying in the behavior of charged particles. Historically, the Penning trap was characterized for the first time by F. M. Penning in 1936 [47]. The aim of his study was to deal with the properties of electrical discharges between coaxial cylinders in the presence of a magnetic field. The main result of Penning was that an electron path between two electrodes could be long in the presence of a magnetic field. After observing such a behavior from the charged particles, experimentalists were motivated to take advantage of a stored particle in the Penning trap to deal with the fundamental problems in Physics, such as testing the validity of QED and CPT invariance. In Table 4.1, we present the important developments concerning a charged particle in a Penning trap.

The ideal Penning trap is made up as follows: slow electrons with mass m and electric charge e are captured in the trap by colliding a high energetic electron beam with a small number of gaseous atoms. In addition, two combined magnetic and quadrupole electrostatic fields are simultaneously imposed on the charged particle [see Fig. 4.1]. The quadrupole electrostatic potential responsible for an axially bounding of a charged particle in the trap in a cylindrical coordinate system is [48]

$$\phi(\rho, z) = V_0 \frac{z^2 - \rho^2/2}{2d^2}, \quad (4.1)$$

where ρ and z are the radial and z components. V_0 and d are the trap potential and size, respectively. Simultaneous with the electrostatic potential, a magnetic field \mathbf{B} is imposed along the axis of the trap as shown in Fig. 4.1 to radially bound a charged particle in the trap. We have schematically shown the configuration of the electric and magnetic fields of the Penning trap in Fig. 4.1.

As mentioned, these two combined external fields store a single charged particle in the trap. This bound system can be compared with a Hydrogen atom but with an important difference. In a Hydrogen atom, a single electron bounds to the nucleus via the Coulomb potential, while in this new bound system, a single charged particle bounds to the Penning trap via the external fields. The latter one is the so-called “the Geonium atom” [48].

The Penning trap is designated to store a charged particle in a specific place. The goal of this process is twofold. The first one is to use this technique in the field of precision

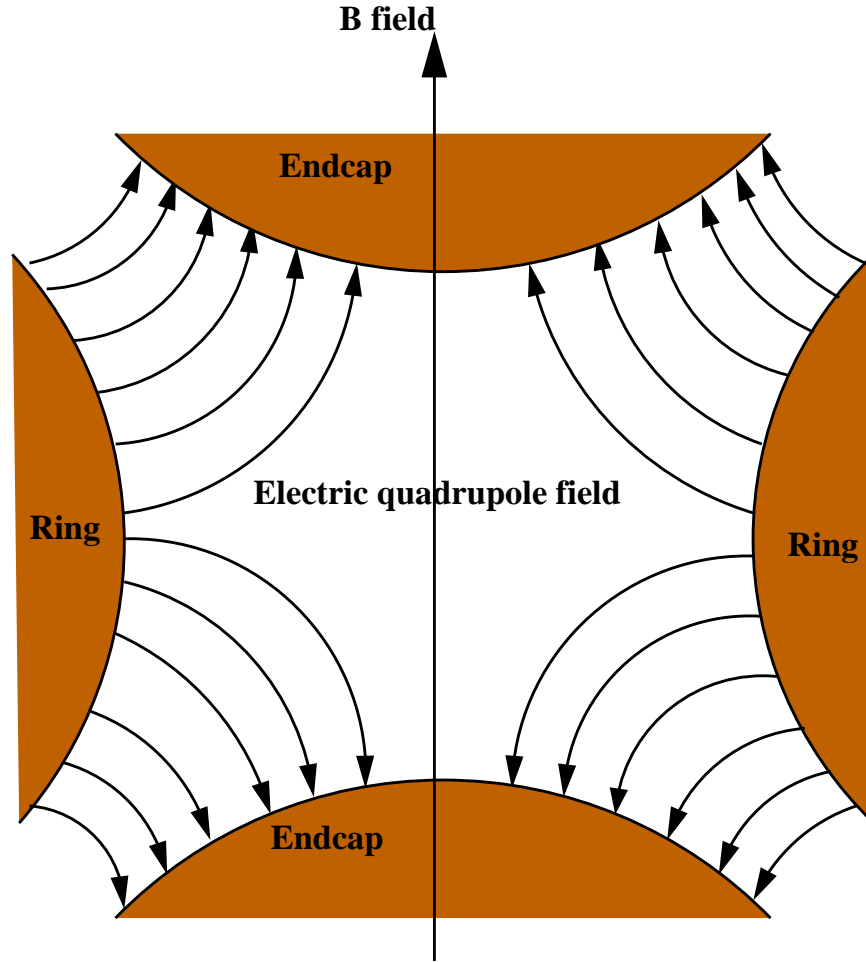


Figure 4.1: The schematic representation of the configuration of the magnetic and quadrupole electrostatic field lines.

measurements to determine the fundamental constants, such as the fine-structure constant and bound-electron g factor. The second goal is to examine concepts such as CPT with leptons and baryons, quantum electrodynamics and to perform accurate mass spectroscopy measurements.

The major advantage of a Penning trap is that a charged particle can be kept in the trap as long as desired [49]. This unique opportunity makes it possible to measure the physical constants with a high accuracy. However, this unique advantage creates some limitations in the experimental process. In other words, when the storing time is considerably long, the density of the stored particles becomes small. In order to detect these small number of particles in the trap, we need a very sensitive technique. If one increases the detection sensitivity, this precludes carrying out other types of spectroscopic experiments.

In this chapter, we systematically study the dynamics of a charged particle in a Penning trap. In Sec. 4.2, the motion of the charged particle in an ideal Penning trap in the

38 4. Dynamics of a charged particle in a Penning trap (the Geonium atom)

Table 4.1: The historical summary of important progresses for a charged particle in the Penning trap.

Year	Element	Progress	Reference
1936	e^-	Trapping of electrons in the presence of a magnetic field	Ref. [47]
1967	e^-	Measurement of the cyclotron frequency	Ref. [50]
1968	e^-	Measurement of the cyclotron frequency and the spin resonance	Ref. [51]
1968	e^-	Bolometric method	Ref. [52]
1972	He^+	Measurement of the lifetime of $2S$ state	Ref. [53]
1976	e^-	g measurement on one single electron	Ref. [54]
1978	Mg^+	Laser cooling	Ref. [55]
1981	Mg^+	Spectroscopy of a single Mg^+ ion	Ref. [56]
1985	Be^+	Frequency standard	Ref. [57]
1987	Be^+	Shell structure in a Penning trap	Ref. [58]
1988	Mg^+	Quantum jump spectroscopy	Ref. [59]
2000	C^{5+}	Observation of the continuous Stern-Gerlach effect on a bound electron	Ref. [60]
2002	C^{5+}	New determination of the electron's mass	Ref. [61]
2004	O^{7+}	Measurement of the g factor	Ref. [62]
2008	e^-	New measurement of the electron magnetic moment	Ref. [63]

framework of classical electrodynamics is investigated using the Euler-Lagrange formulation. More specifically, we consider two important cases. In the first case, the motion of charged particle in the Penning trap is investigated. In the second case, the motion of the charged particle in a Penning trap in the presence of an additional electric field is studied. The latter one is an important issue when we deal with the quenching mechanism that plays an essential role in three-photon, double resonance excitation arrangement for determining the bound-electron g factor [see Chapter 5]. In Sec. 4.3, the quantum mechanical motion of a charged particle in an ideal Penning trap is studied. We consider a real Penning trap that is suffered imperfections and derive the invariance theorem. This theorem has an application in obtaining the cyclotron frequency of an ion and bound-electron g factor [see Chapter 5]. In Sec. 4.5, we introduce two methods for obtaining the true cyclotron frequency based upon the invariance theorem and one side band frequency. Sec. 4.6 is reserved for the partial summary and tentative concluding remarks.

4.2 Classical electrodynamics of the Geonium atom

In this section, we wish to describe the classical trajectory of a charged particle in the Penning trap in two different cases:

- a charged particle trajectory in the presence of the quadrupole electric and magnetic fields (the Geonium atom),
- a charged particle trajectory in the presence of the quadrupole electric and magnetic fields in addition to an additional electric field \mathbf{E} (the Geonium atom + an additional electric field).

Let us start with the first case. The starting point is to use the Euler-Lagrange formalism to derive the equations of the classical motion.

The Lagrangian can be written in terms of the kinetic energy T and the potential energy V . The potential energy is

$$V(x, \dot{x}) = q\phi(x, y) - q\mathbf{v} \cdot \mathbf{A}(x); \quad \mathbf{A}(x, y, z) = \frac{1}{2}B(-y\mathbf{e}_x + x\mathbf{e}_y), \quad (4.2)$$

where $\phi(x, y)$ is defined in Eq. (4.1). \mathbf{v} and q are the velocity and charge of a particle in the trap, respectively.

Hence, the Lagrangian has the following form:

$$L = \frac{1}{2}m(\dot{x}^2 + \dot{y}^2 + \dot{z}^2) - \frac{qV_0}{4d^2}(2z^2 - x^2 - y^2) - \frac{qB}{2}(\dot{x}y - \dot{y}x), \quad (4.3)$$

or

$$L = \frac{1}{2}m(\dot{x}^2 + \dot{y}^2 + \dot{z}^2) - \frac{1}{4}m\omega_z^2(2z^2 - x^2 - y^2) - \frac{1}{2}m\omega_c(\dot{x}y - \dot{y}x), \quad (4.4)$$

where $\omega_c = qB/m$ and $\omega_z^2 = qV_0/md^2$. Therefore, the equations of the classical motion in x and y directions are:

$$\begin{aligned} \ddot{x} - \omega_c\dot{y} - \frac{1}{2}\omega_z^2x &= 0 \\ \ddot{y} + \omega_c\dot{x} - \frac{1}{2}\omega_z^2y &= 0, \end{aligned} \quad (4.5)$$

and for the z direction,

$$\ddot{z} + \omega_z^2z = 0. \quad (4.6)$$

Eq. (4.5) describes the radial motion with the cyclotron frequency ω_c and the magnetron frequency ω_m in the xy -plane and Eq. (4.6) represents a simple harmonic motion with the axial frequency ω_z . Eqs. (4.5) and (4.6) also indicate that the axial motion of the particle is decoupled from the radial motion.

There are various methods to obtain the analytic solution for Eq. (4.5). Here, we use the complex variable method [$u(t) = x(t) + iy(t)$], which enables us to convert the two differential equations in Eq. (4.5) into the following differential equation

$$\ddot{u}(t) + i\omega_c\dot{u}(t) - \frac{1}{2}\omega_z^2u(t) = 0. \quad (4.7)$$

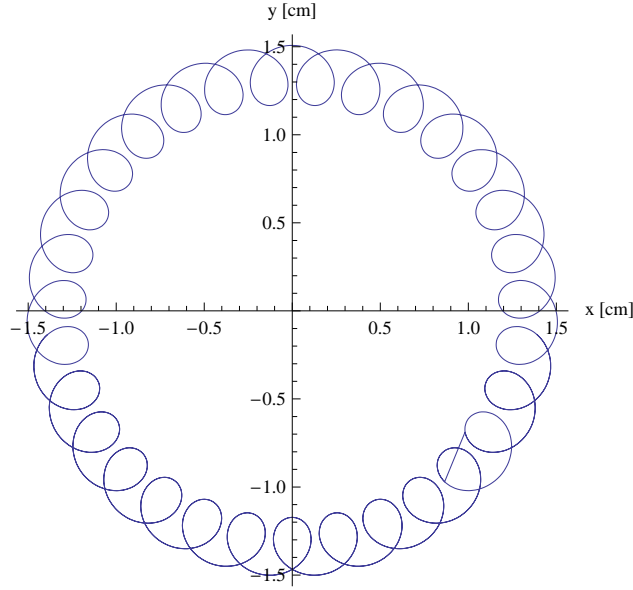


Figure 4.2: The motion of the Geonium atom in the xy -plane is composed of the cyclotron and the magnetron motions is shown [see Eq. (4.10)]. The small circles represent the cyclotron motion and the big circle shows the metastable magnetron motion in the Penning trap. Here, we have assumed that $\omega_+ = 4\omega_z$, $\omega_z = 8\omega_-$ and $A = 8B = 4z_0$.

The general answer of this simple equation is $e^{-i\omega t}$. By putting $e^{-i\omega t}$ in Eq. (4.7), one can find the modified cyclotron ω_+ and magnetron frequencies ω_- , *i.e.*,

$$\omega_{\pm} = \frac{1}{2} \left(\omega_c \pm \sqrt{\omega_c^2 - 2\omega_z^2} \right), \quad \omega_m \ll \omega_z \ll \omega_c. \quad (4.8)$$

Hence, the general solution of Eq. (4.7) is

$$u(t) = A_+ e^{-i\omega_+ t} + A_- e^{-i\omega_- t}. \quad (4.9)$$

The complex function $u(t)$ characterizes a superposition of two circular motions in the xy -plane. Eq. (4.9) indicates that this circular motion represented in Fig. 4.2 is composed of the circular magnetron motion with the magnetron frequency ($\omega_- = \omega_m$) and the modified cyclotron motion ($\omega_+ \simeq \omega_c$) [see Eq. (4.8)]. In Eq. (4.9), the second term refers to the magnetron motion, which is in an unstable equilibrium in the Penning trap. This indicates that during collisions with gaseous atoms, ions may diffuse out of the Penning trap, which can be considered as a disadvantage of the Penning trap in comparison with a rf trap, for which all three motions (axial, cyclotron and magnetron motions) are in a stable equilibrium [49].

The general solutions of Eqs. (4.5) and (4.6) in a three-dimensional Cartesian space read,

$$\begin{aligned} x(t) &= A \sin(\omega_+ t) + B \sin(\omega_- t) \\ y(t) &= A \cos(\omega_+ t) + B \cos(\omega_- t), \end{aligned} \quad (4.10)$$

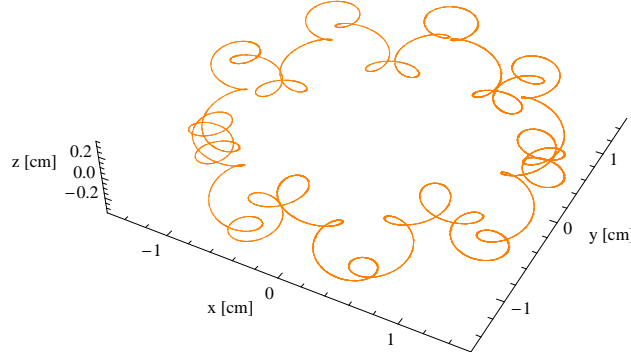


Figure 4.3: Three dimensional motion of the Geonium atom is based on the Eqs. (4.10 and 4.11), which is combined the magnetron, cyclotron, trapping motions. The initial values for this typical motion are $A = 8B = 4z_0$ and $\omega_+ = 4\omega_z$, $\omega_z = 8\omega_-$.

and

$$z(t) = z_0 \cos(\omega_z t). \quad (4.11)$$

In Fig. 4.3, we depict the ion motion for $\omega_+ = 4\omega_z$, $\omega_z = 8\omega_-$ and $A = 4z_0 = 8B$, where z_0 is the amplitude of the trapping motion.

Eqs. (4.10) and (4.11) indicate that a charged particle has a periodic motion in the trap. The length of this duration is called an overall period that is equal to the periods of the magnetron motion of the charged particle in the trap ($1/\omega_-$). In a real Penning trap, the periodic motion can happen provided that the relevant frequencies are integer or simple ratios of each other; otherwise the charged particle does not experience the periodic motion.

To better understand the foregoing physical discussion, we introduce the ratio ω_z/ω_- , the so-called trapping tune. In fact, this ratio shows the number of trapping oscillations. The frequency ratio is proportional to the overall period. This means that for a small frequency ratio, we expect a small overall period. Under this condition, the charged particles will be considerably affected during the experiments. In Fig. 4.4, we draw some examples of charged particle orbits for small ratios of its eigenfrequencies that are depicted for $\omega_+ = \omega_z = n\omega_-$, where $n = 5, 4, 3$ and 2 . These figures reveal that the charged particle performs n ($n = 5, 4, 3$ and 2) oscillations in the axial direction during one period of the magnetron motion. Moreover, an increase in the number of trapping oscillations results in an increase in the radius of the cyclotron motion. This can be described by the following relation,

$$r_c = \frac{\omega_z}{\omega_-} \frac{V_c \omega_z}{2}, \quad (4.12)$$

where V_c is the cyclotron speed of a charged particle. Eq. (4.12) indicates that for the higher numbers of trapping oscillations, the contribution of the cyclotron motion of a

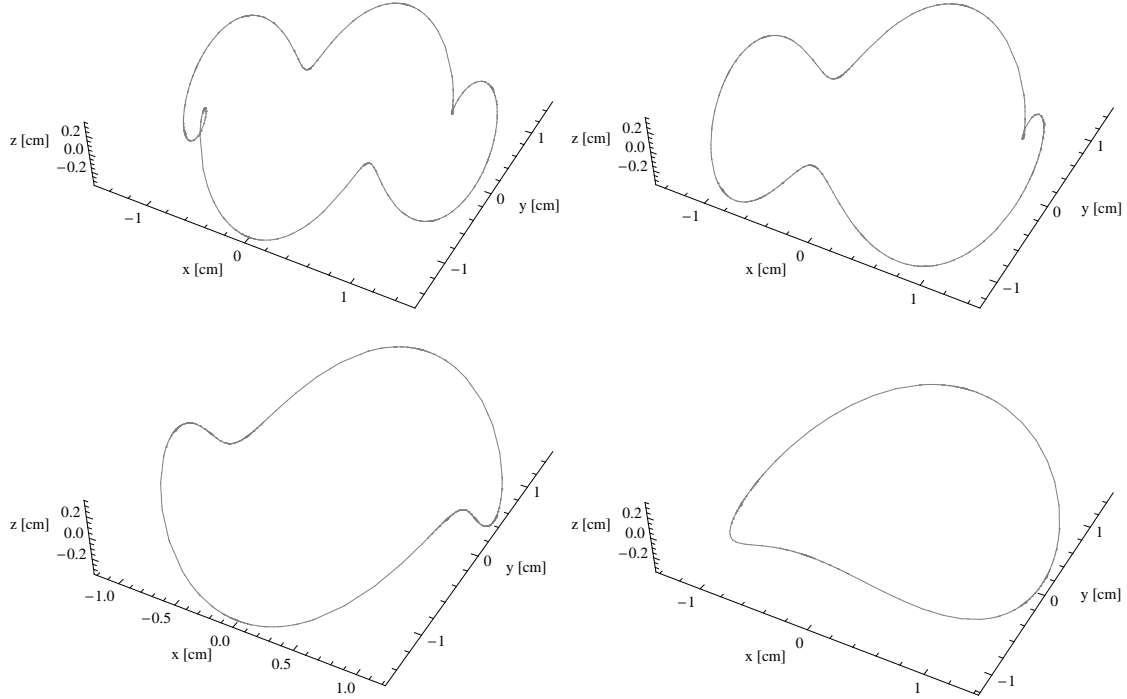


Figure 4.4: Typical examples of ion orbits for different values of the ratio ω_z/ω_- are based on Eqs. (4.10 and 4.11), which represent the number of axial oscillations. Here, the hierarchy introduced in Eq. (4.8) is changed to $\omega_- < \omega_z < \omega_+$. For the four graphs, the values of the trapping oscillations ω_z/ω_- are 5, 4, 2 and 3 (clockwise starting on the top left).

charged particle is more noticeable. In the following, we continue with the second case, *i.e.* considering the effect of an additional electric field on the Geonium atom. The reason for studying this case is that an additional electric field is responsible for a quenching mechanism in the three-photon, double resonance excitation arrangement related to the bound-electron g -factor determination [see Sec. 5.4]. In this case, the modified potential reads

$$\varphi(x, y, z) = \frac{V_0}{4d^2} (2z^2 - x^2 - y^2) - E_0 z, \quad (4.13)$$

where the second term in Eq. (4.13) refers to the contribution of the additional electric field. We again use the Euler-Lagrange method, like in the previous case. According to Eq. (4.13), the Lagrangian reads

$$L = \frac{1}{2}m(\dot{x}^2 + \dot{y}^2 + \dot{z}^2) - \frac{1}{4}m\omega_z^2(2z^2 - x^2 - y^2) - \frac{1}{2}m\omega_c(\dot{x}y - \dot{y}x) + m\omega_a^2 z, \quad (4.14)$$

where $\omega_c = qB/m$ and $\omega_z^2 = qV_0/md^2$. ω_a is defined as

$$\omega_a^2 = \frac{qE_0}{m}, \quad (4.15)$$

where E_0 is the intensity of the additional electric field. Eq. (4.14) indicates that the equations of the motion in xy -plane are the same as Eq. (4.5). This means that the additional electric field does not have any effects on the circular motion of a charged particle in the trap (*i.e.*, the magnetron and cyclotron motion). From Eq. (4.14), one can obtain the following equation for the axial motion of the particle

$$\ddot{z}(t) + \omega_z^2 z(t) = \omega_a^2. \quad (4.16)$$

The solution of Eq. (4.16) is

$$z(t) = \frac{\omega_a^2}{\omega_z^2} + z_0 \cos \omega_z t. \quad (4.17)$$

In Fig. 4.5, we draw the trajectory of the charged particle in the Penning trap in the presence and the absence of the additional electric field. In Eq. (4.17), since the ratio $\frac{\omega_a}{\omega_-}$ is proportional to the additional electric field \mathbf{E}_0 [see Eq. (4.15)], the trajectory of the charged particle depends on the value of the \mathbf{E}_0 field. According to Fig. 4.5, there is a considerable shift between these two trajectories for a large and moderate electric field, while there is a tiny shift for a small electric field.

From the experimental point of view, the value of the additional electric field has to be small in order to keep a charged particle in the trap. Hence, it is safe to say that this additional electric field produces a small shift in the charged particle orbit when its contribution is taken into account.

In the following, to carefully examine the effect of an additional electric field on the charged particle trajectory, we evaluate the average value of the square of the quadrupole electrostatic field over the trajectory of the charged particle in the trap. This calculation is performed in the presence of an additional electric field \mathbf{E}_0 . We remind that the additional electric field is responsible for the quenching mechanism in the three-photon, double-resonance excitation setup applied for the g -factor determination in Sec. 5.4. Regarding the quadrupole potential created by the two endcap electrodes and the additional electric field in Fig. 4.1, one can write the total electric field in the Cartesian coordinate system, *i.e.*

$$\begin{aligned} E_x(t) &= \frac{V_0}{2d^2} x(t), \\ E_y(t) &= \frac{V_0}{2d^2} y(t), \\ E_z(t) &= -\frac{V_0}{d^2} z(t) - E_0, \end{aligned} \quad (4.18)$$

where $x(t)$, $y(t)$ and $z(t)$ are introduced in Eqs. (4.10) and (4.17). $V_0 = 10.22$ V/cm and $d = 0.335$ cm are the trap potential and size, which are determined experimentally [see Table I from Ref. [48]]. Therefore, the average values of the square of the quadrupole electrostatic field components over one period of the motion of the charged particle in the

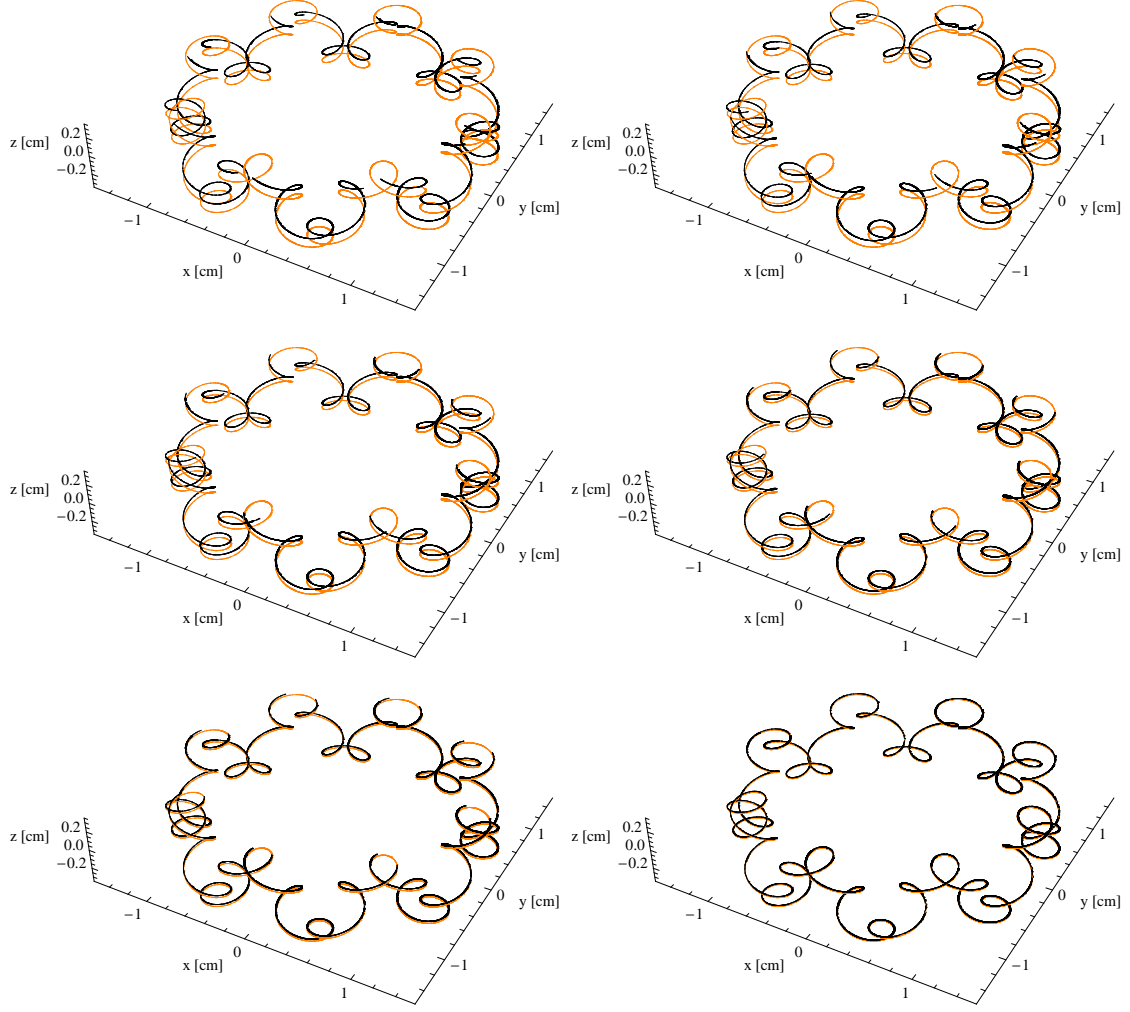


Figure 4.5: Typical examples of ion orbits (the Geonium atom) for different values of the ratio ω_a/ω_- , which is proportional to the value of additional electric field are based on Eqs. (4.10 and 4.17)]. The red line refers to the ion orbit in the absence of additional electric field and black line is the ion orbit in the presence of additional electric field. Here, the hierarchy introduced in Eq. (4.8) is considered. For the six graphs, the values of the ratio ω_a/ω_- are 2.46 (top left), 2.14 (top right), 1.82 (middle left), 1.50 (middle right), 1.18 (low left) and 0.86 (low right), respectively. The initial values for the typical motion are $A = 8B = 4z_0$ and $\omega_+ = 4\omega_z$, $\omega_z = 8\omega_-$.

trap read,

$$\begin{aligned} \langle E_x^2 \rangle &= \langle E_y^2 \rangle = \frac{V_0^2}{8d^2} [A^2 + B^2] = \frac{65V_0^2}{32d^2} \left(\frac{\text{V}}{\text{cm}} \right)^2, \\ \langle E_z^2 \rangle &= E_0^2 + \frac{V_0^2}{2d^2} \left(\frac{\text{V}}{\text{cm}} \right)^2. \end{aligned} \quad (4.19)$$

It is clear that these average values depend on the initial conditions of the charged particle motion in the trap (*i.e.*, the trap parameters V_0 and d) and the value of the additional electric field. They are evaluated for the same physical conditions applied to the trajectories in Fig. 4.5

$$\begin{aligned}\langle E_x^2 \rangle &= \langle E_y^2 \rangle = 1890.5 \left(\frac{\text{V}}{\text{cm}} \right)^2, \\ \langle E_z^2 \rangle &= E_0^2 + 465.353 \left(\frac{\text{V}}{\text{cm}} \right)^2.\end{aligned}\tag{4.20}$$

To keep a charged particle in the trap, the value of the additional electric field must remain small. Therefore, the average value of the z component of the total electric field depends weakly on the value of the additional electric field \mathbf{E}_0 . This shows that the effect of an additional electric field \mathbf{E}_0 on the average value of the square of the quadrupole electrostatic field over the trajectory of the charged particle in the trap is negligible. This effect is also observed in Fig. 4.5, where the two trajectories for small values of the additional electric field are compared and nearly coincided with the charged particle trajectory in the absence of the additional electric field (black and red colors). Therefore, the conclusion we can draw is that the small additional electric field does not have any considerable effects on the trajectory of a charged particle in the Penning trap.

4.3 Quantum motion of the Geonium atom

In this section, we deal with the quantum mechanical motion of the charged particles in a perfect Penning trap (the Geonium atom). In this study, we introduce two methods of calculation. The first one is based on an analytical solution of the Schrödinger equation as described in Ref. [64], while the second one is based on raising and lowering operators.

In the first method, we consider the following Hamiltonian for the charged particle in the trap,

$$H = \frac{\mathbf{p}^2}{2m} + \phi(\rho, z),\tag{4.21}$$

where $\mathbf{p} = i\hbar\nabla + (e/c)\mathbf{A}(x, y)$. $\phi(\rho, z)$ and $\mathbf{A}(x, y)$ are defined in Eq. (4.1) and Eq. (4.2), respectively. e and m are the charge and the mass of a charged particle. Therefore, the Schrödinger equation of a charged particle in the presence of the quadratic electrostatic potential introduced in Eq. (4.1) can be expressed as,

$$i\hbar \frac{\partial \psi}{\partial t} = H\psi,\tag{4.22}$$

According to findings of Ref. [64], the solution of Eq. (4.22) is,

$$\psi(\rho, \varphi, z) = \frac{1}{\sqrt{2\pi}} e^{-iEt/\hbar + il\varphi} R(\rho) u(z),\tag{4.23}$$

46 4. Dynamics of a charged particle in a Penning trap (the Geonium atom)

where l is the orbital quantum number [see Eq. (4.29)]. The radial $R(\rho)$ and axial $u(z)$ parts of the wavefunction introduced in Eq. (4.23) can be obtained from the following coupled relations [64],

$$\begin{aligned} u''(z) + \left(\frac{2m}{\hbar^2} E_2 - \gamma_2^2 z^2 \right) u(z) &= 0, \\ R''(\rho) + \frac{1}{\rho} R'(\rho) + \left(\frac{2mE_1}{\hbar^2} - 2\gamma l - \frac{l^2}{\rho^2} - \gamma_1^2 \rho^2 \right) R(\rho) &= 0. \end{aligned} \quad (4.24)$$

In Eq. (4.24), the primes illustrate that the radial and axial parts of the wave function are differentiated with respect to ρ and z , respectively. In Eq. (4.24), E_1 and E_2 satisfy the following constraint,

$$E_1 + E_2 = \hbar \left[\omega_H \left(N + \frac{1}{2} \right) - \omega_E \left(s + \frac{1}{2} \right) + \omega_s \left(k + \frac{1}{2} \right) \right], \quad (4.25)$$

where $\omega_H = \frac{1}{2}(\Omega + \Omega_1)$, $\omega_E = \frac{1}{2}(\Omega - \Omega_1)$ and $\omega_s = \sqrt{\frac{2e^2 d}{m}}$. Here, Ω and Ω_1 read,

$$\Omega = \frac{eB}{mc}, \quad \Omega_1 = \Omega \sqrt{1 - \frac{4amc^2}{B^2}}, \quad (4.26)$$

where $0 < a < B^2/4mc^2$ and \mathbf{B} is the magnetic field. The general solution of the Eq. (4.22) is,

$$\psi_{Nsk}(\rho, \varphi, z) = \frac{1}{\sqrt{2\pi}} e^{il\varphi} \sqrt{2\gamma_1} I_{N,s}(\gamma_1 \rho^2) \left(\frac{\gamma_2}{\pi} \right)^{1/4} \sqrt{\frac{1}{2^k k!}} e^{-\gamma_2 z^2/2} H_k(\sqrt{\gamma_2} z), \quad (4.27)$$

with

$$I_{N,s}(\rho) = \frac{1}{\sqrt{(s+l)!s!}} e^{-\frac{1}{2}\gamma_1 \rho^2} (\gamma_1 \rho)^{l/2} L_s^l(\gamma_1 \rho^2), \quad (4.28)$$

where $\gamma_1 = \gamma \sqrt{1 - \frac{4dmc^2}{B^2}}$, $\gamma_2 = 2dme^2/\hbar^2$ and $\gamma = eB/2c\hbar$. In Eqs. (4.27) and (4.28), H_k and L_s^l are designated for the Hermite polynomial and the Laguerre polynomial, respectively. Here, m is the mass of the charged particle, c is the velocity of light and d is the size of the trap. Note that k , l and s are the axial, orbital and radial quantum numbers, respectively. The principal quantum number n is the sum of the two quantum number l and s . The range of these quantum numbers is as follows:

$$\begin{aligned} k &= 0, 1, 2, 3, \dots, \\ l &= 0, \pm 1, \pm 2, \pm 3, \dots, \\ s &= \begin{cases} 0, 1, 2, 3, \dots & \text{if } l \geq 0, \\ -l, -l+1, \dots & \text{if } l < 0 \end{cases} \\ n = l + s &= \begin{cases} l, l+1, l+2, l+3, \dots & \text{if } l \geq 0, \\ 0, 1, 2, \dots & \text{if } l < 0. \end{cases} \end{aligned} \quad (4.29)$$

We can also write the general wave function of Eq. (4.27) in the separated form when we want to separately study the quantum radial and axial motions [64], *i.e.*,

$$\begin{aligned} u_k(z) &= \left(\frac{\gamma_2}{\pi}\right)^{1/4} \sqrt{\frac{1}{2^k k!}} e^{-\gamma_2 z^2/2} H_k(\sqrt{\gamma_2} z), \\ R_{l,s}(\rho) &= \frac{\sqrt{2\gamma_1}}{\sqrt{s!(s+l)!}} e^{-\gamma_1 \rho^2/2} (\gamma_1 \rho^2)^{l/2} L_s^l(\gamma_1 \rho^2). \end{aligned} \quad (4.30)$$

Note that the first relation in Eq. (4.30) refers to the quantum mechanical axial motion and the second one denotes the combined cyclotron and magnetron motions.

The second method for the quantum mechanical investigation of the charged particle in the trap (the Geonium atom) relies upon the raising and lowering operators as described in Ref. [48]. The main advantage of this method is that it enables us to investigate separately the axial, cyclotron and magnetron motions of the charged particle in the trap. With the combination of these three motions, we can easily describe the quantum behavior of the charged particle in the Penning trap.

Let us first consider the axial motion. The Hamiltonian of the axial motion, which is similar to that of the one-dimensional harmonic oscillator reads,

$$H_z = \frac{p_z^2}{2m} + \frac{1}{2} m \omega_z^2 z^2. \quad (4.31)$$

We define the non-Hermitian raising and lowering operators as follows,

$$\begin{aligned} a_z &= \left(\frac{m\omega_z}{2\hbar}\right)^{1/2} z + i\left(\frac{1}{2m\hbar\omega_z}\right)^{1/2} P_z, \\ a_z^\dagger &= \left(\frac{m\omega_z}{2\hbar}\right)^{1/2} z - i\left(\frac{1}{2m\hbar\omega_z}\right)^{1/2} P_z. \end{aligned} \quad (4.32)$$

Using the basic commutation relation $[z, p_z] = i\hbar$, it is readily verified that a_z and a_z^\dagger satisfy the commutation relation

$$[a_z, a_z^\dagger] = 1. \quad (4.33)$$

With the aid of the inverse of Eq. (4.32), the axial Hamiltonian becomes,

$$H_z = \hbar\omega_z \left[a_z^\dagger a_z + \frac{1}{2} \right]. \quad (4.34)$$

The corresponding eigenvalues and eigenstates of this motion can be derived using the raising operator introduced in Eq. (4.32),

$$E_k = \hbar\omega_z \left[k + \frac{1}{2} \right], \quad |k\rangle = \frac{(a_z^\dagger)^k}{\sqrt{k!}} |0\rangle, \quad (4.35)$$

and the Hermitian conjugate of the energy states $|k\rangle$ reads,

$$\langle k| = \langle 0| \frac{(a_z)^k}{\sqrt{k!}}. \quad (4.36)$$

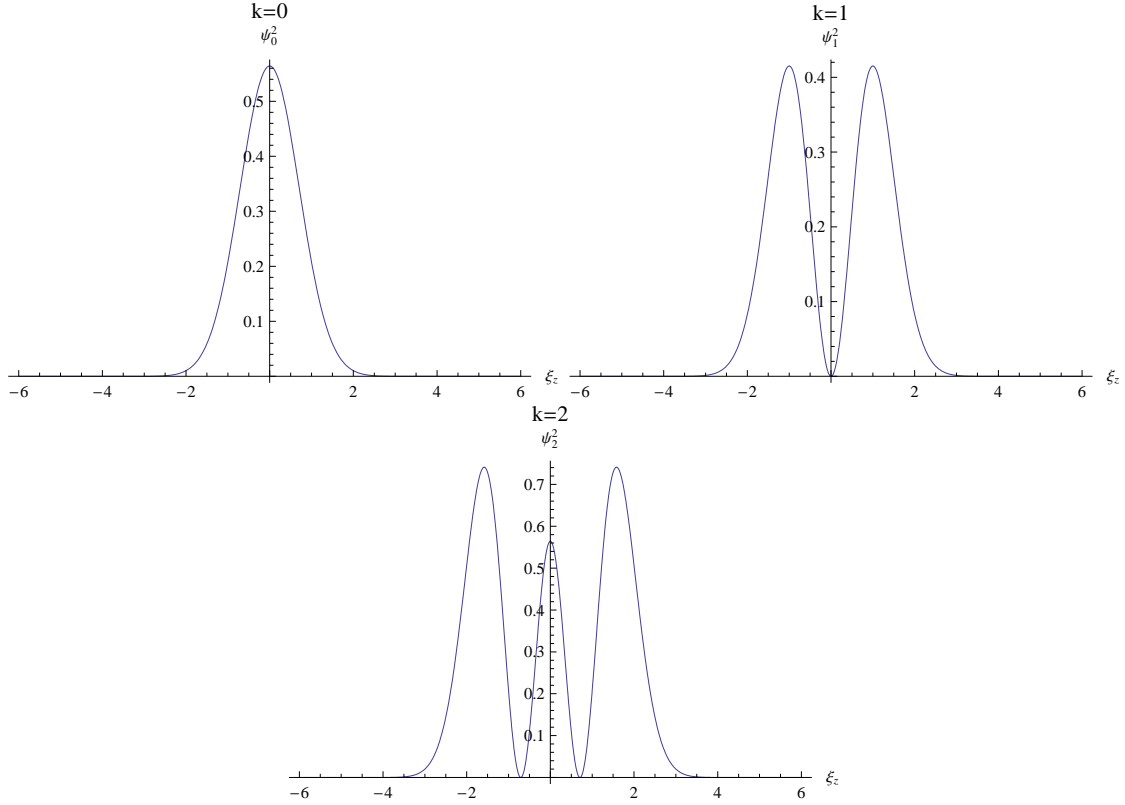


Figure 4.6: The quantum probability densities for the three lowest states of the axial motion of a charged particle in the Penning trap (the Geonium atom) based on Eqs. (4.32) and (4.38) in a Penning trap are shown. Note that $\xi_z = z/\sigma_z$ is the dimensionless parameter, where $\sigma_z = [\hbar/(m\omega_z)]^{1/2}$.

As a result of Eqs. (4.35) and (4.36), the orthonormality condition reads

$$\langle k'|k\rangle = \delta_{k'k}. \quad (4.37)$$

Due to the similarity with the quantum mechanical harmonic oscillator in one dimension, one can use both Eq. (4.32) and

$$\begin{aligned} a_z|k\rangle &= \sqrt{k}|k-1\rangle \\ a_z^\dagger|k\rangle &= \sqrt{k+1}|k+1\rangle, \end{aligned} \quad (4.38)$$

to create the other eigenstates from the ground state $|0\rangle$. We thus draw the probability density of the quantum axial motion for the three lowest quantum numbers $k = 0, 1$ and 2 for a perfect Penning trap in Fig. 4.6. In Fig. 4.6, ξ_z/σ_z is a dimensionless variable and $\sigma_z = [\hbar/(m\omega_z)]^{1/2}$. Moreover, we compare the classical and quantum mechanical probability density for the axial quantum number $k = 15$ in Fig. 4.7.

The question that could be asked is when the quantum description of the axial motion is necessary? If the axial motion is not coupled to a tuned circuit or is coupled very weakly

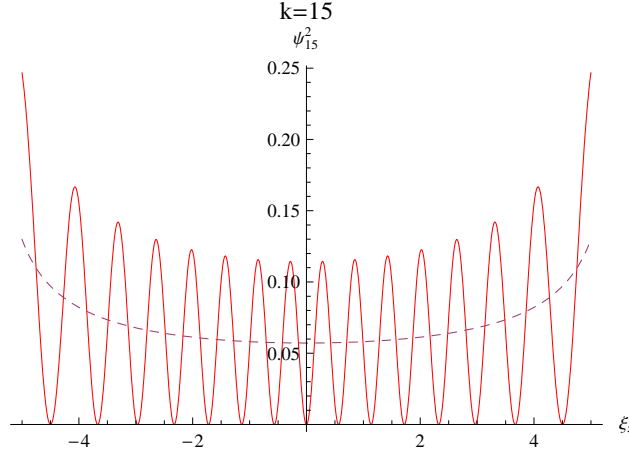


Figure 4.7: The comparison of the quantum probability density for the state $k = 15$ of the axial motion with the corresponding classical probability density (dash line). Note that $\xi_z = z/\sigma_z$ and is the dimensionless parameter, where $\sigma_z = [\hbar/(m\omega_z)]^{1/2}$.

to the radiation field, the quantum description has to be taken into account. Otherwise, the classical description remains valid for the axial motion (at least for an electron or a proton in the Penning trap) [48].

Second, we focus on the quantum cyclotron motion of the charged particle in the Penning trap (the Geonium atom). The corresponding Hamiltonian for this motion can be written in terms of the canonically conjugate variables q and p_q

$$H_c = \frac{1}{2}m\omega_c^2 q^2 + \frac{p_q^2}{2m}, \quad (4.39)$$

where $q = P_x/m\omega_c$ and $p_q = -P_y$. Hence, the raising and lowering operators in this case can be written as follows:

$$\begin{aligned} a_c &= \sqrt{\frac{m\omega_c}{2\hbar}}q + i\sqrt{\frac{1}{2m\hbar\omega_c}}p_q, \\ a_c^\dagger &= \sqrt{\frac{m\omega_c}{2\hbar}}q - i\sqrt{\frac{1}{2m\hbar\omega_c}}p_q, \end{aligned} \quad (4.40)$$

or

$$\begin{aligned} a_c &= \sqrt{\frac{1}{2m\hbar\omega_c}}(P_x - iP_y) \\ a_c^\dagger &= \sqrt{\frac{1}{2m\hbar\omega_c}}(P_x + iP_y). \end{aligned} \quad (4.41)$$

In Eq. (4.41), a_c and a_c^\dagger fulfill the commutation relation $[a_c, a_c^\dagger] = 1$. Like in the axial motion, one can also write Eq. (4.39) in terms of the raising and lowering operators using

Eq. (4.41):

$$H_c = \hbar\omega_c \left(a_c a_c^\dagger + \frac{1}{2} \right). \quad (4.42)$$

In this case, the non-Hermitian raising and lowering operators a_c^\dagger and a_c can also create all eigenstates and eigenvalues, *i.e.*,

$$\begin{aligned} a_c |c\rangle &= \sqrt{c} |c-1\rangle, \\ a_c^\dagger |c\rangle &= \sqrt{c+1} |c+1\rangle, \end{aligned} \quad (4.43)$$

where the cyclotron energy spectrum reads,

$$E_c = \hbar\omega_c \left(c + \frac{1}{2} \right). \quad (4.44)$$

We have depicted the probability density of the cyclotron wave functions for the three lowest cyclotron quantum numbers $c = 0, 1$ and 2 using Eq. (4.41) and Eq. (4.43) [see Fig. 4.8]. Note that we have used the dimensionless variables $\xi_x = x/\sigma_{xy}$ and $\xi_y = y/\sigma_{xy}$ in our wave functions, where $\sigma_{xy} = [\hbar/(m\omega_{xy})]^{1/2}$, in order to draw the probability density for the quantum cyclotron motion. In addition, we compare the classical and quantum mechanical probability density for the cyclotron quantum number $c = 15$ in Fig. 4.9. Third, we continue with the quantum mechanical magnetron motion of the charged particle in the Penning trap (the Geonium atom). Similar to the axial and cyclotron motions, one can define the raising and lowering operators in the case of quantum magnetron motion, *i.e.*,

$$\begin{aligned} a_m &= \sqrt{\frac{1}{2m\hbar\omega_m}} (P_x + iP_y) \\ a_m^\dagger &= \sqrt{\frac{1}{2m\hbar\omega_m}} (P_x - iP_y). \end{aligned} \quad (4.45)$$

Note that the same commutation relation as used for the axial and cyclotron motions holds for the quantum magnetron motion. In this case, the effect of the annihilation and creation operators a_m and a_m^\dagger on the magnetron eigenstates is the same as those operate upon the axial and cyclotron eigenstates, *i.e.*,

$$\begin{aligned} a_m |m\rangle &= \sqrt{m} |m-1\rangle, \\ a_m^\dagger |m\rangle &= \sqrt{m+1} |m+1\rangle, \end{aligned} \quad (4.46)$$

where m is the magnetron quantum number. Therefore, similar to the two previous cases (*i.e.*, the axial and cyclotron motions), the Hamiltonian of the magnetron motion of the charged particle reads:

$$H_m = -\hbar\omega_m \left(a_m a_m^\dagger + \frac{1}{2} \right), \quad (4.47)$$

where the corresponding eigenvalues are

$$E_m = -\hbar\omega_m \left(m + \frac{1}{2} \right). \quad (4.48)$$

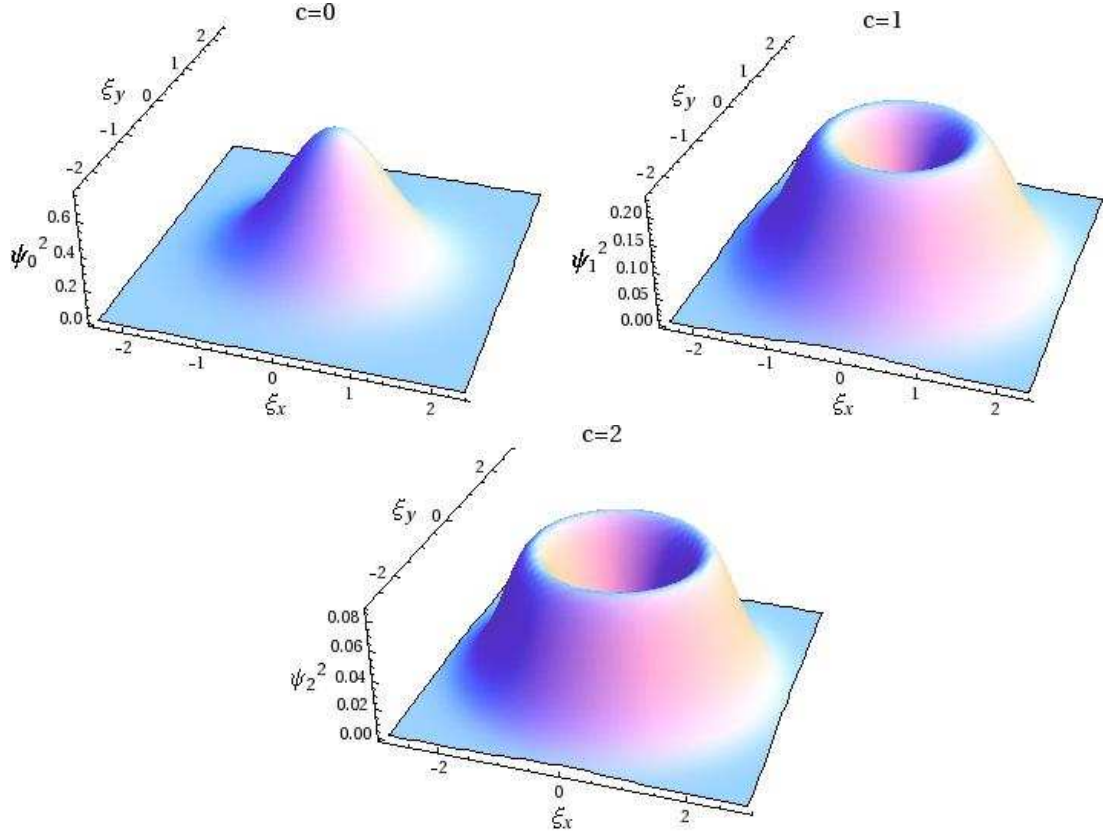


Figure 4.8: The quantum probability densities for the three lowest states of the cyclotron motion of the charged particle in the Penning trap (the Geonium atom) are shown. These are obtained based on Eqs. (4.41) and (4.43) and are shown in $\xi_x \xi_y$ -plane. Note that $\xi_x = x/\sigma_{xy}$ and $\xi_y = y/\sigma_{xy}$ are the dimensionless parameters, where $\sigma_{xy} = [\hbar/(m\omega_{xy})]^{1/2}$.

For a charged particle that populates the states $c = 0$ and 1 with a high probability, the particle spends the majority of its time near these states. For such a particle the cyclotron motion has to be described quantum mechanically. However, the magnetron motion can still be treated classically for both an electron and a proton [48]. This originates from the fact that the magnetron motion has a long radiative decay time, which precludes coupling between the magnetron motion and the black body radiation in the Penning trap [48].

After considering separately the axial, cyclotron and magnetron motions of the charged particle in the Penning trap (the Geonium atom), we can describe the whole quantum mechanical motion of the charged particle in the trap. Due to the similarity between the Hamiltonian of a charged particle in the Penning trap and that of a three-dimensional harmonic oscillator, the eigenstates of the charged particle in the Penning trap can be constructed by using the following normalized states,

$$|k, c, m\rangle = (k! c! m!)^{-1/2} \left[(a_z^\dagger)^k (a_m^\dagger)^c (a_c^\dagger)^m \right] |0, 0, 0\rangle, \quad (4.49)$$

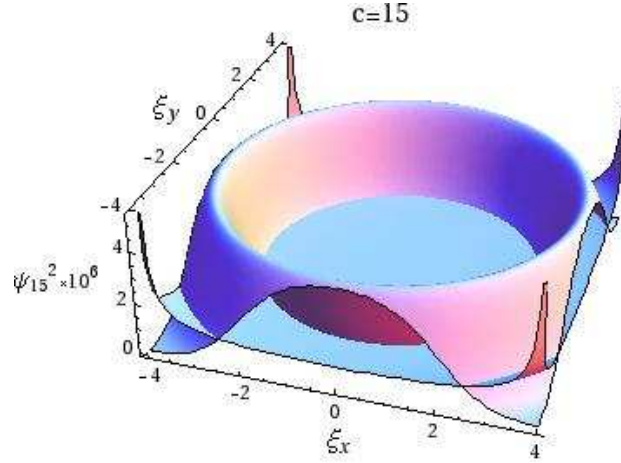


Figure 4.9: A comparison of the quantum probability density for the state $c = 15$ of a cyclotron motion (the curved plane) with the probability density of the corresponding classical cyclotron motion (the horizontal plane) in the $\xi_x \xi_y$ plane. Note that $\xi_x = x/\sigma_{xy}$ and $\xi_y = y/\sigma_{xy}$ are the dimensionless parameters, where $\sigma_{xy} = [\hbar/(m\omega_{xy})]^{1/2}$.

with corresponding eigenvalues

$$E_{kcm} = \hbar\omega_z\left(k + \frac{1}{2}\right) + \hbar\omega_c\left(c + \frac{1}{2}\right) - \hbar\omega_m\left(m + \frac{1}{2}\right). \quad (4.50)$$

In Eq. (4.50), the energy sign in the axial and cyclotron motions is positive, while it is negative for the magnetron case. This refers to the fact that the axial and cyclotron energies increase when their quantum numbers are increased, which means that their energy levels are limited from below, as shown in Fig. 4.11. In the case of the magnetron energy levels, its energy decreases by increasing its quantum number m , due to the fact that it is a metastable motion (as discussed in Sec. 4.2). As a consequence, the magnetron energy levels are turned upside down, as also illustrated in Fig. 4.11.

We draw the quantum mechanical probability density of a charged particle when the contributions of the three quantum motions, *i.e.*, axial, cyclotron and magnetron motions, are taken into account Fig. 4.10.

In order to complete the quantum mechanical investigation of the charged particle in the trap, the spin motion of a trapped particle has to be considered as well. To do so, we express the spin motion in terms of the following spin Hamiltonian

$$H_s = -\boldsymbol{\mu} \cdot \mathbf{B} = \frac{g}{2}\hbar\omega_c\frac{1}{2}\sigma_z, \quad (4.51)$$

where $\boldsymbol{\mu}$ is the Bohr magneton and σ_z refers to spin operator in the z direction. The corresponding eigenvalue of σ_z is

$$E_s = \frac{g}{2}\hbar\omega_c\frac{s}{2}. \quad (4.52)$$

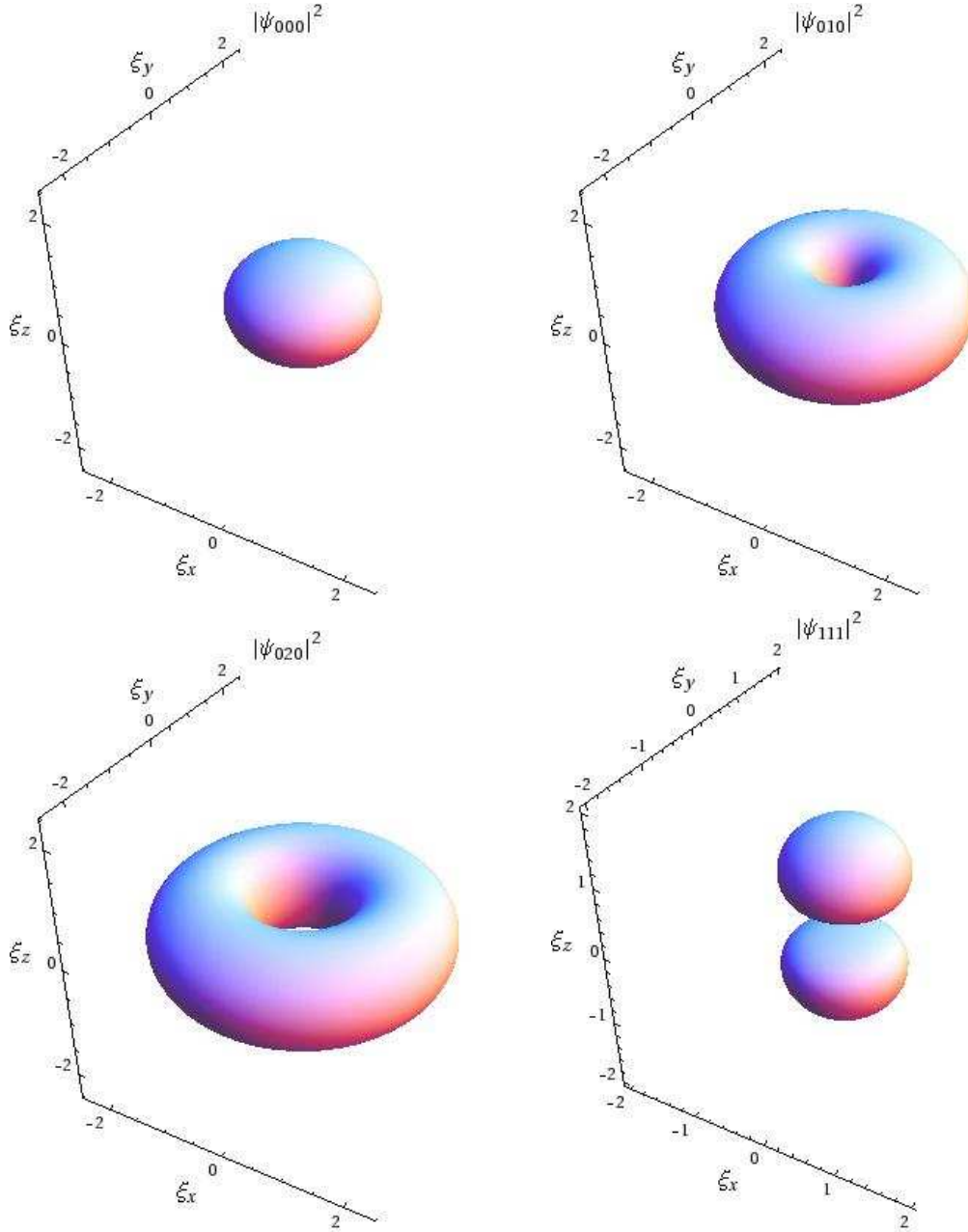


Figure 4.10: The quantum probability densities for the ψ_{000} , ψ_{010} , ψ_{020} and ψ_{111} states of the charged particle in the Penning trap (the Geonium atom) based on Eqs. (4.32), (4.41), (4.45) and (4.49) are shown. The first quantum number refers to the axial quantum number and the rest is for the cyclotron and magnetron quantum numbers, respectively. Here, $\xi_x = x/\sigma_{xy}$, $\xi_y = y/\sigma_{xy}$ and $\xi_z = z/\sigma_z$ are the dimensionless parameters, where $\sigma_{xy} = [\hbar/(m\omega_{xy})]^{1/2}$ and $\sigma_z = [\hbar/(m\omega_z)]^{1/2}$.

For each trapped particle with spin 1/2, there exists two energy levels corresponding to $s = \pm 1$ [see Fig. 4.11]. The energy gap between these levels is $E_s = \hbar\omega_s$, where $\omega_s =$

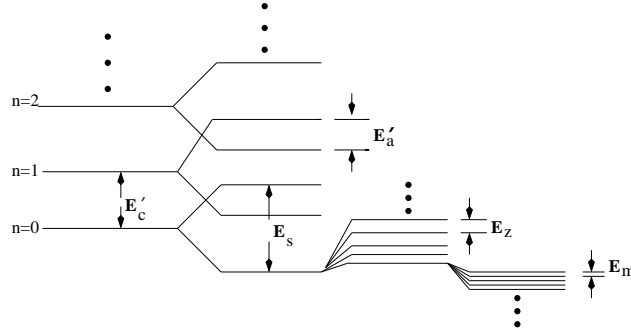


Figure 4.11: The separation of the Geonium atom energy levels for an electron. The first ladder on the left shows the cyclotron energy levels ($E'_c = \hbar\omega'_c$). In the second one, the energy levels are separated by spin $E_s = \hbar\omega_s$. In the third one, the energy levels are split by axial energy $E_z = \hbar\omega_z$. Finally, the magnetron energy $E_m = \hbar\omega_m$ separates the energy levels in opposite direction because its motion is unbound and metastable [48].

$(g/2)\omega_c$ [see Fig. 4.11]. This implies that there is a small difference between the spin precession frequency ω_s and the cyclotron frequency ω_c , as g is not exactly equal to 2 for an electron [48]. The separation among the Geonium energy levels, as shown schematically in Fig. 4.11, is expressed in terms of the anomaly frequency ω_a ,

$$\omega_a = \omega_s - \omega_c. \quad (4.53)$$

The anomaly transition due to the anomaly frequency ω_a is correlated to the two simultaneously upward and downward spin-flip and cyclotron transitions in Fig. 4.11.

However, since there is an electrostatic field in addition to the magnetic field in the Penning trap, the cyclotron frequency is slightly modified to the new value of ω'_c resulting in a change in the separation among the energy levels of the Geonium atom as follows:

$$\omega'_a = \omega_s - \omega'_c. \quad (4.54)$$

This separation is shown in Fig. 4.11 by $E'_a = \hbar\omega'_a$.

The obtained results in this section are valid when the electrostatic and magnetic fields are perfectly aligned with the quadrupole axis. When one considers imperfections due to misalignments of the field directions with the symmetry axis, the results above need to be modified. This concept will be introduced in the next section.

4.4 A real Penning trap

So far, we have considered an ideal Penning trap and described classically and quantum mechanically the motion of a charged particle in it. In reality, the Penning trap suffers a few imperfections. Certainly, they have considerable effects on the accuracy level of measurements. In principle, these imperfections can be categorized into three groups. The

first one is the misalignment of the magnetic field direction with the symmetry axis of the trap electrodes. The second one is related to the higher-order electrostatic imperfections. In fact, adding the harmonic term to the ideal potential Eq. (4.1) gives us this imperfection. The presence of these harmonic terms are originated both from the deviation of an ideal geometry in the trap electrodes and from improperly aligned electrodes shown in Fig. 4.1. Therefore, one can express these imperfections in terms of an infinite series of multiplications of spherical harmonics $Y_l^m(\theta, \varphi)$ and the ratio $(r/z_0)^l$, where r is the radial coordinate and z_0 is the trapping size [see Ref. [48]]. Due to the rapid falling off of the series, the terms $l \geq 6$ can be ignored. The terms $l = 0$ and $l = 1$ vanish because of the symmetrical shape of the Penning trap. The term $l = 5$ can be eliminated due to the inversion symmetry. The terms $l = 3$ and $l = 4$ give rise to an anharmonicity [65]. The contributions of these two terms can not be neglected. Hence, experimentalists usually reduce the effect of these two terms on the high precision measurements by using compensation electrodes [65]. The third one is the so-called harmonic imperfection. It can be represented by adding an extra term to Eq. (4.1), *i.e.*, [48]

$$\phi(x, y) = \frac{1}{2}m\omega_z^2 \left[z^2 - \frac{1}{2}(x^2 + y^2) - \frac{1}{2}\epsilon(x^2 - y^2) \right], \quad (4.55)$$

where ϵ is the single asymmetry parameter.

4.4.1 The invariance theorem

As explained in the previous section, there are a few unavoidable imperfections in the real Penning trap that reduce the accuracy level of a measurement. Experimentally, these imperfections are originated both from the misalignments of the trap electrodes with the magnetic field direction and from the deviation of the ideal geometry of the trap electrodes. In this section, we want to obtain a relation for an exact determination of the cyclotron frequency ω_c , which is free from the above imperfections.

We consider a charged particle in a real Penning trap, which suffers the two general above imperfections. The first imperfection related to the configuration of the Penning trap electrodes and the magnetic field \mathbf{B} can be expressed in a principal-axes coordinate system in terms of the angles θ and φ as follows,

$$\begin{aligned} B_x &= B \sin \theta \cos \varphi, \\ B_y &= B \sin \theta \sin \varphi, \\ B_z &= B \cos \theta. \end{aligned} \quad (4.56)$$

The second one is the harmonic imperfection that is shown by the ϵ parameter in Eq. (4.55). According to the Lorentz force and Newton's second law, one can obtain the

following differential equations of a charged particle in the real Penning trap,

$$\begin{aligned}\ddot{x}(t) - \omega_c \dot{y}(t) \sin \theta \sin \varphi + \omega_c \dot{z}(t) \sin \theta \cos \varphi &= \frac{1}{2} \omega_z^2 (1 + \epsilon) x(t), \\ \ddot{y}(t) - \omega_c \dot{z} \cos \theta + \omega_c \dot{x}(t) \sin \theta \sin \varphi &= \frac{1}{2} \omega_z^2 (1 - \epsilon) y(t), \\ \ddot{z}(t) - \omega_c \dot{x}(t) \sin \theta \cos \varphi + \omega_c \dot{y}(t) \cos \theta &= -\omega_z^2 z(t).\end{aligned}\tag{4.57}$$

Due to the time dependence of the form $e^{-i\omega t}$, one can convert the differential equation introduced in Eq. (4.57) into three homogenous algebraic equations with the determinant,

$$F(\omega^2) = \begin{vmatrix} \omega^2 + \frac{1}{2} \omega_z^2 (1 + \epsilon) & -i\omega\omega_c \cos \theta & i\omega\omega_c \sin \theta \sin \varphi \\ i\omega\omega_c \cos \theta & \omega^2 + \frac{1}{2} \omega_z^2 (1 - \epsilon) & -i\omega\omega_c \sin \theta \cos \varphi \\ -i\omega\omega_c \sin \theta \sin \varphi & i\omega\omega_c \sin \theta \cos \varphi & \omega^2 - \omega_z^2 \end{vmatrix}.\tag{4.58}$$

Eq. (4.58) indicates that the algebraic equation has a solution, provided that $F(\bar{\omega}^2) = 0$, where $\bar{\omega}$ is a measured eigenfrequency. Since the closed form of Eq. (4.58) has 3×3 dimensions, Eq. (4.58) can be matched with the following polynomial form,

$$\begin{aligned}F(\omega^2) &= (\omega^2 - \bar{\omega}_c^2)(\omega^2 - \bar{\omega}_z^2)(\omega^2 - \bar{\omega}_m^2) \\ &= \omega^6 - \omega^4(\bar{\omega}_c^2 + \bar{\omega}_m^2 + \bar{\omega}_z^2) + \omega^2(\bar{\omega}_z^2 \bar{\omega}_m^2 + \bar{\omega}_c^2 \bar{\omega}_z^2 + \bar{\omega}_c^2 \bar{\omega}_m^2) - \bar{\omega}_c^2 \bar{\omega}_z^2 \bar{\omega}_m^2.\end{aligned}\tag{4.59}$$

Note that $\bar{\omega}_c, \bar{\omega}_m$ and $\bar{\omega}_z$ are the measured cyclotron, magnetron and axial frequencies, respectively.

Simplifying further the determinant in Eq. (4.58) gives,

$$\begin{aligned}F(\omega^2) &= \omega^6 - \omega^4 \omega_c^2 + \omega^2 \left[\omega_c^2 \omega_z^2 \left(1 - \frac{3}{2} \sin^2 \theta - \frac{1}{2} \epsilon \sin^2 \theta \cos 2\varphi \right) - \frac{3}{4} \omega_z^4 \left(1 + \frac{\epsilon^2}{3} \right) \right] - \\ &\quad - \frac{1}{4} \omega_z^6 (1 - \epsilon^2).\end{aligned}\tag{4.60}$$

Matching the coefficients of the powers ω^0 , ω^2 and ω^4 in both Eqs. (4.59, 4.60) leads to the following results,

$$\bar{\omega}_c^2 \bar{\omega}_z^2 \bar{\omega}_m^2 = \frac{1}{4} \omega_z^6 (1 - \epsilon^2),\tag{4.61a}$$

$$\bar{\omega}_c^2 \bar{\omega}_z^2 + \bar{\omega}_c^2 \bar{\omega}_m^2 + \bar{\omega}_z^2 \bar{\omega}_m^2 = \omega_c^2 \omega_z^2 \left(1 - \frac{3}{2} \sin^2 \theta - \frac{1}{2} \epsilon \sin^2 \theta \cos 2\varphi \right) - \frac{3}{4} \omega_z^4 \left(1 + \frac{1}{3} \epsilon^2 \right),\tag{4.61b}$$

$$\bar{\omega}_c^2 + \bar{\omega}_z^2 + \bar{\omega}_m^2 = \omega_c^2.\tag{4.61c}$$

Eq. (4.61c) is the so-called ‘‘invariance theorem’’. This relation indicates that the cyclotron frequency ω_c is independent of the misalignment angles θ and φ and the distortion

parameter ϵ that were described in Sec. 4.4. In principle, the invariance theorem provides a prescription that allows us to calculate the cyclotron frequency ω_c in terms of the measured eigenfrequencies of the real Penning trap (*i.e.*, $\bar{\omega}_c$, $\bar{\omega}_m$ and $\bar{\omega}_z$).

Experimentally, the cyclotron frequency ω_c is obtained by measuring $\bar{\omega}_c$, $\bar{\omega}_m$ and $\bar{\omega}_z$, in which the measurement of $\bar{\omega}_c$ is performed to a good level of accuracy, while the measurement $\bar{\omega}_m$ and $\bar{\omega}_z$ is carried out with lesser accuracies [48]. This is because the deviation from an ideal geometry of the trap electrodes imposes a very weak perturbation to the cyclotron motion of the ion in a strong magnetic field, yielding [48]

$$\bar{\omega}_c^2 \gg \bar{\omega}_z^2 \gg \bar{\omega}_m^2. \quad (4.62)$$

According to Eq. (4.62), $\bar{\omega}_z = \omega_z$ and Eq. (4.61a) yields

$$\bar{\omega}_m = \tilde{\omega}_m = \frac{\bar{\omega}_z^2}{2\bar{\omega}_c}. \quad (4.63)$$

By adding $\tilde{\omega}_m^2$ to the both sides of Eq. (4.61c), we can rewrite the invariance theorem as follows,

$$\omega_c^2 = \bar{\omega}_m^2 - \tilde{\omega}_m^2 + \left[\bar{\omega}_c + \frac{\omega_z^2}{2\bar{\omega}_c} \right]^2. \quad (4.64)$$

After performing some algebraic treatments, Eq. (4.64) is converted to the following form,

$$\frac{\omega_c}{\bar{\omega}_c} = \left[\frac{\tilde{\omega}_m^2}{\bar{\omega}_c^2} \left(\frac{\bar{\omega}_m^2}{\tilde{\omega}_m^2} - 1 \right) + \left(1 + \frac{\bar{\omega}_z^2}{2\bar{\omega}_c^2} \right)^2 \right]^{1/2}. \quad (4.65)$$

Due to the fact that $\tilde{\omega}_m^2 - \bar{\omega}_m^2$ is a small quantity, one can expand Eq. (4.65) around $\tilde{\omega}_m^2 - \bar{\omega}_m^2$ to obtain

$$\begin{aligned} \frac{\omega_c}{\bar{\omega}_c} &= 1 + \frac{1}{2} \left(\frac{\bar{\omega}_z}{\bar{\omega}_c} \right)^2 + \frac{1}{8\bar{\omega}_c^4} \left[\left(\frac{\bar{\omega}_m}{\bar{\omega}_c} \right)^2 - 1 \right] \times \\ &\times \left\{ \frac{\tilde{\omega}_m^4}{(1 + \bar{\omega}_z^2/2\bar{\omega}_c^2)^3} \left[\left(\frac{\bar{\omega}_m}{\bar{\omega}_c} \right)^2 - 1 \right] + \frac{4\tilde{\omega}_m^2\bar{\omega}_c^2}{1 + \bar{\omega}_z^2/2\bar{\omega}_c^2} \right\}. \end{aligned} \quad (4.66)$$

Recalling the hierarchy $\bar{\omega}_c^2 \gg \bar{\omega}_z^2 \gg \bar{\omega}_m^2$, in the second line of Eq. (4.66), the denominator in the first term is approximately equal to unity and the numerator in the second term is equal to $\bar{\omega}_z^4$. Hence Eq. (4.66) simplifies to

$$\frac{\omega_c}{\bar{\omega}_c} = 1 + \frac{1}{2} \left(\frac{\bar{\omega}_z}{\bar{\omega}_c} \right)^2 + \frac{1}{8} \left(\frac{\bar{\omega}_z}{\bar{\omega}_c} \right)^4 \times \left[\left(\frac{\bar{\omega}_m}{\bar{\omega}_c} \right)^2 - 1 \right]. \quad (4.67)$$

In principle, the term $(\bar{\omega}_z/\bar{\omega}_c)^4$ in Eq. (4.67) is in reality, a very small correction $[(\bar{\omega}_z/\bar{\omega}_c)^4 = 10^{-14}]$. Thus by not considering this term, one obtains the relation for the corrected cyclotron frequency $\bar{\omega}_c = \bar{\omega}_+$ for an ideal Penning trap [see Eq. (4.8)]. This means that one can consider the leading order correction; in this approximation, $\bar{\omega}_c^2 \simeq \omega_c^2$ and Eq. (4.61b) can be converted to the following useful form,

$$\bar{\omega}_z^2 \simeq \omega_z^2 \left[1 - \frac{3}{2} \sin^2 \theta \left(1 + \frac{1}{3} \epsilon \cos 2\varphi \right) \right]. \quad (4.68)$$

Inserting Eq. (4.68) into Eq. (4.61a) reveals that

$$\bar{\omega}_m^2 = \frac{\omega_z^4}{4\bar{\omega}_c^2} (1 - \epsilon^2) \left[1 - \frac{3}{2} \sin^2 \theta \left(1 + \frac{1}{3} \epsilon \cos 2\varphi \right) \right]^{-1}. \quad (4.69)$$

After writting Eq. (4.68) in terms of $\bar{\omega}_z$ and substituting that into Eq. (4.69), one can reach the following result,

$$\bar{\omega}_m^2 = \tilde{\omega}_m^2 (1 - \epsilon^2) \left[1 - \frac{3}{2} \sin^2 \theta \left(1 + \frac{1}{3} \epsilon \cos 2\varphi \right) \right]^{-3}. \quad (4.70)$$

Note that the factor $\tilde{\omega}_m$ comes from Eq. (4.63).

Since the misalignment angel θ and the distortion parameter ϵ are much smaller than unity under experimental conditions, Eq. (4.70) becomes

$$\bar{\omega}_m^2 \simeq \tilde{\omega}_m^2 \left(1 - \epsilon^2 + \frac{9}{2} \theta^2 \right). \quad (4.71)$$

Therefore, Eq. (4.67) at the limit of very small θ and ϵ reads

$$\frac{\omega_c}{\bar{\omega}_c} = 1 + \frac{1}{2} \left(\frac{\bar{\omega}_z}{\bar{\omega}_c} \right)^2 + \frac{9}{16} \left(\frac{\bar{\omega}_z}{\bar{\omega}_c} \right)^4 \left(\theta^2 - \frac{2}{9} \epsilon^2 \right). \quad (4.72)$$

4.5 Determination of the true cyclotron frequency

As explained before, the Penning trap is the most suitable device, in which one can perform the most precise measurement to determine the fundamental constants, such as the magnetic moment of the electron and test the fundamental symmetries, such as CPT. In order to achieve these tasks, the determination of true cyclotron frequency with high precision is certainly a requirement. [see Refs. [66, 67]].

In this section, we deal with two different methods for the determination of the true cyclotron frequency of the charged particle in the real Penning trap. The first method is based on the invariance theorem and the second one relies upon a single sideband frequency. Note that the first method is much more precise than the second one. In those experiments, where the high accuracy level of the measurement is required, the former method is preferred.

4.5.1 Determination of the cyclotron frequency based on the invariance theorem

The true cyclotron frequency is not the oscillation frequency of the charged particle in the real Penning trap. Hence, it can not be obtained via an experiment. As mentioned in Sec. 4.4.1, it can be expressed in terms of three measured eigenfrequencies of the charged particle in the real Penning trap, *i.e.*, the trap-modified cyclotron frequency ($\bar{\omega}_c$), the axial frequency ($\bar{\omega}_z$) and the magnetron frequency ($\bar{\omega}_m$), and then obtained via the invariance

theorem [see Eq. (4.61c)]. These three measured eigenfrequencies depend on the two misalignment angles (θ and φ) and the harmonic distortion factor ϵ [see Eq. (4.55)].

The outstanding point of the invariance theorem is that harmonic and improperly aligned magnetic field imperfections (*i.e.*, θ , φ and ϵ) do not influence the true cyclotron frequency ω_c (see Sec. 4.4). However, the anharmonic imperfections mentioned in the previous section could still affect the accuracy of the cyclotron frequency determination. Therefore, the cyclotron frequency, which plays an important role in the determination of the bound-state g factor can be obtained with a high accuracy. This prescription is especially very efficient for more massive particles, which have smaller cyclotron frequencies [65].

4.5.2 Determination of the cyclotron frequency based on one sideband frequency

The sideband frequency is defined as follows,

$$\bar{\omega}_c = \bar{\omega}_+ + \bar{\omega}_-. \quad (4.73)$$

Eq. (4.73) denotes that the sideband frequency connects the magnetron and cyclotron motions in the real Penning trap. Since the sideband frequency $\bar{\omega}_c$ can be measured in the imperfect Penning trap (real Penning trap), it can be expressed in term of the systematic shift $\Delta\bar{\omega}_c$, *i.e.*,

$$\bar{\omega}_c = \omega_c + \Delta\bar{\omega}_c, \quad (4.74)$$

where ω_c is the true cyclotron frequency.

The measured sideband frequency $\bar{\omega}_c = \bar{\omega}_+ + \bar{\omega}_-$ can be interpreted as a true cyclotron frequency ω_c , if the systematic shift $\Delta\bar{\omega}_c$ vanish. In the following, we want to evaluate this systematic shift and show that this systematic shift is really small. In this calculation, we will fully profit from the invariance theorem.

In the following, we substitute Eq. (4.73) into Eq. (4.74) and the systematic shift $\Delta\bar{\omega}_c$ reads,

$$\Delta\bar{\omega}_c = \bar{\omega}_+ + \bar{\omega}_- - \omega_c. \quad (4.75)$$

After dividing both sides of this equation by $\bar{\omega}_c$, Eq. (4.75) reads

$$\frac{\Delta\bar{\omega}_c}{\bar{\omega}_c} = 1 + \frac{\bar{\omega}_-}{\bar{\omega}_+} - \frac{\omega_c}{\bar{\omega}_c}, \quad (4.76)$$

where in the first and second term of the right hand side of Eq. (4.76), $\bar{\omega}_c = \bar{\omega}_+$ is assumed.

Due to the hierarchy $\bar{\omega}_c^2 \gg \bar{\omega}_z^2 \gg \bar{\omega}_m^2$, Eq. (4.8) for the measured eigenfrequencies can be expanded (for small $\bar{\omega}_z$)

$$\bar{\omega}_- \simeq \frac{\bar{\omega}_z^2}{2\bar{\omega}_+} + \frac{\bar{\omega}_z^4}{4\bar{\omega}_+^3} + \dots \quad (4.77)$$

At the limit of very small $\theta \ll 1$ and $\epsilon \ll 1$, Eq. (4.68) reads,

$$\bar{\omega}_z^2 \simeq \omega_z^2 \left(1 - \frac{3}{2}\theta^2\right) + \dots \quad (4.78)$$

Inserting Eq. (4.78) into Eqs. (4.77 and 4.72) leads to the following results, respectively,

$$\bar{\omega}_- \simeq \frac{\omega_z^2}{2\bar{\omega}_+} \left(1 - \frac{3}{2}\theta^2\right) + \dots, \quad (4.79a)$$

$$\frac{\omega_c}{\bar{\omega}_c} \simeq 1 + \frac{1}{2} \left(\frac{\omega_z}{\bar{\omega}_c}\right)^2 \left(1 - \frac{3}{2}\theta^2\right) + \frac{9}{16} \left(\frac{\omega_z}{\bar{\omega}_c}\right)^4 \left(\theta^2 - \frac{2}{9}\epsilon^2\right). \quad (4.79b)$$

Substituting Eqs. (4.79a and 4.79b) into Eq. (4.76) leads to the following result,

$$\frac{\Delta\bar{\omega}_c}{\bar{\omega}_c} \simeq \frac{\omega_z^4}{4\bar{\omega}_c^4} \left(\frac{1}{2}\epsilon^2 - \frac{9}{4}\theta^2\right). \quad (4.80)$$

Note that in the derivation of Eq. (4.80) the leading order of the first relation in Eq. (4.79) is taken into account.

Inverting Eq. (4.78) in terms of $\bar{\omega}_z^2$ and putting it in Eq. (4.80) give us

$$\frac{\Delta\bar{\omega}_c}{\bar{\omega}_c} \simeq \frac{\bar{\omega}_z^4}{4\bar{\omega}_c^4} \left(\frac{1}{2}\epsilon^2 - \frac{9}{4}\theta^2\right). \quad (4.81)$$

Considering the relation $\bar{\omega}_z^2 \simeq 2\bar{\omega}_c\bar{\omega}_-$, Eq. (4.81) becomes

$$\Delta\bar{\omega}_c \simeq \left(\frac{9}{4}\right) \left(\frac{\bar{\omega}_-^2}{\bar{\omega}_c}\right) \left(\frac{2}{9}\epsilon^2 - \theta^2\right). \quad (4.82)$$

If one puts $\bar{\omega}_- \simeq \bar{\omega}_z^2/2\bar{\omega}_c$ into Eq. (4.82), one will obtain the prefactors that also appeared in the third term of Eq. (4.79b), which means that there is consistency between these two equations.

Eq. (4.82) indicates that the systematic shift $\Delta\bar{\omega}_c$ is of the order the ratio of the magnetron frequency and the measured cyclotron frequency, which is much smaller than the cyclotron frequency due to the hierarchy of the frequencies ($\bar{\omega}_- \ll \bar{\omega}_z \ll \bar{\omega}_+$) for a charged particle in a real Penning trap. In addition, Eq. (4.82) depends on the square of the misalignment θ and harmonic distortion ϵ , but it does not depend on the mass and the charge of the particle in the lowest order.

4.6 Partial summary and tentative concluding remarks

The main idea of this thesis is related to the proposals for the bound-electron g -factor determination, which is performed in the Penning trap. To this end, in this chapter, we described the Penning trap and the significance of its applications on the area of high precision measurements. We obtained the typical trajectory of a charged particle in two combined quadrupole electrostatic and magnetic fields (the Geonium atom) [see Fig. 4.2 and Fig. 4.3]. Also, the trajectory of a charged particle in a Penning trap was mapped out in the presence of an additional electric field [see Fig. 4.5]. For a small electric field, we

found that it does not have a significant effect on the ion trajectory. This finding also has an essential role in the three-photon, double-resonance excitation arrangement related to the bound-electron g -factor determination, which will be illustrated in Chapter 5. Based on the similarity between the Hamiltonian of the Geonium atom with the Hamiltonian of a particle in a three dimensional harmonic potential, we described the quantum dynamics of the Geonium atom via two different methods. The first one was based on the Schrödinger equation and the second one relied on the lowering and raising operators. Based on these methods, we were able to explain separately the axial, cyclotron and magnetron motions of a charged particle, which lead to the general wavefunction of a charged particle in the Penning trap (the Geonium atom). Due to the unavoidable imperfections in the Penning trap, we considered the real Penning trap and recalculated the invariance theorem, which has a significant application in the area of high-precision measurement of a bound-electron g factor [see Chapter 5]. We utilized two methods, *i.e.*, the invariance theorem (Sec. 4.5.1) and one side band frequency (Sec. 4.5.2) in order to obtain the true cyclotron frequency. Since the determination of the true cyclotron frequency based on the first method yields a more precise result than the second one, it is always used in those experiments that need high precision (such as bound-electron g -factor measurements), while the second method based on one side band frequency is useful for those experiments, which do not need the high precision.

Chapter 5

Proposals for measurement of the bound-electron g factor

5.1 Introduction

Electromagnetic interactions are well understood in terms of quantum electrodynamics (QED). Many experiments in the field of atomic as well as sub-atomic physics have confirmed the theoretical predictions of QED with great precisions. The well-known experiments are the measurements of the Doppler-free, two-photon $1S$ – $2S$ transition frequency and free- and bound- electron g factor. An excellent agreement between the experimental and theoretical values of the g factor for a free- and bound- electron has clearly demonstrated the success of the theory of quantum electrodynamics [68]. For the free electron, these values are $g_{exp} = 2.002\,319\,304\,360\,(56)$ and $g_{th} = 2.002\,319\,304\,3718\,(75)$ [63, 69] and for a bound-electron, we have $g_{exp}(^{12}\text{C}^{5+}) = 2.001\,041\,5663\,(10)(56)$ and $g_{th}(^{12}\text{C}^{5+}) = 2.001\,041\,5901\,(3)$ [70].

Since both the theoretical and experimental values for the bound-electron g factor have impinged upon the uncertainty of the electron mass [71], any advances in the theoretical and experimental investigations of the magnetic moments of a bound system is required to raise the accuracy level [62, 72]. The magnetic moments of the bound electron in $^{12}\text{C}^{5+}$, $^9\text{Be}^+$ and $^6\text{O}^{7+}$ have been measured with a high precision [73, 62, 74]. The present accuracy of the experimental results for Hydrogen-like carbon as well as oxygen is already below one part per billion level and is likely to be improved in the near future.

In this chapter, we introduce two different proposals in which the accuracy level of a bound-electron g -factor value could be improved. The motivation behind the current chapter is the applicability of the ultra-high precision atomic laser spectroscopy techniques in measuring the bound-electron g factor and the $1S$ – $2S$ transition frequency via two-photon spectroscopy of Helium ion. In Sec. 5.2 of this chapter, we explain the experimental and theoretical aspects of g factor. This section comprises of a general description of the g factor, experimental setup, that is applied for measuring the bound-electron g factor in a Penning trap, the theoretical aspects of a free- and bound-electron g factor as well as QED

corrections related to the bound-electron g factor. Based on this study, the g factor of $^4\text{He}^+$ ion in its ground state is obtained in which the QED corrections are taken into account. In Sec. 5.3, the first proposal for measurement of the bound-electron g factor based on the idea of two-photon, double-resonance excitation arrangement is introduced. In Sec. 5.4, the second proposal for measurement of the bound-electron g factor relied on three-photon, double resonance excitation arrangement is studied. The latter setup could also be applied to measure the $1S-2S$ and $1S \Leftrightarrow n'S, n' \rightarrow \infty$ transition frequencies in $^4\text{He}^+$. These frequency measurements, as the third proposal, are explained in Sec. 5.5. The partial summary and tentative concluding remarks are given in Sec. 5.6. Three appendices elucidate the calculation of different theoretical data that were used for the two proposals. In Appendix. A, the calculation of quenching effect on the lifetime of metastable $2S$ state is introduced. In Appendix. B, Breit-Rabi diagram, due to the effect of the magnetic field of a Penning trap on the $2P_{1/2}(m_j = \pm 1/2)$ and $2S_{1/2}(m_j = \pm 1/2)$ states, is obtained. In Appendix. C, the calculation related to the relativistic and the leading order of QED contributions of g factor for various states is presented. In Appendix. D, we also introduce the relativistic and QED corrections, which are related to the energy value of $1S$ and $2S$ states in Helium ion.

5.2 Experimental and theoretical aspects of g factor

In this section, we consider the experimental and theoretical significance of free- and bound-electron g factor. In the experimental discussions of this section, we express the g factor of an electron in terms of the Larmor frequency of the electron and cyclotron frequency of an ion. These frequencies are accurately measured via the experimental setup so-called the double-trap technique (explained below). In the theoretical considerations of this section, the deviation of a free- and bound-electron g factor from the Dirac value is explained by introducing the corresponding expansions in terms fine-structure constant α and binding effects $Z\alpha$. In the case of the bound-electron g factor, the relativistic and QED corrections for Helium ion is calculated. This investigation provides a theoretical background for the two proposed excitation arrangements related to the bound-electron g -factor measurement in Helium ion [for details of the two excitation arrangements see Secs. 5.3 and 5.4].

5.2.1 General description

This section introduces general characteristics of the bound-electron g factor. The direct relation between the magnetic moment $\boldsymbol{\mu}$ and the bound-electron g factor can be expressed in terms of its total angular momentum \boldsymbol{J} as follows,

$$\boldsymbol{\mu} = -g_j \mu_0 \boldsymbol{J}, \quad (5.1)$$

where $\mu_0 = e\hbar/m_e$ is the Bohr magneton. Note that Eq. (5.1) is given in the units of the Bohr magneton. Here, e and m_e are the charge and the mass of an electron, respectively.

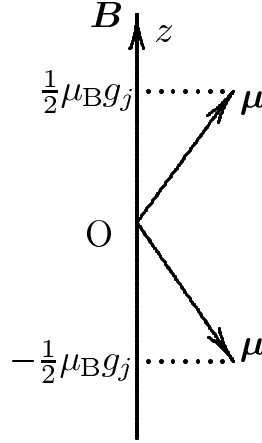


Figure 5.1: The spin of a spin-1/2 particle (e.g., an electron) and the magnetic moment μ have two potential orientations in an external magnetic field. The \mathbf{B} field is in z direction. g_j is the bound-electron g factor. Here, μ_B refers to the Bohr magneton.

In the presence of a magnetic field \mathbf{B} (in z direction) in a Penning trap, the energy difference between two spin directions of the bound electron reads

$$\Delta E = -\boldsymbol{\mu} \cdot \mathbf{B} = g_j \frac{e\hbar}{2m_e} B_z. \quad (5.2)$$

If we define the cyclotron frequency of the electron $\omega_c^e = eB_z/m_e$, Eq. (5.2) becomes

$$\Delta E = \frac{\hbar}{2} g_j \omega_c^e. \quad (5.3)$$

If a magnetic moment μ is immersed in a steady \mathbf{B} field in the z direction [see Fig. 5.1], the magnetic moment will precess about the z axis with the classical Larmor frequency ω_L . A measurement of the magnetic moment is made through inducing a spin-flip of the magnetic moment between the two states parallel and antiparallel to the \mathbf{B} field [see Fig. 5.1]. The energy difference between two states is equal to $\Delta E = \hbar\omega_L$. Therefore, the g factor reads

$$g_j = 2 \frac{\omega_L}{\omega_c^e}. \quad (5.4)$$

Eq. (5.4) indicates that the bound-electron g factor can be obtained if the Larmor and cyclotron frequency of the bound electron are measured. From the experimental point of view, the measurement of the cyclotron frequency of the bound electron is a formidable task. In other words, Eq. (5.4) is not a suitable way to obtain the bound-electron g factor. The possible way to measure the bound-electron g factor is to use the cyclotron frequency of an ion, since it can be measured experimentally. In this fashion, one can write Eq. (5.4) in terms of the cyclotron frequency of an ion, *i.e.*,

$$g_j = 2 \frac{\omega_L}{\omega_c} \frac{\omega_c}{\omega_c^e}, \quad (5.5)$$

where the cyclotron frequency of an ion $\omega_c = (QB)/M$. Therefore, Eq. (5.5) reads

$$g_j = 2 \frac{\omega_L}{\omega_c} \frac{Q/M}{e/m_e}, \quad (5.6)$$

where Q and M are the charge and mass of an ion, respectively. Eq. (5.6) indicates that the determination of the bound electron g factor depends only on the measurement of the ratio of $\frac{\omega_L}{\omega_c}$. We will deal with this concept in the next section.

5.2.2 Experimental setup for the measurement of the bound-electron g factor

The cyclotron and the Larmor frequencies are the two important inputs for measuring the bound-electron g factor [see Eq. (5.6)]. We discuss how the cyclotron and the Larmor frequencies are measured in a Penning trap.

In the Penning trap experiment, two nearly identical traps placed 2.7 cm apart from each other in the magnetic field directions are utilized [75]. According to Fig. 5.2, a stack of 13 cylindrical electrodes of 7 mm inner diameter is included in these traps. In the first trap, a nickel ring electrode is used to distort the homogeneity of the magnetic field. In the second trap, a copper electrode is used and the magnetic field remains homogenous, because copper is non magnetic and does not distort the magnetic field. As it will be explained below, the inhomogeneity of the magnetic field plays an important role in analyzing the direction of the electron spin via the continuous Stern-Gerlach effect and also limits the accuracy of the g factor measurement [see Sec. 5.2.3]. The two traps are the so-called “analysis trap” and “precision trap”, respectively [see Fig. 5.2].

A typical ion is consecutively confined in these two separated traps in order to achieve a high-precision measurement. In each trap, the charged particle (an ion) is stored in a combination of a homogeneous magnetic field \mathbf{B}_0 and an electrostatic quadrupole potential [see Chapter 4]. The particle is confined by the magnetic field in the plane perpendicular to the direction of the magnetic field, and the electrostatic potential is responsible to confine the charged particle in the direction parallel to the magnetic field lines. Due to this configuration shown in Fig. (4.1), the three produced characteristic motions are the trap-modified cyclotron motion $\bar{\omega}_+$, the magnetron motion $\bar{\omega}_-$, which is a circular $\mathbf{E} \times \mathbf{B}$ drift motion perpendicular to the magnetic field lines, and the axial motion $\bar{\omega}_z$ [60]. Therefore, the cyclotron frequency ω_c of the charged particle can be obtained from the experimentally measured eigenfrequencies by using the invariance theorem, [see Sec. 4.5.1]

$$\omega_c = \sqrt{\bar{\omega}_+^2 + \bar{\omega}_-^2 + \bar{\omega}_z^2}. \quad (5.7)$$

Measuring the g factor needs not only the cyclotron frequency ω_c , but also the Larmor frequency ω_L [see Eq. (5.6)]. The resonant excitation of the transition between the two spin states of the bound electron within the magnetic field of the Penning trap enables one to measure the Larmor frequency ω_L . The experimental method for measuring the Larmor

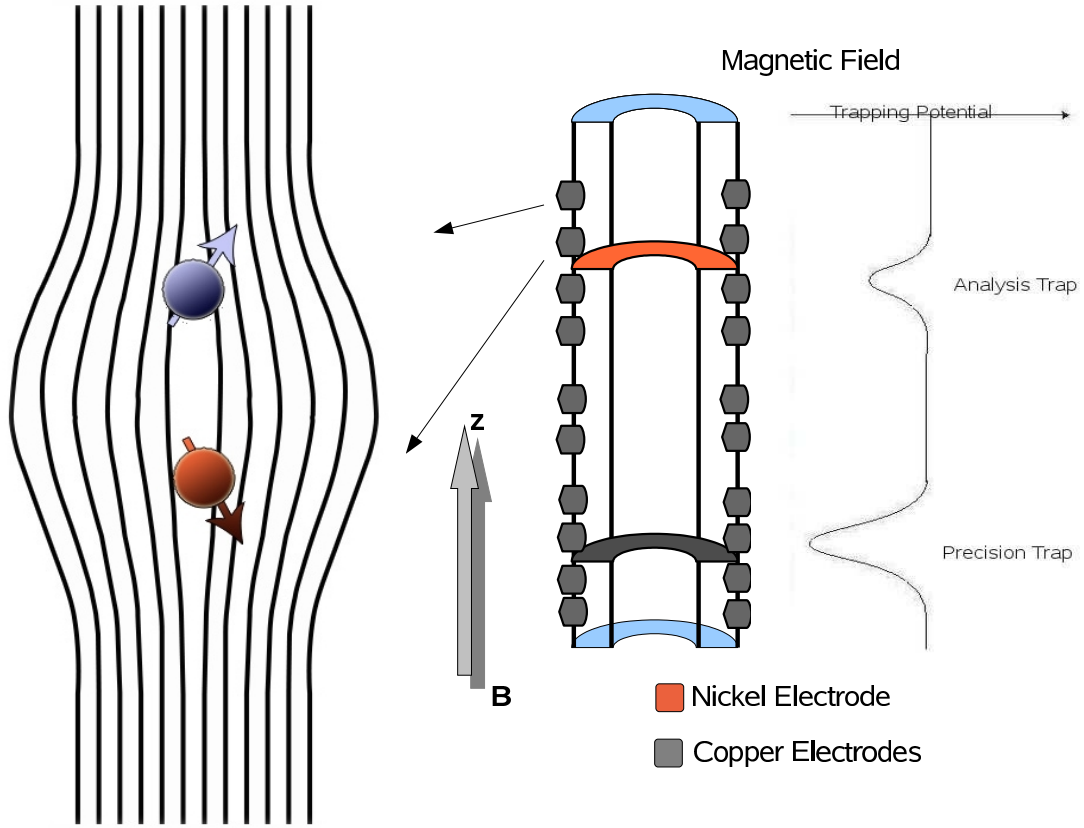


Figure 5.2: Scheme of the double Penning trap setup used for g -factor measurements of the bound electron.

frequency was first introduced by Dehmelt [67], and is called quantum jump or spin-flip transition. In this method, a microwave field in resonant with the Larmor frequency ω_L is applied between the two spin states $m_s = \pm 1/2$. The spin state m_s is analyzed in a subsequent quantum nondestructive measurement by determining the axial frequency of the ion. The spin-flip transitions are detected as discrete changes of the axial frequency of the ion. These transitions are observed through the continuous Stern-Gerlach effect. The number of spin-flip transitions is then counted for a fixed time interval. About every seven minutes, one quantum jump is observed near the resonance frequency. With changing the microwave frequency, the measurement procedure is repeated at about 20 different excitation frequencies. Finally, the resonance spectrum of the Larmor frequency can be obtained by plotting the quantum jump rate versus the excitation frequency. Note that the measurement of the spin-flip rate for at the microwave frequency $\omega_{MW} \approx \omega_L$ is performed simultaneously with the measurement of the cyclotron frequency, which will be discussed in the next section.

5.2.3 Continuous Stern–Gerlach effect and the double-trap technique

In this section, we deal with the Continuous Stern-Gerlach effect and explain why we need the analysis trap and precision trap for bound-electron g -factor measurements.

The effect of the inhomogeneous magnetic field on the spin of a particle results in a measurable difference of its oscillation frequency for various spin directions. This effect is called by Dehmelt “the continuous Stern-Gerlach effect”. The exact measurement of the particle oscillation frequency yields useful information on the spin orientation of the particle. Due to the presence of the inhomogeneous field in the analysis trap, the direction of the electron spin can be analyzed via the continuous Stern-Gerlach effect [76].

This inhomogeneity plays a key role in the determination of the spin orientation of an electron. However, the inhomogeneity precludes the high accuracy level of the measurement. In order to overcome this drawback, a double-trap technique is usually applied in the Penning trap experiment. According to this technique, a spatial separation between two traps, one inducing the spin-flips and the other analyzing the spin direction, improves the accuracy level of the measured magnetic moment by three orders of magnitude [73]. After determining the spin orientation of the particle in the analysis trap, the particle is transferred into the precision trap and the microwave field is radiated to induce a spin-flip. After an interaction time of about 80 s the charged particle is returned to the analysis trap. Once again, the spin orientation is analyzed in the analysis trap by an additional spin-flip in order to determine correctly the spin direction of the particle when it comes back the analysis trap. This new determination of the spin-flip reassures whether or not the axial frequency is altered relative to its value before entering to the precision trap.

When a charged particle is in the precision trap, its cyclotron frequency is measured simultaneously with the interaction with the microwave frequency. The simultaneous measurement of Larmor and cyclotron frequencies, which is possible in the double trap setup makes it possible to measure g factor to a high accuracy.

5.2.4 Theoretical aspects of g factor

After dealing with the experimental issues of the g factor, in this section, we focus on the theoretical considerations of g factor of a free- and bound-electron. We introduce corrections that result in the modification of the free- and bound-electron g factor values. Based on this investigation, we calculate the modified value of the bound-electron g factor of ${}^4\text{He}^+$ in its ground state, which will be used in the description of the proposed excitation arrangement for the measurement of $1S$ bound-electron g factor in Secs. 5.3 and 5.4.

As a starting point, we briefly explain a free electron g factor. If we set $\mathbf{J} = \mathbf{S}$ in Eq. (5.1) and use the Dirac equation with minimal coupling of the electromagnetic field, it results the value of the free-electron g factor, which is $g_{\text{Dirac}} = 2$ [77]. Experimental evidences showed that this value has a deviation from the g factor predicted by the Dirac equation [78, 79]. There are two reasons for this discrepancy, which are explained in the framework of QED and the standard model. The first one is related to an electron self-

interaction, *i.e.*, the exchange of virtual photons. The second one, so-called non-QED contributions, is due to electron interactions with virtual weak bosons W and Z as well as hadronic loop insertions in the photon propagator, which result in a slight modification of free-electron g factor [80]. These modifications can be expressed as an expansion in terms of QED loop expansion parameter α along with non-QED terms, as shown in Eq. (1.1). We show the non-QED terms by a_{hadronic} and a_{weak} . The deviation of g from the Dirac value due to taking into account the effect of non-QED corrections is 1.7×10^{-12} , which is very small [81]. According to Eq. (1.1), the fine structure constant α ($\alpha \approx 1/137.036$) serves as an input parameter for the determination of the g factor. The fine-structure constant is very small and the various orders of Feynman diagrams have been envisaged as a series expansion. In high orders, the series drops off rapidly and converges. Hence, the perturbation theory is a safe method to obtain the g factor of the free electron. The coefficients introduced in Eq. (1.1) are known until the fourth order of α/π , [80]

$$\begin{aligned} A_1 &= \frac{1}{2}, \\ A_2 &\approx -0.3\,284\,789\,656, \\ A_3 &\approx 1.1\,812\,415, \\ A_4 &= -1.7283(35). \end{aligned} \tag{5.8}$$

For a bound electron, we have a different situation. In the case of the bound-electron g factor, this value is modified because of two reasons: (*i*) electron interaction with an external Coulomb field, which modifies the properties of the electron (*ii*) the electron self-interaction (the exchange of virtual photons). These modifications of the bound-electron g factor play an essential role in an accurate determination of the electron mass. The recent and accurate determination of the electron mass based on g_{bound} has nearly reached the experimental precision of 0.5 ppb (parts per billion) [73]. The experimental setup for the measurement of the electron mass is based on the simultaneous measurement of the cyclotron frequency of the ion and the Larmor frequency of the electron in the Penning trap as described in Sec. 5.2.2.

As already mentioned, the electron self-interaction and electron interaction with an external Coulomb field modify the bound-electron g factor value. One can express the deviation from the Dirac value in terms of a series expansion, such as free-electron g factor [see Eq. (1.1)]. As opposed to the series expansion of the free-electron g factor, where the coefficients are constant, in the series expansion of the bound-electron g factor, they depend on the binding effects $Z\alpha$, *i.e.*,

$$g = g^{(0)} + f_1(Z\alpha)\frac{\alpha}{\pi} + f_2(Z\alpha)\left(\frac{\alpha}{\pi}\right)^2 + f_3(Z\alpha)\left(\frac{\alpha}{\pi}\right)^3 + \dots \tag{5.9}$$

In Eq. (5.9), the first part refers to the Breit term originated from solving the Dirac equation for a bound system which shows the deviation of g factor from $g_{\text{Dirac}} = 2$, due to binding effects (explained below) and the rest assign to the QED corrections with the coefficient functions $f_j(Z\alpha)$. Eq. (5.9) denotes that the bound-electron g factor depends

on not only the ratio α/π but also the binding effect $Z\alpha$. The nuclear charge Z may not be a small number. Thus, higher orders, in contrast to the free-electron g factor, can not be ignored. This implies that the non-perturbative methods is applicable for the bound-electron g factor. It is interesting to note that in the limit $Z\alpha \rightarrow 0$, one revisits the series expansion of the free-electron g factor Eq. (1.1).

For a bound-electron g factor, in order to reach the experimental precision, the values of the coefficient functions $f_j(Z\alpha)$ in Eq. (5.9) must be calculated. In the framework of NRQED (nonrelativistic QED), these coefficient functions are known up to the second order of (α/π) in Eq. (5.9), due to taking into account the loop effects (the electron self-interaction) [82]. With considering the first and second loop corrections in Eq. (5.9), the modified value for the bound-electron g factor in nS state reads [83]

$$g = g^{(0)} + g_{\text{loop}}^{(1)} + g_{\text{loop}}^{(2)} + \mathcal{O}(\alpha^3), \quad (5.10)$$

where each correction is as follow,

$$\begin{aligned} g^{(0)} &= 2 - \frac{2}{3} \frac{(Z\alpha)^2}{n^2} + \left(\frac{1}{2n} - \frac{2}{3}\right) \frac{(Z\alpha)^4}{n^3} + \mathcal{O}(Z\alpha)^6, \\ g_{\text{loop}}^{(1)} &= \left(\frac{\alpha}{\pi}\right) \left[2 \times \frac{1}{2} \left(1 + \frac{(Z\alpha)^2}{6n^2}\right) + \frac{(Z\alpha)^4}{n^3} \left(a_{41} \ln[(Z\alpha)^{-2}] + a_{40}\right) + \mathcal{O}(Z\alpha)^5 \right], \\ g_{\text{loop}}^{(2)} &= \left(\frac{\alpha}{\pi}\right)^2 \left[-0.656958 \left(1 + \frac{(Z\alpha)^2}{6n^2}\right) + \frac{(Z\alpha)^2}{n^3} \left(b_{41} \ln[(Z\alpha)^{-2}] + b_{40}\right) + \mathcal{O}(Z\alpha)^5 \right], \end{aligned} \quad (5.11)$$

where $a_{41}(nS) = 32/9$, $b_{41}(nS) = 56/9$ and $b_{40}(1S) = -18.5(5.5)$. In Eq. (5.11), $a_{40}(nS)$ reads

$$a_{40}(nS) = \frac{73}{54} - \frac{5}{24n} - \frac{8}{9} \ln k_0(nS) - \frac{8}{3} \ln k_3(nS), \quad (5.12)$$

where the Bethe logarithms $\ln k_0$ and $\ln k_3$ have explicit values $\ln k_0(1S) = 2.984\,128\,555$ and $\ln k_3(1S) = 3.272\,806\,545$.

In Eq. (5.10), to reach the experimental accuracy of bound-electron g factor it is necessary to consider more corrections to bound-electron g factor. Here, we only explain the recoil correction, which is associated with the finite mass of the nucleus. Its contribution to the bound-electron g factor, as obtained in Ref. [84] reads

$$g_{\text{recoil}} = \frac{4}{3} (Z\alpha)^4 m_e^2 R^2, \quad (5.13)$$

where the rms nuclear charge distribution radius R is 1.673(1) fm (“old” value) and 1.680(5) fm (“new” value) [85].

We have summarized these corrections that are relevant to the 10^{-12} level of accuracy of $1S$ bound-electron factor of ${}^4\text{He}^+$ in Table 5.4. These corrections are obtained for the two different values of the fine-structure constant α .

Table 5.1: Individual contributions to the $1S$ bound-electron g factor for ${}^4\text{He}^+$. In the labeling of the corrections, we follow the conventions of Ref. [86]. The abbreviations used are as follows: “h.o.” stands for a higher order contribution, “SE” for a self energy correction, “VP-EL” for the electric-loop vacuum-polarization correction, and “VP-ML” for the magnetic-loop vacuum-polarization correction. The value of $\alpha^{-1} = 137.035\,999\,070(98)$ is the currently most accurate value from Refs. [66], whereas the value of $\alpha^{-1} = 137.035\,999\,11(46)$ is the 2002 CODATA recommended value [69].

Corrections		$\alpha^{-1} = 137.035\,999\,070(98)$	$\alpha^{-1} = 137.035\,999\,11(46)$
Dirac eigenvalue		1.999 857 988 825 2(2)	1.999 857 988 825 3(9)
Finite nuclear size		0.000 000 000 002 3	0.000 000 000 002 3
One-loop QED	$(Z\alpha)^0$	0.002 322 819 466 0(17)	0.002 322 819 465 4(76)
	$(Z\alpha)^2$	0.000 000 082 462 2	0.000 000 082 462 2
	$(Z\alpha)^4$	0.000 000 001 976 7	0.000 000 001 976 7
	h.o.,SE	0.000 000 000 035 1(2)	0.000 000 000 035 1(2)
	h.o.,VP-EL	0.000 000 000 002 0	0.000 000 000 002 0
	h.o.,VP-ML	0.000 000 000 000 2	0.000 000 000 000 2
\geq two-loop QED	$(Z\alpha)^0$	-0.000 003 515 096 9(3)	-0.000 003 515 096 9(3)
	$(Z\alpha)^2$	-0.000 000 000 124 8	-0.000 000 000 124 8
	$(Z\alpha)^4$	0.000 000 000 002 4(1)	0.000 000 000 002 4(1)
Recoil	m/M	0.000 000 029 198 5	0.000 000 029 198 5
Radiative recoil	$(m/M)^2$	-0.000 000 000 025 3	-0.000 000 000 025 3
Hadronic/weak interaction		0.000 000 000 003 4	0.000 000 000 003 4
Total		2.002 177 406 727 1(17)	2.002 177 406 726 5(77)

5.2.5 g factor of an electron in Hydrogen-like atom

As mentioned, the electron interaction with an external Coulomb field modifies the bound-electron g factor value. In this section, the correction to the bound-electron g factor due to an electron interaction with a Coulomb field of a nucleus with charge Ze is calculated. This correction is the so-called relativistic binding corrections.

In the relativistic quantum theory, the first theoretical investigation on the bound-electron g factor in the Coulomb field of a nucleus with a charge Ze was performed by Breit in 1928 [87]. The usual procedure to calculate the modified value of a bound-electron g factor is to compute the energy shift of the state ϕ_n in the presence of an external magnetic field, *i.e.*,

$$\Delta E = -\langle \phi_n | \boldsymbol{\mu} \cdot \mathbf{B} | \phi_n \rangle = m_j g_j \mu_0 B, \quad (5.14)$$

where $\boldsymbol{\mu}$ is defined in Eq. (5.1) and m_j is the magnetic spin projection onto the same z axis. For an electron with the state $|\phi_n\rangle = |1S_{1/2}\rangle$, Eq. (5.14) can also be written as follow

$$\Delta E = \langle \phi_n | \boldsymbol{\alpha} \cdot e\mathbf{A} | \phi_n \rangle, \quad (5.15)$$

where $\mathbf{A} = (\mathbf{B} \times \mathbf{r})/2$. Eq. (5.15) explaining the deviation of the bound-electron g factor

Table 5.2: The bound-electron g -factor results for Hydrogen-like atom. The results in the first column are based on the evaluation of Eq. (5.14). The results in the second column are relied on the evaluation of Eq. (C.23) or Eq. (C.27). Z and α are the nuclear charge and the fine constant structure.

State	relativistic correction	leading-order QED correction
$1S_{1/2}$	$2 - \frac{2}{3}(Z\alpha)^2$	$+\frac{\alpha}{\pi}$
$2S_{1/2}$	$2 - \frac{1}{6}(Z\alpha)^2$	$+\frac{\alpha}{\pi}$
$2P_{1/2}$	$\frac{2}{3} - \frac{1}{6}(Z\alpha)^2$	$-\frac{\alpha}{3\pi}$
$2P_{3/2}$	$\frac{4}{3} - \frac{2}{15}(Z\alpha)^2$	$+\frac{\alpha}{3\pi}$

from the Dirac value leads to the Breit result,

$$g_j = 2 \left[\frac{1 + 2\sqrt{1 - (Z\alpha)^2}}{3} \right], \quad (5.16)$$

where Z and α are nuclear charge and fine-structure constant. Eq. (5.16) shows the deviation of the g factor from the Dirac prediction (*i.e.*, in the limit $Z\alpha \rightarrow 0$, $g_{\text{Dirac}} = 2$). This deviation is only because of the binding effects ($Z\alpha$). We apply this method for the determination of the relativistic binding corrections to the bound-electron g factor for different states and list the results in Table 5.2. More details of derivation of these results are introduced in Appendix. C. These results are valuable in the theoretical considerations of the two proposals for determining the g factor of ${}^4\text{He}^+$ ion in its ground state, which will be discussed in the next section.

5.3 Proposal I: Double-resonance excitation setup

After studying the experimental and theoretical issues related to the bound-electron g factor in the previous section, we are prepared to deal with an important part of this thesis. In this section, we offer a proposal for a bound-electron g factor measurement in the ground state of the spinless ${}^4\text{He}^+$ ion. The proposal is based on the double-resonance, two-photon excitation arrangement, which is introduced in this section.

This excitation arrangement is expected to improve the accuracy level of measurement of g factor of ${}^4\text{He}^+$ ion in its ground state. This proposal uses the properties of the bound-electron system of spinless ${}^4\text{He}^+$ resided in a Penning trap. Let us first discuss the general idea of the proposal related the bound-electron g factor of ${}^4\text{He}^+$ ion. An overview is given in Fig. 5.3. We assume that a circularly polarized (σ_+) laser light drives transition between $1S_{1/2}(m_j = +1/2)$ and $2P_{3/2}(m_j = +3/2)$ states of ${}^4\text{He}^+$. Due to the short lifetime of the excited state $2P_{3/2}(m_j = +3/2)$, an electron decays to the ground state $1S_{1/2}(m_j = +1/2)$ with emission of fluorescence photons. Therefore, a trapped single ${}^4\text{He}^+$ ion can

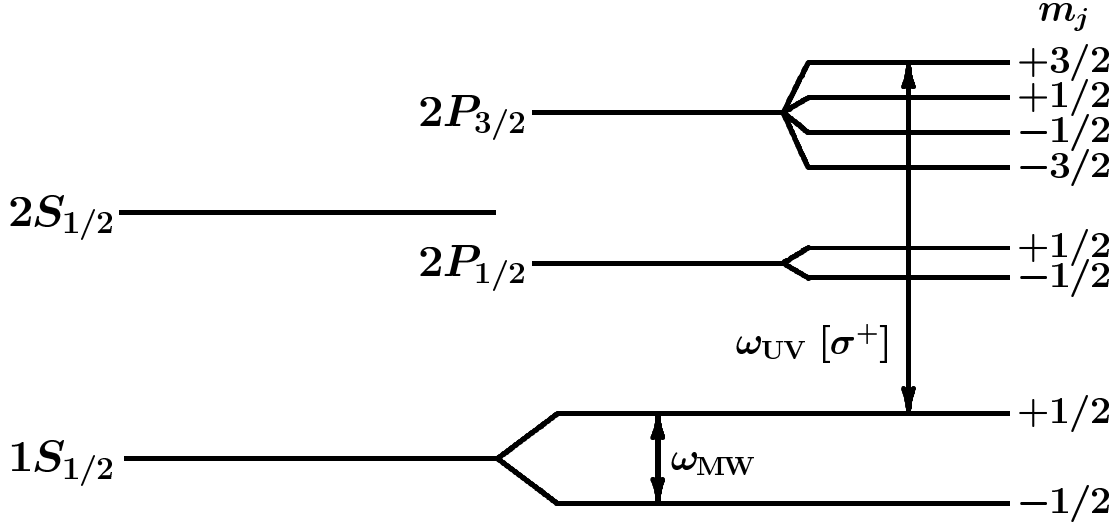


Figure 5.3: Laser-microwave double-resonance excitation scheme using circularly polarized UV light for excitation of the $1S_{1/2} \Leftrightarrow 2P_{3/2}$ transition and a microwave field for driving the spinflip transition $1S_{1/2} (m_j = +\frac{1}{2}) \Leftrightarrow 1S_{1/2} (m_j = -\frac{1}{2})$.

be optically observed in the Penning trap. The Lyman- α transition $1S_{1/2}(m_j = +1/2) - 2P_{3/2}(m_j = +3/2)$ is simultaneously accompanied by a spin-flip transition between the ground state Zeeman sub levels of 4He^+ induced by an additional microwave field. Spin-flip transition in the ground state yields the halt of fluorescence emission. This indicates that a quantum jump to $1S_{1/2}(m_j = 1/2)$ has been occurred. Further spin-flip transition restores the fluorescence intensity. Plotting the spin-flip rates (quantum jump rates) versus the microwave laser frequency results in a resonance spectrum of Larmor precession frequency, which can be associated with a bound-electron g factor.

We focus on the 4He^+ system, where the total angular momentum is equal to the total electron angular momentum \mathbf{J} (i.e. nuclear spin $\mathbf{I} = 0$). We assume that a spinless 4He^+ is in the Penning trap [see Fig. 5.2]. Due to the interaction of the magnetic field with the ion in the trap, the Zeeman splitting of the electronic ground state $1S_{1/2}$ takes place, which is given by Eq. (5.14). Likewise, due to the magnetic field, the excited state $2P_{3/2}$ is split into four Zeeman sublevels with $m_j = \pm\frac{1}{2}, \pm\frac{3}{2}$. The corresponding Landé g factor is [for details of calculations refer to Table 5.2 and Appendix. C].

$$g_j(2P_{3/2}) = \frac{4}{3} + \frac{\alpha}{3\pi} - \frac{2}{15}(Z\alpha)^2. \quad (5.17)$$

In Eq. (5.17), the leading-order QED and the relativistic contributions are taken into account.

Assuming that the 4He^+ ion in the Penning trap is in an electronic state of $1S_{1/2}$, a circularly polarized UV light with angular frequency $\omega_{\text{UV}} = 2\pi \times 9.87 \times 10^5$ Hz drives the Lyman- α transition $1S_{1/2}(m_j = +1/2) \Leftrightarrow 2P_{3/2}(m_j = +3/2)$, see Fig. 5.3. Due to

the electron relaxation to initial state $1S_{1/2}(m_j = +1/2)$ and emission of a fluorescence photon, this excitation scheme is a closed cycle (neglecting one-photon ionization into the continuum). Since $2P_{3/2}$ state has a short lifetime [see Appendix. A], the fluorescence intensity of a relaxed electron from the excited state under a saturation condition makes it possible to detect a single trapped ion with high sensitivity. The Rabi frequency between the ground state $1S_{1/2}(m_j = +1/2)$ and the excited state $2P_{3/2}(m_j = +3/2)$ induced by the narrow-band ultraviolet electromagnetic field,

$$\mathbf{E}(t) = \frac{\varepsilon_{UV}}{\sqrt{2}} \left(\cos(\omega_{UV}t) \mathbf{e}_x + \sin(\omega_{UV}t) \mathbf{e}_y \right) \quad (5.18)$$

can be found by using [23],

$$\Omega_{\text{Rabi}} = -q\varepsilon_{UV} \left\langle \phi_{1S} \left| \mathbf{x} \cdot \boldsymbol{\epsilon}_{UV} \right| \phi_{2P} \right\rangle. \quad (5.19)$$

In Eq. (5.19), the macroscopic classical amplitude of the electromagnetic field is denoted by ε_{UV} and $\boldsymbol{\epsilon}_{UV}$ refers to the polarization of the electromagnetic field and q is the electron charge. Hence the corresponding numerical value for Rabi frequency is given by $\Omega_{\text{Rabi}} = 1.3082 \times 10^7 \text{Hz} \sqrt{I_{UV}}$, where I_{UV} , intensity of the UV radiation, is measured in units of W/cm^2 .

While the Lyman- α transition $1S_{1/2}(m_j = +1/2) \Leftrightarrow 2P_{3/2}(m_j = +3/2)$ is driven by ultra-violet electromagnetic radiation, a microwave field with frequency ω_{MW} excites the ground states of Helium ion in the trap to induce the spin-flip transition. [see Fig. 5.3]. An excitation of spin-flip transition yields the instantaneous stop of the fluorescence photons. This indicates that a quantum jump has been occurred. Further spin-flip transitions between the ground states restores the fluorescence intensity. Therefore, the spin-flip rates between two Zeeman sublevels of the ground state $^4\text{He}^+$ can be counted per unit time. The resonance spectrum of the Larmor precession frequency ω_L can be thus deduced by plotting the behavior of the spin-flip rates versus excitation microwave frequency at $\omega_{\text{MW}} \approx \omega_L$ [for more discussion of the spin-flip transition see Sec. 5.2]. The cyclotron frequency ω_c , as another requirement to measure bound-electron g factor in Eq. (5.6), is obtained exactly by using the invariance theorem [see Eq. (4.61) in Sec. 4.4.1].

While the narrow-band ultraviolet electromagnetic radiation operates at the $1S_{1/2}(m_j = +1/2) \Leftrightarrow 2P_{3/2}(m_j = +3/2)$, the absorption of an additional photon can take place, resulting in ionization through the channel $2P_{3/2}(m_j = +3/2) \Rightarrow \varepsilon D_{5/2}$, where $\varepsilon D_{5/2}(m_j = 5/2)$ are electronic continuum states [see Fig. 5.4]. We therefore express the dynamic Stark shift of atomic energy of the reference states $2P_{m_j=3/2}$ as [see Sec. 2.2]

$$\begin{aligned} \Delta E_{\text{AC}}(\phi_{2P_{3/2}}) &= -\frac{e^2}{2Z^4\varepsilon_0 c} I_{UV} P_{\omega_{UV}}(\phi_{2P_{3/2}}) \\ P_{\omega_{UV}}(\phi_{2P_{3/2}}) &= \sum_{\pm} \left\langle \phi_{2P_{3/2}} \left| x^{\pm 1} \frac{1}{H_0 - E_{\phi_{2P_{3/2}}} \pm \omega_{UV}} x^{\mp 1} \right| \phi_{2P_{3/2}} \right\rangle, \end{aligned} \quad (5.20)$$

where $P_{\omega_{UV}}(\phi_{2P_{3/2}})$ is the dynamic polarizability of the Helium ion for angular frequency ω_{UV} . For this process, we obtain an ionization cross section of $1.631 \times 10^{-23} \text{cm}^2$. This leads

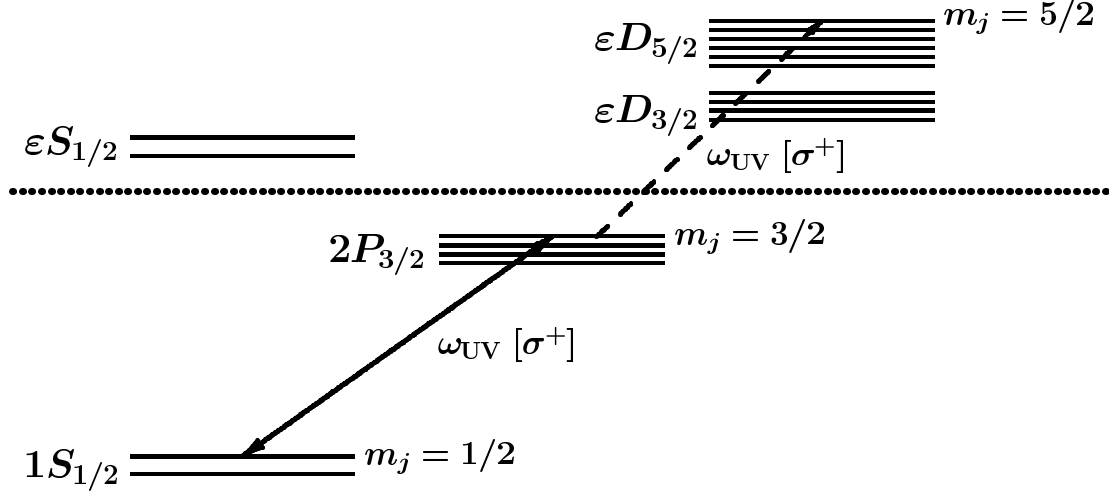


Figure 5.4: Schematic representation of the excitation scheme including ionization channels. The dotted line represents the ionization continuum threshold, and ϵL_j are electronic continuum states.

to an ionization rate of $\gamma_{\text{ioni}} = 2.495 \times 10^{-2} \text{s}^{-1} I_{\text{UV}}$, where I_{UV} is the laser intensity measured in units of W/cm^2 [for more details of calculations see Sec. 2.4]. Since the ionization rate and Rabi frequency are proportional to the intensity of the laser and its square root, respectively, it is better to work at a reduced laser intensity regime where probability of ionization of electrons is less. This results in an improvement in the population of the excited electrons in the $2P$ state of a ${}^4\text{He}^+$ ion. Nevertheless, at a typical laser intensity of $100 \text{W}/\text{cm}^2$, the lifetime of ${}^4\text{He}^+$ is 0.401s against ionization, and this has to be compared to the Rabi frequency of $1.3082 \times 10^8 \text{Hz}$. This means that the ${}^4\text{He}^+$ ion has about 10^8 Rabi cycles before its ionization. Therefore, the ionization channel does not limit the feasibility of the measurement at all.

There is a small effect, *i.e.*, AC Stark shift on the ground state Zeeman sub levels, because of the UV transition driving between $1S$ and $2P$ states. Therefore, it is important to calculate AC Stark shift of $1S - 2P$ transition due to non resonance levels. The value of AC Stark shift is $0.0968 \text{ Hz} \times I_{\text{UV}}$, where I_{UV} is given in W/cm^2 [see Sec. 2.2]. This value can be compared with the relative shift of the spin-flip transition between ground states. Since their relative shift of the spin-flip transition is a fourth-order effect, it can be neglected in comparison with the AC Stark shift of the UV transition by a factor of $\omega_{\text{L}}/\omega_{\text{UV}} < 10^{-4}$. Therefore, the shift of the spin-flip transition can be ignored on the accuracy level of 10^{-12} in units of the microwave frequency.

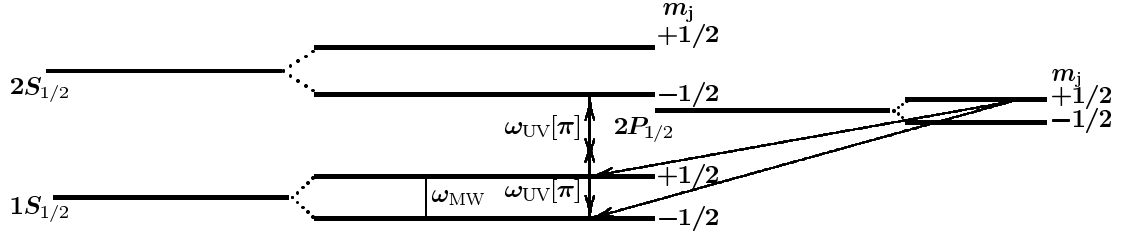


Figure 5.5: Laser-microwave double-resonance excitation scheme using π polarized UV light for excitation of the $1S_{1/2}(m_j = -\frac{1}{2}) \leftrightarrow 2S_{1/2}(m_j = -\frac{1}{2})$ transition. At the presence of the external magnetic field \mathbf{B} , $2S_{1/2}(m_j = -1/2)$ and $2P_{1/2}(m_j = +1/2)$ states are energetically degenerate. Applying the additional electric field responsible for quenching between $2S_{1/2}(m_j = -1/2)$ and $2P_{1/2}(m_j = +1/2)$ states makes them possible to decay ground state. A microwave field drives the spinflip transition $1S_{1/2}(m_j = -\frac{1}{2}) \leftrightarrow 1S_{1/2}(m_j = +\frac{1}{2})$.

5.4 Proposal II: Three-photon, double-resonance excitation setup

In Sec. 5.3, we discussed a two-photon laser spectroscopy technique for a very accurate determination of g factor of the Helium ion. In that proposal, quantum jump spectroscopy via a double-resonant, two-photon scheme in a closed cycle $1S_{1/2}(m_j = +1/2) \leftrightarrow 2P_{3/2}(m_j = +3/2)$ and microwave radiation leading the spin-flip transition between the ground state Zeeman sublevels of Helium ion result in an improved accuracy level in the measurement of the g -factor. However, building a cw laser with a wavelength of 30.37 nm to induce the quantum jump between the Zeeman sublevels (of two different electronic states) is technologically a challenge task. Our aim in this section is to propose another excitation setup in order to measure $1S$ bound-electron g factor of $^4\text{He}^+$ ion and overcome the limitations of the aforementioned approach. As opposed to the previous proposal, where a two-photon, double-resonance excitation scheme is driven by a circularly polarized laser light, in the current proposal, a three-photon, double-resonance excitation setup is operated by a linearly polarized laser light, which is explained in Ref. [88].

The general idea is schematically shown in Fig. 5.5. It is assumed that a Helium ion in the ground state $1S_{1/2}(m_j = -1/2)$ is excited to $2S_{1/2}(m_j = -1/2)$ state by absorption of two photons from a monochromatic laser light. At the same time, the magnetic field of the Penning trap and the additional electric field influence a Helium ion in the Penning trap. The magnetic field makes the two states of $2S_{1/2}(m_j = -1/2)$ and $2P_{1/2}(m_j = 1/2)$ energetically degenerate. The additional electric field is responsible for quenching of these two states. It causes the lifetime of excited state $2S_{1/2}(m_j = -1/2)$ to be reduced and decay to the ground state of Helium ion. The two-photon excitation $1S \rightarrow 2S$ along with the quenching mechanism constitutes a closed cycle. Due to the reduced lifetime of the excited state $2S_{1/2}(m_j = -1/2)$, a single Helium ion can be optically observed with a

high sensitivity in the trap. During the detection of the fluorescence photons¹, the Larmor frequency ω_L can be measured by spin-flip rates due to microwave excitation of the ground state Zeeman sublevels. After counting the number of spin-flip per unit time, plotting the spin-flip rate versus excitation microwave frequency yields the resonance spectrum of the Larmor precession frequency ω_L . This excitation arrangement relies on a quenching mechanism along with a microwave excitation that makes it possible to determine a bound-electron g factor in the Penning trap. Since three photons are involved in this excitation arrangement, we denote it as a three-photon, double-resonance excitation setup.

Similar to the previous proposal, we assume that $^4\text{He}^+$ spinless ion is stored in the Penning trap and a combination of a homogenous magnetic field with an electric quadrupole field is applied. Due to the interaction of the homogeneous magnetic field with Helium ion, the bound-electron g factor of the $2S$ state is given by (see Table 5.2 and Appendix. C)

$$g_j(2S_{1/2}) = 2 + \frac{\alpha}{\pi} - \frac{1}{6}(Z\alpha)^2 + \dots \quad (5.21)$$

In this expression, the leading-order QED and the relativistic corrections are considered. Note that the relativistic correction has a large contribution in determination of the g factor of a bound system [9]. Correspondingly, the excited state $2P_{1/2}$ becomes separated into two Zeeman sublevels with $m_j = \pm\frac{1}{2}$. The corresponding Landé g factor, following the formulation in Appendix C is [see Table 5.2]

$$g_j(2P_{1/2}) = \frac{2}{3} - \frac{\alpha}{3\pi} - \frac{1}{6}(Z\alpha)^2 + \dots \quad (5.22)$$

In this contribution, we treat $^4\text{He}^+$ spinless ion as a particle that is already in the Penning trap in the ground state $1S_{1/2}$ with magnetic spin projection $m_j = -1/2$. A monochromatic laser light with π polarization (*i.e.*, linearly polarized laser light) and wavelength of 60 nm, which is already demonstrated in Ref. [88], drives the transition between the $1S_{1/2}(m_j = -\frac{1}{2}) \Leftrightarrow 2S_{1/2}(m_j = -\frac{1}{2})$, see Fig. 5.5. As mentioned earlier, the components with $m_j = \pm 1/2$ of both $2S_{1/2}$ and $2P_{1/2}$ energy levels split as depicted in Fig. 5.7 in the presence of the magnetic field of the Penning trap. At $B = 0.752$ T, the Zeeman sublevels $2S_{1/2}(m_j = -1/2)$ and $2P_{1/2}(m_j = +1/2)$ energetically overlap. Since the quadrupole electric field of the Penning trap is not sufficient to induce a $2P_{1/2}(m_j = 1/2)$ admixture to the $2S_{1/2}(m_j = -1/2)$ state, an additional electric field in the parallel direction to the magnetic field of the Penning trap is applied [see Figs. 5.6]. This \mathbf{E} field is responsible for mixing $2S_{1/2}(m_j = -1/2)$ and $2P_{1/2}(m_j = 1/2)$ [see Figs. 5.5]. Using a numerical calculation, we have shown that this small amount of the additional electric field creates a tiny shift in the trapped particle trajectory in the Penning trap [see Fig. 4.5]. Therefore, it is safe to say that the quenching mechanism does not limit the feasibility of the measurement at all.

¹The fluorescence photons come from due to decay of the excited state $2S_{1/2}(m_j = -1/2)$ to the ground state.

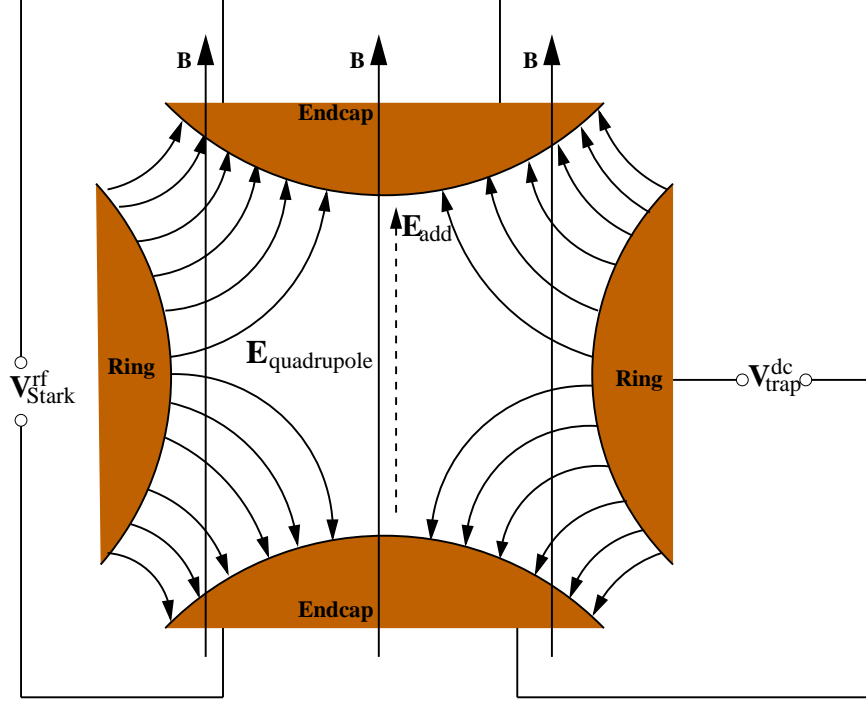


Figure 5.6: The schematic representation of the configuration of the magnetic and quadrupole electrostatic field lines along with an additional electric field in the penning trap.

Due to this mixing, the width of the metastable $2S_{1/2}(m_j = -1/2)$, Γ , in frequency units of electric field \mathbf{E} is proportional to the electric field strength (for more details of calculation see Appendix. A).

$$h^{-1}\Gamma\left[2S_{1/2}(m_j = -\frac{1}{2})\right] = 83.823 \text{ Hz} + 84.135 E^2 \text{ Hz}. \quad (5.23)$$

Since we are working in natural units, the factor h for the conversion to S.I. units is considered. In Eq. (5.23), the first term refers to two-photon decay natural width of the metastable $2S$ state [89] and the second one refers to the decay width associated with the quenching effect. In this term, the electric field \mathbf{E} is measured in units of V/cm. Eq. (5.23) indicates that $2S_{1/2}(m_j = -1/2)$ state is no longer a metastable, i.e., its lifetimes is reduced and $2S_{1/2}(m_j = -1/2)$ along with $2P_{1/2}(m_j = +1/2)$ states decay to the ground state $1S_{1/2}(m_j = \pm 1/2)$ by emission of fluorescence photons [see Fig. 5.5]. Accordingly, the transition $1S_{1/2}(m_j = -1/2) \Leftrightarrow 2S_{1/2}(m_j = -1/2)$ is a closed cycle indicating, that $1S_{1/2}(m_j = -1/2) \rightarrow 2S_{1/2}(m_j = -1/2) \rightarrow 2P_{1/2}(m_j = +1/2) \rightarrow 1S_{1/2}(m_j = -1/2)$ transition occurs. Due to the decay to the initial state $1S_{1/2}(m_j = -1/2)$, the fluorescence intensity of the excited state under saturation conditions makes it possible to detect a single trapped ion with high sensitivity. Because of the interaction of π polarized UV light

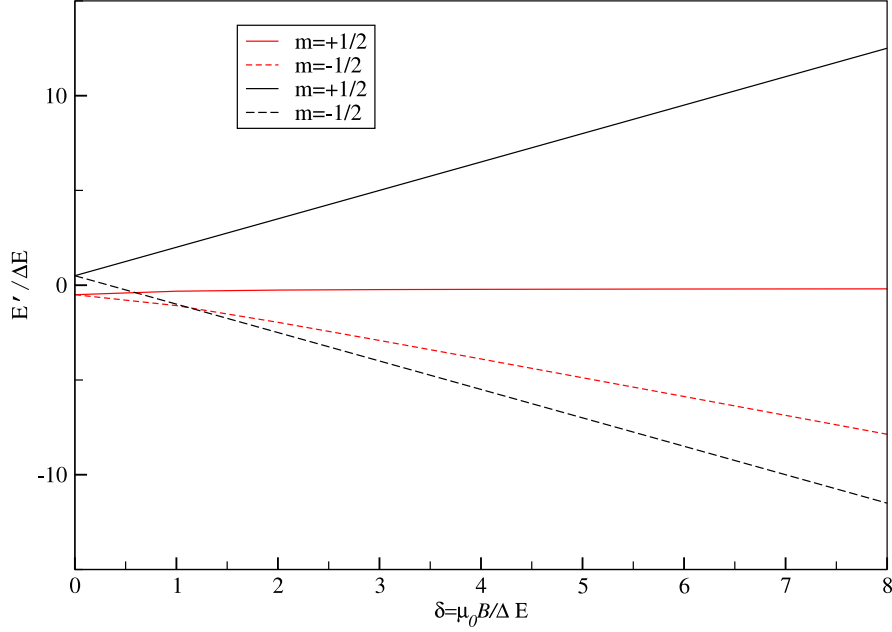


Figure 5.7: Breit-Rabi diagram for $^4\text{He}^+$ (black and red lines refer to $2S_{1/2}$ and $2P_{1/2}$ states). The intersection of the energies of pair levels at small field strengths is shown. For $m_j = \pm(l + 1/2)$, energy is linear. This behavior is no longer observed at medium and strong field strength (Paschen-Back effect). For $n = 2$, $\Delta E = 0.564 \text{ cm}^{-1}$ and δ is unity when $B = 1.209 \text{ T}$.

with the helium ion, one should consider the full, time-dependent Hamiltonian

$$\begin{aligned} H(t) &= H_0 + V(t), \\ V(t) &= -ez\varepsilon_{\text{UV}} \cos(\omega_{\text{UV}}t), \end{aligned} \quad (5.24)$$

where H_0 is the unperturbed term of the Hamiltonian and ω_{UV} are the angular frequency of the driving laser field (see Fig. 5.5). As a result of the two-photon nature of excitation process, the generalized Rabi frequency of the UV transition can be evaluated by [14]

$$\Omega_{\text{Rabi}} = 4\pi\beta I_{\text{UV}}, \quad (5.25)$$

where the time-independent two-photon transition matrix element β is obtained by

$$\beta = -\frac{1}{Z^4} \frac{e^2}{2\hbar c \varepsilon_0} \left\langle \phi_{1S_{1/2}} \left| z \frac{1}{H_0 - E + \omega} z \right| \phi_{2S_{1/2}} \right\rangle, \quad (5.26)$$

where Z is the nuclear charge of the helium ion ($Z = 2$). The corresponding numerical value of the generalized Rabi frequency is $\Omega_{\text{Rabi}} = 0.2891 I_{\text{UV}} \text{ Hz}$ indicating, that it is proportional to the laser intensity. Note that I_{UV} is assumed to be given in units of W/cm^2 .

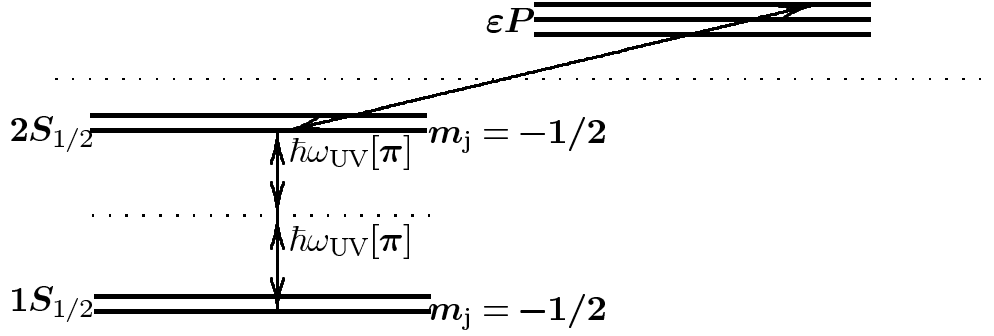


Figure 5.8: Schematic representation of the excitation scheme including ionization channel. ϵP are electronic continuum states.

During excitation of the transition $1S$ – $2S$ and detection of the corresponding fluorescence emission, a microwave field is irradiated on the ground states of Helium ion in order to induce spin-flip transition [see Fig. 5.5]. An excitation of the spin-flip transition yields the stop of the fluorescence photons. This denotes that a quantum jump to state $1S_{1/2}(m_j = 1/2)$ has taken place. The Helium ion stays in this state until a further spin-flip transition brings it back to $1S_{1/2}(m_j = -1/2)$. After plotting spin-flip rates versus the excitation microwave frequency, the resonance spectrum of Larmor frequency is obtained. The Larmor frequency ω_L along with cyclotron frequency ω_c is important inputs in Eq. (5.6) for measuring the g factor. The latter one is determined by an image-current method and the invariance theorem, which was explained in Sec. 4.4.1.

While the narrow-band ultraviolet electromagnetic radiation drives the transition $1S_{1/2}(m_j = -1/2) \Leftrightarrow 2S_{1/2}(m_j = -1/2)$ the absorptions of an additional photon can cause ionization through the channel $2S \Rightarrow \epsilon P$ (ϵP are electronic continuum states), which results in losing the ion from the trap [see Fig. 5.8]. This could be one of the most important drawbacks in this excitation setup. We therefore express the dynamic Stark shift of reference state $2S$ [see Eq. (5.24)] [14],

$$\Delta E_{AC}(\phi_{2S_{1/2}}) = -\frac{e^2}{2Z^4\epsilon_0 c} I_{UV} P_{\omega_{UV}}(\phi_{2S_{1/2}})$$

$$P_{\omega_{UV}}(\phi_{2S_{1/2}}) = \sum_{\pm} \left\langle \phi_{2S_{1/2}} \left| z \frac{1}{H_0 - E_{\phi_{2S_{1/2}}} \pm \hbar\omega_{UV}} z \right| \phi_{2S_{1/2}} \right\rangle, \quad (5.27)$$

where $P_{\omega_{UV}}(\phi_{2S_{1/2}})$ is the dynamic polarizability of the Helium ion for an angular frequency ω_{UV} . The imaginary part of Eq. (5.27) leads to the ionization rate and cross section [see Eq. (3.6a) and (3.6b)]. These values are evaluated, and are $\gamma_{\text{ioni}} = 0.472054 \text{ s}^{-1} I_{UV}$ and $\sigma_{\text{ioni}} = 1.5435 \times 10^{-18} \text{ cm}^2$. Here, I_{UV} is the laser intensity measured in units of W/cm^2 .

5.5 Proposal III

5.5.1 $1S$ – $2S$ transition frequency determination

The Helium ion $1S$ – $2S$ experiment can provide more stringent test of QED than the Hydrogen $1S$ – $2S$ experiment [88]. The singly charged Helium $1S$ – $2S$ experiment renders access to a measurement of the Rydberg constant and $1S$ Lamb shift. This makes possible to precisely check the validity of the quantum electrodynamics in an atom. Therefore, in order to perform a precise measurement of $1S$ – $2S$ transition frequency in Helium ion, we exploit the proposed excitation arrangement introduced in Sec. 5.4, which is applied for the bound-electron g -factor measurement in the Helium ion.

The $1S$ – $2S$ resonance can be observed by means of a Doppler-free two-photon spectroscopy by counterpropagating waves of equal frequencies. The required 60 nm laser light for this transition is induced by doubling cw light emitted by a 120 nm dye laser in a nonlinear crystal and gas jet [88]. The laser with wavelength 60 nm generated by thirteenth harmonic of a Ti:sapphire laser is measured with the help of the frequency comb technique, which is described in detail in [88]. The laser with the spectral linewidth as well as the frequency stability of about 60 Hz and 1 kHz, respectively is stabilized to an external ultrastable cavity and provides a wide comb of precisely equidistant frequencies, which associates to the modes of the laser cavity mutually phase locked. The splitting of these modes is equal to the repetition rate of the laser, which is more than 100 MHz and electronically phased locked to the radio frequency of the atomic cesium fountain clock. The repetition rate more than 100 MHz is sufficiently enough for high resolution spectroscopy. Therefore, the 60 nm laser can probe the $1S$ – $2S$ transition in $^4\text{He}^+$ ion, which characterizes the feasibility of our proposal to measuring the $1S$ – $2S$ transition frequency in the $^4\text{He}^+$ ion.

As mentioned in Sec. 5.4, the general scheme of our proposal is depicted in Fig. 5.5. We suppose that Helium ion in the ground state $1S_{1/2}$ is guided to a nozzle cooled with a liquid Helium flow-through cryostat in the vacuum chamber. A static magnetic field of a few tesla mounted around the vacuum chamber leads to the separation of Zeeman sublevels of the participating levels ($1S$ and $2S$ states). The frequency of a dye laser at 120 nm is locked to a high finesse optical resonator. This ultrastable laser light is frequency doubled, and the consequence UV radiation at 60 nm is coupled into an enhancement resonator inside the vacuum chamber for the excitation of the two-photon, Doppler-free $1S$ – $2S$ transition in $^4\text{He}^+$ ion. Therefore, cold Helium ion beams in the ground state $1S_{1/2}(m_j = -\frac{1}{2})$, which already leave the nozzle in the direction of laser beam are excited to the metastable $2S_{1/2}(m_j = -\frac{1}{2})$. These excited Helium ions are detected $l = 10$ cm downstream in a quench zone, where a small electric field \mathbf{E}_{add} mixes $2S_{1/2}(m_j = -\frac{1}{2})$ and $2P_{1/2}(m_j = \frac{1}{2})$ [see Fig. 5.5]. The quenching mechanism makes it possible to observe the emission of Lyman- α photons by a solar blind photomultiplier tube. A chopper frequently stops the 60 nm UV light. The photomultiplier is read out when the blocked UV light evades background counts. Due to the delay time τ between blocking UV light and detection of the excited ion signals, the slow $^4\text{He}^+$ ion with velocity less than l/τ can be registered by

the photomultiplier. This technique makes it possible to reduce the two main systematic effects (see below), *i.e.*, the finite transit time and the second Doppler effect, responsible for broadening and shift of energy levels in the $1S$ – $2S$ experiment of the Helium ion.

Table 5.3: Individual contributions to the $1S$ – $2S$ transition frequency for ${}^4\text{He}^+$ are listed in units of MHz. These corrections are evaluated for the two different nuclear charge radii $\langle r^2 \rangle^{1/2}$. The abbreviations used are as follows: “P.L.” stands for photon-line radiative-recoil correction, “S.E.” for a self energy correction, “E.L.” for the electron-line radiative-finite size correction, and “P.O.” for the polarization-operator radiative-finite size correction. The value of $\alpha^{-1} = 137.035\,999\,11(46)$ is the 2002 CODATA recommended value [69]. Here m and M refer to the electron and the nuclear masses, respectively.

Corrections to the f_{1S-2S} in ${}^4\text{He}^+$		$\langle r^2 \rangle^{1/2} = 1.673(1)\text{fm}$	$\langle r^2 \rangle^{1/2} = 1.680(5)\text{fm}$
Relativistic effect	$(Z\alpha)^4$	9 867 227 064.451 6	9 867 227 063.935 6
Pure recoil	$(Z\alpha)^6 m^2/M$	0.104 195 106 164 2	0.104 195 106 164 2
Radiative recoil	$(Z\alpha)^5 m^2/M$	0.097 725 444 158 5	0.097 725 444 158 5
P.L. radiative recoil	$(Z\alpha)^5 m^2/M$	0.003 260 173 283 2	0.003 260 173 283 2
Radiative recoil	$\alpha(Z\alpha)^6 m/M$	-0.015 840 953 062 1	-0.015 840 953 062 1
Leading nuclear size		-1.543 910 687 185 6	-1.556 857 470 665 7
E.L. radiative finite size		0.000 489 592 321 8	0.000 493 697 899 8
P.O. radiative finite size		-0.000 123 323 002 9	-0.000 124 357 153 6
Nuclear S.E.	$(Z^2\alpha)(Z\alpha)^4$	0.002 373 022 615 3	0.002 373 022 615 3
Total value of f_{1S-2S}		9 867 227 063.099 8	9 867 227 062.570 9

In principal, there are several systematic effects caused the observed line width of the excited state $2S_{1/2}(m_j = -1/2)$ is larger than its natural width. These systematic effects are responsible for the broadening and shift of the energy lines. The major systematic effects on determination of $1S_{1/2}(m_j = -1/2)$ – $2S_{1/2}(m_j = -1/2)$ transition frequency are mainly originated from the presence of an ultra-violet laser light, the small electric field \mathbf{E}_{add} responsible for quenching, a static magnetic field \mathbf{B} mounted around the vacuum chamber as well as the Helium ion velocity. It is clear that the contributions of these systematic effects influence on the accuracy level of the $1S_{1/2}(m_j = -1/2)$ – $2S_{1/2}(m_j = -1/2)$ transition frequency determination in the ${}^4\text{He}^+$ ion. In the following, we discuss the major systematic effects related to our proposed excitation arrangement by which one may measure $1S$ – $2S$ transition frequency in the ${}^4\text{He}^+$ ion.

- *Finite transit time.* Since the metastable ${}^4\text{He}^+$ ion beam and the laser beam are colinear, we can expect a long interaction length, that results in a line broadening. Choosing the slowest atoms by turning the laser light frequently off with a chopper and counting signal photons that reach after a time delay τ leads to the reduction of the finite transit time broadening [90]. For the time delay between 0.5 and 1.5 ms, our estimation for the maximum finite transit time broadening is 25.16 kHz.
- *Doppler shift.* It is well known that the first Doppler effect in a two-photon transition is vanished by using counterpropagating laser beams, while the second Doppler shift

can not be suppressed [91]. In fact, the latter one shifts to lower frequency in comparison with the resonance frequency of an atom at rest and its contribution should be taken into account in a high precise measurement of $1S$ – $2S$ transition frequency. Practically, the broadening due to this systematic effect is reduced by the method explained in the case of finite transit time [90]. An upper limits for the second Doppler effect for the time delay τ between 0.5 and 1.5 ms and the two different nuclear charge radiuses are $\Delta\nu_{\max} \leq 0.242$ kHz. Here, we use the absolute transition frequencies of ${}^4\text{He}^+$ obtained in Table 5.3, which is relevant to the excitation scheme given in Fig. 5.5 [details of the calculations regarding to the relativistic and QED corrections of the absolute transition frequencies of ${}^4\text{He}^+$ are presented in appendix D].

- *AC Stark shift.* AC Stark shift, which blueshifts the $1S$ – $2S$ two-photon transition frequency linearly with intensity of the driving laser field exists for both the ground state $1S$ and excited state $2S$ [see Fig. 5.5]. The AC Stark shifts for metastable $2S_{1/2}(m_j = -1/2)$ and ground state $1S_{1/2}(m_j = -1/2)$, which are proportional to the real part of $\Delta E_{AC}(\phi)$ in Eq. (5.27) are $\beta_{AC}(2S) = 0.08745 \text{ Hz} \times I_{UV}$ and $\beta_{AC}(1S) = -0.01673 \text{ Hz} \times I_{UV}$ in a linearly polarized laser field with intensity I_{UV} (Wcm^{-2}). Since the AC Stark shifts of the ground and excited states are of the same order of magnitude and almost close to each other, the AC Stark shift of metastable $2S_{1/2}(m_j = -1/2)$ nearly compensates that of the ground state; and the final shift β_{AC} for the two-photon transition is small but considerable. This indicates that for a typical laser beam of 100 W/cm^2 , the final shift is $[\mu/m_e]^3 \beta_{AC} = 9.9203 \text{ Hz}$, where μ refers to the reduced mass. Finally, we take notice of the ionization rate of the upper level in our scheme, which is $\gamma_{\text{ioni}} = 47.2 \text{ Hz}$.
- *DC Stark shift.* DC Stark shift is due to the presence of the static electric field \mathbf{E}_{add} responsible for quenching between the $2S_{1/2}(m_j = -1/2)$ and $2P_{1/2}(m_j = 1/2)$ states [see Fig. 5.5]. For metastable $2S$ state, the linear and quadratic Stark shifts in the static electric field \mathbf{E}_{add} reads

$$\begin{aligned} E^{\text{L.S.E}} &= 1\,919 \, E_{\text{add}} \text{ kHz} \\ E^{\text{Q.S.E}} &= 0.225 \, E_{\text{add}}^2 \text{ kHz}, \end{aligned} \quad (5.28)$$

where \mathbf{E}_{add} is measured in units of mV/cm . Here, the notations of L.S.E and Q.S.E stand for linear and quadratic Stark effects, respectively. The numerical values of these two corrections for a typical value of the electric field are shown in Table 5.4.

- *Saturation effect.* Another systematic effect, which also depends on the laser intensity similar to the AC Stark shift (light shift) is the so-called saturation coefficient, β_{sat} . This coefficient is expressed in terms of the transition matrix element β_{12} introduced in Eq. (5.26), *i.e.*,

$$\beta_{\text{sat}} = 8 \left(\frac{\beta}{\Gamma_{2S}} \right)^2 \quad (5.29)$$

Table 5.4: Corrections due to Stark effect for the $1S_{1/2} \Leftrightarrow 2S_{1/2}$ transition. These values are obtained in the frame work of time-independent perturbation based on Eq. (5.28) for a typical value of an additional electric field $E_{\text{add}} = 2 \text{ mV/cm}$.

D.C. Stark shift	$1S_{1/2} \Leftrightarrow 2S_{1/2}$
Linear shift	3 838 kHz
Quadratic shift	0.9 kHz
Total shift	3 838.9 kHz

According to the natural width of the excited state $2S$ introduced in Eq. (5.23), our estimation for the saturation coefficient is $\beta_{\text{sat}} = 6.023 \times 10^{-7} I_{\text{UV}}^{-2}$. For a typical laser intensity 100 W/cm^2 , the numerical value of the Rabi frequency is about 28 Hz [see Eq. (5.26)]. Thus, for the interaction time, which is about 1 ms, the contribution of saturation effect may be ignored in our proposed excitation arrangement.

- *Magnetic field.* The magnetic field around the vacuum chamber yields a small shift of the participating states in our proposed scheme given in Fig. 3.1. This shift is essentially due to the relativistic Zeeman effect and originates from the small difference in the g factors of the electron in the two bound states, which depend on the binding energy via Eq. (5.14). Our estimation for the relativistic Zeeman shift is

$$\beta_{\text{rel.}} = \frac{\mu_0 B}{4} (Z\alpha)^2 = 745.319 B \text{ kHz/T}, \quad (5.30)$$

where the magnetic field B is measured in units of Tesla.

5.5.2 Transition frequency determination of the ground to high-Rydberg states

The methodology above could also be generalized for the $1S-n'S$ transition frequency determination, $n' \rightarrow \infty$. Lifetime of Rydberg States [see Chapter 3] varies as n'^3 . This indicates that these states have long lifetimes and are promising platforms for high-resolution spectroscopy. Consequently, $1S-n'S$ transition frequency can be measured with a much higher precision. This implies that fundamental constants, such as Rydberg constant can be determined very exactly via $1S-n'S$ transition frequency.

The idea for determination of $1S-n'S$ transition frequency in a Helium ion is the same as the previous case. By using Doppler-free, two-photon spectroscopy technique, a UV laser field, in a two-photon process, excites the Helium ion to the Rydberg state and drives the transition $1S-n'S$, $n' \rightarrow \infty$. The $1S \Leftrightarrow n'S$ ($n' \rightarrow \infty$) transition frequency of $^4\text{He}^+$ ion can be measured by Doppler-free, two-photon laser spectroscopy. Since the Rydberg atoms are very sensitive to the UV laser field, by absorption of an additional photon from the laser field, the Helium ion is rapidly ionized [see Chapter 3]. The AC

Stark shift of the initial state $1S$ state is $\beta_{AC}(1S) = -0.02148 \text{ Hz} \times I_{UV}$, where I_{UV} is the laser intensity measured in units W/cm^2 . This ionization, as indicated in Sec. 3.3, occurs through the channel $n'S \Rightarrow \varepsilon P$, $n' \rightarrow \infty$. We therefore find an ionization cross section $n'^3 \sigma_{\text{ioni}} = 6.2225 \times 10^{-18} \text{ cm}^2$ and Rabi frequency $n'^{3/2} \Omega_{\text{Rabi}} = 0.2362 \text{ Hz } I_{UV}$, where I_{UV} is the laser intensity measured in units W/cm^2 . In obtaining the ionization cross section and Rabi frequency, we use the time-dependent perturbation theory and the Z -scaling of ionization cross section and β_{if} that were introduced in Chapters 2 and 3 [see Eq. (2.44) and Eq. (3.19)].

5.6 Partial summary and tentative concluding remarks

In this chapter, an estimation of the $1S$ bound-electron g factor of $^4\text{He}^+$ spinless ion is discussed. In this regard, two experimental setups are proposed and discussed. In our theoretical considerations, substantial corrections are introduced that would correct the Dirac value of the g factor. These corrections play very important roles in testing bound-state QED. Both experiment and theory focus on the $1S$ bound-electron g -factor and the $1S$ – $2S$ transition frequency of a $^4\text{He}^+$ spinless ion (nuclear spin $I = 0$).

We express the $1S$ bound-electron g factor in terms of the QED loop expansion parameter α and the electron-nucleus interaction strength $Z\alpha$. These terms are corrections that are originated from electron self-interaction and electron interaction with an external Coulomb field. These corrections improve the accuracy of the $1S$ bound electron g factor to the 10^{-12} level and chief among them is the “ $(Z\alpha)^0$ one-loop QED correction [see Table 5.4], which is due to the uncertainty in the fine-structure constant α [85]. In addition, on this level of accuracy, one has to take into account the relativistic effects for the ratio ω_L/ω_c , which plays a crucial role in the measurement of the bound-electron g factor [see Eq. (5.6)]. To estimate the relativistic correction, as the first step, the relativistic form of the cyclotron frequency can be written as follows [76],

$$\omega_c^{\text{rel.}} = \frac{qB}{\gamma m} = \frac{1}{\gamma} \omega_c^{\text{non-rel.}}, \quad (5.31)$$

where $\gamma = (1 - v^2/c^2)^{-1/2}$ is the so-called Lorentz factor. Then, in the case of Larmor frequency ω_L , the following two cases are considered to a better extent. First, we assume that motion of an ion is parallel to the direction of the magnetic field in the Penning trap. In this case, the Larmor frequency reads [76]

$$\omega_L^{\text{rel.}} = (1 + a) \omega_c^e(\gamma) = \frac{1}{\gamma} \omega_L^{\text{non-rel.}}, \quad (5.32)$$

where $a = g/2 - 1$ is the so-called anomaly of the magnetic moment of the electron. Comparison of Eq. (5.32) with Eq. (5.31) leads to the conclusion that the amount of the displacement in the cyclotron and Larmor frequencies is the same, due to the axial motion of the ion. Hence, the ratio $\frac{\omega_L}{\omega_c}$ is independent of the axial energy of the ion motion. In the

second case, we assume that the motion of the ion is perpendicular to the magnetic field. In this case, the relativistic Larmor frequency of the electron as indicated in Ref. [76] reads

$$\omega_L^{\text{rel.}} = (1 + \gamma a) \omega_c^e(\gamma) = \frac{1}{\gamma} \omega_L^{\text{non-rel.}} + \frac{v^2}{2c^2} a \omega_L^{\text{non-rel.}}. \quad (5.33)$$

By comparing Eq. (5.33) with the relativistic cyclotron frequency $\omega_c^{\text{rel.}}$ [see Eq. (5.31)], one can see that there is a small difference in their values. However, this small difference is a critical correction in determining the bound-electron g factor. The order of this correction can be obtained in terms of the anomaly a and v^2/c^2 , which are in the order of 10^{-3} and 10^{-9} , respectively [see Eqs. (5.31 and 5.33)]. Therefore, the relativistic uncertainties of ω_L/ω_c is of the order of 10^{-12} . This leads to the fact that the relativistic correction for the ratio ω_L/ω_c has an important contribution in determining of the accuracy level of the bound-electron g factor.

In the proposed experiments, we also introduce and discuss different mechanisms for measuring the $1S$ bound-electron g factor of $^4\text{He}^+$ spinless ion (nuclear spin $I = 0$) [see Secs. 5.3 and 5.4]. The two discussed proposals are based on combination of the Penning trap and high-resolution spectroscopy techniques to study the $1S$ bound-electron g factor of $^4\text{He}^+$ ion. The first proposal is based on a double resonance, two-photon excitation setup and the other one is relied on a double-resonance, three-photon excitation arrangement. These proposals offer possibilities using which ultra-high precision-spectroscopy techniques can be applied for ultra-accurate g measurements of Hydrogen-like ions with low nuclear charge number Z . In these proposals, laser excitation among Zeeman sublevels of $^4\text{He}^+$ ion offers additional channels that might improve the accuracy level of the bound-electron g factor determination through quantum jump spectroscopy. The excitations among the Zeeman sublevels take place via absorption of one or two photon(s) from a laser field, resulting in AC Stark shift. In high-precision two-photon spectroscopy, this shift can not be suppressed and its exact value must be calculated.

In Sec. 5.3, two simultaneous radiations in the UV and microwave regions are used in the double-resonance, two-photon excitation arrangement. The first one, the UV electromagnetic radiation, is responsible for Lyman- α transition $1S_{1/2}(m_j = +1/2) \Leftrightarrow 2P_{3/2}(m_j = +3/2)$, which is a closed cycle. This is because the excited state $2P_{3/2}(m_j = +3/2)$ has a short lifetime and it decays rapidly to the ground state $1S_{1/2}(m_j = +1/2)$ by emission of a fluorescence photon. As a consequence, $^4\text{He}^+$ spinless ion can be detected with a high sensitivity in the trap. The second one, a microwave radiation, operates at $1S_{1/2}(m_j = -1/2) \Leftrightarrow 1S_{1/2}(m_j = +1/2)$ to induce a flip in the spin of the electrons. This transition yields spin-flips resulting in the resonance spectrum of Larmor frequency. The Larmor frequency together with the cyclotron frequency, which is obtained by the invariance theorem determines the $1S$ bound-electron g factor for a Helium ion.

In Sec. 5.4, a double-resonance, three-photon excitation arrangement involves two simultaneous radiations *i.e.*, the UV laser and microwave fields and an additional static electric field. In this process, at a specific value of the magnetic field of the Penning trap, the upper states $2S_{1/2}(m_j = -1/2)$ and $2P_{1/2}(m_j = 1/2)$ energetically become

degenerate. An additional static electric field is applied to quench these two states. This causes the natural lifetime of $2S_{1/2}(m_j = -1/2)$ to be reduced and decay to the ground state $1S_{1/2}(m_j = -1/2)$. At the same time, a UV laser light drives the transition $1S_{1/2}(m_j = -1/2) \rightarrow 2S_{1/2}(m_j = -1/2)$ via a two-photon transition mechanism. This two-photon excitation along with the quenching mechanism makes a closed cycle [i.e., $1S_{1/2}(m_j = -1/2) \rightarrow 2S_{1/2}(m_j = -1/2) \rightarrow 2P_{1/2}(m_j = 1/2) \rightarrow 1S_{1/2}(m_j = -1/2)$]. During this cycle, due to the reduced lifetime of the excited state $2S_{1/2}(m_j = -1/2)$, a fluorescence emission of a single Helium ion can be observed in the trap. Similar to the first proposal, a microwave radiation induces spin-flip transition between the ground state of Zeeman sub levels, yielding the resonance spectrum of Larmor frequency. The excitation-decay cycle above along with the microwave radiation makes it possible to measure the g factor of $^4\text{He}^+$ ion in a single trap.

The major drawback to measure the bound-electron g factor via a double-resonance, two-photon excitation arrangement is that a UV laser light with a wavelength of 30nm is not currently available. However, it is possible to predict a technology to support all the necessary requirements for fulfilling this experiment [85]. Experimentally, the latter proposal is more feasible than the former one, because the required UV laser driven at $1S \rightarrow 2S$ transition has been generated by a frequency comb technique operating in the ultraviolet region of the spectrum [88].

Based on these two proposals, an estimate could be made about the accuracy level of measuring $1S$ bound-electron g factor that is at the experimental accuracy level $10^{-12} \dots 10^{-13}$. Within this accuracy range, more accurate determination of the fine-structure constant and electron mass can be obtained.

In Sec. 5.5, we focus on the $1S_{1/2}(m_j = -1/2) \rightarrow 2S_{1/2}(m_j = -1/2)$ transition frequency determination in $^4\text{He}^+$ ion. The multi-photon spectroscopy technique above, i.e., three-photon, double-resonance excitation arrangement, could be applied to determine the $1S_{1/2}(m_j = -1/2) \rightarrow 2S_{1/2}(m_j = -1/2)$ transition frequency of $^4\text{He}^+$ ion.

In this case, the uncertainty of the determination $1S_{1/2}(m_j = -1/2) \rightarrow 2S_{1/2}(m_j = -1/2)$ transition frequency is restricted by the intensity-dependent frequency shift due to dynamic Stark shift, saturation effect, DC Stark shift, the first and second Doppler effects and finally the effect of magnetic field mounted on the nozzle. It was shown that these uncertainties are originated from the absorption of high power two photons from a UV laser, the effect of an additional electric field, the thermal velocity of the ions and the magnetic field. We also discuss $1S \rightarrow n'S$, $n' \rightarrow \infty$ transition, which results in a better accuracy in transition frequency measurement. For this purpose a Doppler-free, two-photon spectroscopy is used as well. The better accuracy is due to a need for laser excitation that induces a smaller AC Stark shift.

Chapter 6

General conclusion

In this thesis, the interaction of a laser light and one-electron bound systems, *e.g.*, Hydrogen-like atoms, is extensively investigated. The primary goal is to improve the accuracy of the bound-electron g factor value. To this end, we explore different platforms for increasing the precision of measuring $1S$ bound-electron g factor. In this regard, theoretical analyses of the laser light interaction with a bound-electron system as well as a Rydberg state in the high- n region have been performed in the framework of time-dependent perturbation theory to obtain the major systematic effects relevant to high-precision atomic spectroscopy in this thesis. These investigations also yield more insights into our understanding of the bound-state properties and two-photon excitation in Rydberg atom $1S-n'S$ and $2S-n'S$ transitions, $n' \rightarrow \infty$.

Studying the ultra-high resolution spectrum of one-electron bound systems is one of the most intriguing subject in physics that offers a wonderful opportunity for high precision investigations. In this regard, we used quantum mechanics tool sets to study the properties of a spinless Helium ion stored in a Penning trap and in the presence of two simultaneous radiations ultraviolet and microwave fields. Using the platform described, it makes possible to accurately determine the $1S$ bound-electron g factor and to analyze certain properties of systematic effects that impact the ultra-high-precision measurements in atomic physics. We proposed two excitation arrangements in which two- and three- photon electronic excitations are used to measure the $1S$ bound-electron g factor. In the two-photon double resonance, we investigated transition $1S_{1/2}(m_j = 1/2) \Leftrightarrow 2P_{3/2}(m_j = 3/2)$. In three-photon double resonance, we studied transitions $1S_{1/2}(m_j = -1/2) \Leftrightarrow 2S_{1/2}(m_j = -1/2)$ and $1S \Leftrightarrow n'S$, $n' \rightarrow \infty$.

In the proposed excitation arrangements, two groups of systematic effects were taken into account to precisely determine $1S$ bound-electron g factor. The first group is due to the presence of imperfections in a real Penning trap. The effect of the imperfections on the cyclotron frequency of an ion and a bound-electron g factor is extensively studied by using the invariance theorem in Chapter 4. In the second group, we dealt with systematic effects originated from the interaction of a laser and an external electric fields with a Hydrogen-like atom. These systematic effects called AC and DC Stark shifts were investigated in the framework of time-dependent and time-independent perturbation theory in Chapter 2.

Using these precise considerations, a new accuracy level for the $1S$ bound-electron g factor could be determined, which in comparison with the previous measurements [62, 73] could show about two order of magnitude improvement, *i.e.*, on the level $10^{-12} \dots 10^{-13}$ [see Secs. 5.3, 5.4]. In addition, in the $1S$ - $2S$ transition frequency determination in Helium ion, the second group of the systematic effects was considered.

In studying Rydberg states in the high- n region, due to the wiggling motion of an electron in a laser field, the dynamic Stark shift of high- n Rydberg states was exactly calculated in the framework of time-dependent perturbation theory in Chapter 3. Based on this calculation, we evaluated the AC Stark shift and transition matrix elements for $1S$ - $n'S$ and $2S$ - $n'S$, transitions $n' \rightarrow \infty$ in a unified treatment in Hydrogen-like atoms. The calculated energy shifts for initial state $1S$ and high Rydberg state $n'S$, $n' \rightarrow \infty$ served as major systematic effects in $1S$ - $n'S$, $n' \rightarrow \infty$ transition frequency determination via Doppler-free, two-photon laser spectroscopy, which was explained in Sec. 5.5 of this thesis.

With the theoretical analyses presented in this thesis, we establish two proposals which might lead to an improved measurement of the bound-electron g factor in the mid-term future. Double- and triple-resonance excitation schemes, which are unavailable for free electrons, provided additional quantum pathways by which the measurement of the g factor of a bound as opposed to a free electron can be simplified. The combination of UV and microwave radiation is crucial to our proposals. We are fortunate to be able to combine the g factor proposals with a new proposal for the measurement of the $1S$ - $2S$ absolute frequency in an ionized Helium. The details of the proposals are laid out in Secs. 5.3, 5.4 and 5.5 of this thesis.

With respect to the high- n Rydberg state, our investigation for $1S$ - $n'S$ and $2S$ - $n'S$ transitions, $n' \rightarrow \infty$ could be generalized to the other class of transitions such as $1S$ - $n'D$ and $2S$ - $n'D$, $n' \rightarrow \infty$ and envisage the quantities such as ionization of Hydrogen-like atoms. The properties of highly excited Rydberg states are considered to be useful in a host area in fundamental physics including cavity QED.

Appendix A

Quenching effect on metastable $2S_{1/2}(m_j = -\frac{1}{2})$ state

This section is dedicated to the influence of very weak field \mathbf{E} on the lifetime of $2S_{1/2}(m = -1/2)$ and $2P_{1/2}(m = +1/2)$, which are assumed to be degenerate according to Fig. 5.5. We have assumed that Stark effect is very small in comparison with the fine structure splitting, but Lamb shift can not be ignored. In the presence of the electric field \mathbf{E} , the corresponding splitting can be evaluated by using the matrix elements of the perturbing (\mathbf{E}), which connect the states $2S_{1/2}(m_j = -1/2)$ and $2P_{1/2}(m_j = +1/2)$.

$$H = \begin{pmatrix} H^{11} & H^{12} \\ H^{21} & H^{22} \end{pmatrix}. \quad (\text{A.1})$$

Here, H^{11} , H^{12} , H^{21} and H^{22} read

$$\begin{aligned} H^{11} &= H^{22} = \langle \psi_+ | z | \psi_+ \rangle = \langle \psi_- | z | \psi_- \rangle = 0, \\ H^{21} &= H^{12} = \langle \psi_+ | z | \psi_- \rangle = \langle \psi_- | z | \psi_+ \rangle \\ &= -\frac{3nm_j}{4Z} \frac{\sqrt{n^2 - (j+1/2)^2}}{j(j+1)} E. \end{aligned} \quad (\text{A.2})$$

Note that the Schrödinger-Pauli theory with spin is applied. Here ψ_+ and ψ_- refer to the Schrödinger-Pauli eigenfunctions, which can be found in Ref. [5]. Therefore, the perturbation Hamiltonian regarding Lamb shift, which is an indispensable effect in this case reads

$$H' = H + L, \quad (\text{A.3})$$

and

$$H' = \begin{pmatrix} L & -\frac{n\sqrt{n^2-1}m_j E}{Z} \\ -\frac{n\sqrt{n^2-1}m_j E}{Z} & 0 \end{pmatrix}, \quad (\text{A.4})$$

where L is the lamb shift of the S state. The eigenvalues ε and eigenfunctions H' are as follow:

$$\begin{aligned}\varepsilon &= \frac{L}{2} \pm \frac{L}{2} \sqrt{1 + \frac{4(n^2 - 1)m_j E}{Z^2 L^2}}, \\ \psi_{mix} &= a\psi_{2S_{1/2}} + b\psi_{2P_{1/2}}, \\ \frac{a}{b} &= \frac{2\eta/Z}{1 \pm \sqrt{1 + 4\eta^2/Z^2}},\end{aligned}\tag{A.5}$$

where $\eta = n\sqrt{n^2 - 1}m_j E/L$. In Eq. (A.5), there is a direct relation between two stationary states with $n = 2$ and $j = 1/2$. The energy separation of $2S_{1/2}$ state is larger than that of $2P_{1/2}$ state. Therefore, the contribution of transition matrix element from the part of the wave function of ψ_{2S} is smaller than the corresponding contribution of ψ_{2P} . Hence, the lifetime of $2S_{1/2}(m = -1/2)$ and $2P_{1/2}(m = +1/2)$ read [5].

$$\tau_{\pm}(E) = \left[1 + \left(\frac{a_{\pm}}{b_{\pm}}\right)^2\right] t_{2P},\tag{A.6}$$

where the plus sign and minus sign refer to the stationary $2P_{1/2}(m_j = +1/2)$ and $2S_{1/2}(m_j = -1/2)$, respectively. Now, one can evaluate the two following limits:

- Stark effect is much bigger than Lamb shift splitting($\eta \gg 1$):

$$\begin{aligned}\tau_{2S_{1/2}}(E, m_j = -\frac{1}{2}) &= \tau_{2P_{1/2}}(E, m_j = +\frac{1}{2}) = \\ &= 2\tau_{2P_{1/2}} = 199.4 \text{ ps}.\end{aligned}\tag{A.7}$$

- Stark effect is much smaller than Lamb shift splitting($\eta \ll 1$)

$$\tau_{2P_{1/2}}(E, m_j = +\frac{1}{2}) = 99.7 \text{ ps},\tag{A.8}$$

$$\tau_{2S_{1/2}}(E, m_j = -\frac{1}{2}) = \eta^{-2} \tau_{2P_{1/2}},\tag{A.9}$$

where $\eta = E/475(\frac{\text{V}}{\text{cm}})$.

Now one can write the above results in terms of the width in frequency units ($\frac{\Gamma}{h} = (2\pi\tau)^{-1}$)

$$\left(\frac{\Gamma}{h}\right)'_{2S_{1/2}(m_j=-1/2)} = 1597.148\eta^2 \text{ MHz}.\tag{A.10}$$

Regarding the two-photon decay natural width of the metastable $2S$ state, one can write,

$$\left(\frac{\Gamma}{h}\right)_{2S_{1/2}(m_j=-1/2)} = 83.823 \times 10^{-6} + 1597.148\eta^2 \text{ MHz}.\tag{A.11}$$

Appendix B

Breit–Rabi diagram

In the presense of an external magnetic field, the energy levels of atoms are split. In principle, the interaction between the atoms and the field can be classified into two regimes:

- Weak magnetic field leads the Zeeman effects, either normal (in atoms with no spins) or anomalous (in all atoms with an odd number of electrons).

i.e., for weak magnetic fields, it is clear that the fine-structure and hyperfine-structure levels will experience individual energy shifts which can be summarized in terms of a coupling of the total angular momentum of the electron, or of the electron plus nucleus, to the magnetic field. This is, so-to-say, the “Zeeman effect of the fine or hyperfine structure.”

- Strong field leads the Paschen-Back effect. Unlike the (weak) magnetic field, \mathbf{S} and \mathbf{L} couple more strongly to the external magnetic field than to each other.

This is the regime where the we can speak of the “fine or hyperfine structure of the Zeeman effect,” where the leading-order effect is given by the (linear) couplings of the electron or nuclear magnetic momenta to the magnetic field, but the individual components are separated from each other by frequencies which are approximately equal to the field-free fine and hyperfine structure splittings.

In the following, we intend to study the effect of the magnetic field of a Penning trap \mathbf{B} on $2P_{1/2}(m_j = \pm 1/2)$ and $2S_{1/2}(m_j = \pm 1/2)$ states conducting us to the Breit-Rabi diagram for arbitrary magnetic field \mathbf{B} , which interpolates between the above mentioned regimes. To do so, we consider following Hamiltonian in which W is considered as perturbation [5] (we have followed the notation appeared in Ref. [5])

$$\begin{aligned} H &= H_0 + \Sigma + W, \\ \Sigma &= \frac{\alpha^2 Z}{2} \langle r^{-3} \rangle \mathbf{J} \cdot \mathbf{S}, \\ W &= \mu_0 \mathbf{B} \cdot (\mathbf{J} + 2\mathbf{S}), \end{aligned} \tag{B.1}$$

where α is fine structure constant. We have used the Pauli eigenfunctions with spin in the absence of a magnetic field with inner quantum number $j = l \pm 1/2$. Hence, Hamiltonian H read

$$H = \begin{pmatrix} \frac{1}{2} + \frac{2m_j(l+1)}{2l+1}\delta & \frac{\sqrt{(l+1/2)^2 - m_j^2}}{2l+1}\delta \\ \frac{\sqrt{(l+1/2)^2 - m_j^2}}{2l+1}\delta & -\frac{1}{2} + \frac{2m_j l}{2l+1}\delta \end{pmatrix}. \quad (\text{B.2})$$

After diagonalizing H , one can obtain the following eigenvalue for the total Hamiltonian.

$$E' = \Delta E \left[m_j \delta \pm \frac{1}{2} \sqrt{1 + \frac{4m_j \delta}{2l+1} + \delta^2} \right], \quad (\text{B.3})$$

where ΔE is the magnetic field free energy and $\delta = \frac{\mu_0 B}{\Delta E}$. Fig. 5.7 shows that the energy E' is linear at (weak) magnetic field. This is no longer valid for medium field (*i.e.* Paschen-Back regime).

In the following, the magnetic field value B has been obtained provided that $2S_{1/2}(m_j = -1/2)$ and $2P_{1/2}(m_j = +1/2)$ states have been degenerated. According to Fig. 5.7, one can consider a situation where the magnetic field precisely induces a degeneracy in the energy levels,

$$\begin{aligned} E_{2S_{1/2}} + \Delta E_{2S_{1/2}}(m_j = -\frac{1}{2}) \\ = E_{2P_{1/2}} + \Delta E_{2P_{1/2}}(m_j = +\frac{1}{2}) \end{aligned} \quad (\text{B.4})$$

Using Eq. (5.14) and regarding the lamb shifts of the $2S_{1/2}$ and $2P_{1/2}$ states in $^4\text{He}^+$ [92], one can evaluate the experimental value of the magnetic field which is $B_{\text{exp}} = 0.752$ T.

Appendix C

Calculation of relativistic and leading order QED contributions to bound-electron g factor

In this section, we try to calculate relativistic and leading order QED contributions to the g factor for $2P_j(j = \frac{1}{2}, \frac{3}{2})$ states in the presence of a homogeneous magnetic field. First, we want to evaluate the relativistic correction to the g factor. To do so, we consider the following Hamiltonian:

$$H = -e\boldsymbol{\alpha} \cdot \mathbf{A} = -e \sum_q (-1)^q \alpha_{-q} A_q, \quad q = \pm 1, 0 \quad (\text{C.1})$$

where $\mathbf{A} = \frac{1}{2}(\mathbf{B} \times \mathbf{r})$. One can use the following representation:

$$A_q = -i\sqrt{2} \sum_{m_1, m_2} C_{1m_1, 1m_2}^{1q} B_{m_1} r_{m_2}. \quad m_1 = 0, m_2 = q. \quad (\text{C.2})$$

Here, we choose the z direction for the magnetic field $\mathbf{B} = B\mathbf{e}_z$. Therefore the Hamiltonian reads

$$H = ie\sqrt{2} \sum_q (-1)^q \alpha_{-q} C_{10, 1q}^{1q} B r_q, \quad (\text{C.3})$$

which can be rewritten as follows,

$$H = -ie\sqrt{2} \left[\alpha_0 C_{10, 10}^{10} B r_0 - \alpha_{-1} C_{10, 11}^{11} B r_1 - \alpha_1 C_{10, 1-1}^{1-1} B r_{-1} \right]. \quad (\text{C.4})$$

The values of Clebsch-Gordon coefficient read

$$C_{10, 10}^{10} = 0, \quad C_{10, 11}^{11} = \frac{-1}{\sqrt{2}}, \quad C_{10, 1-1}^{1-1} = \frac{1}{\sqrt{2}}. \quad (\text{C.5})$$

Now, if we put these values in the Hamiltonian, we will reach the following relation:

$$H = ieB \left[\alpha_{-1} r_1 - \alpha_1 r_{-1} \right], \quad (\text{C.6})$$

where r_{+1} , r_{-1} , α_{+1} and α_{-1} read ,

$$\begin{aligned} r_{-1} &= \sqrt{\frac{4\pi}{3}} r Y_{11}(\theta, \varphi) & r_1 &= \sqrt{\frac{4\pi}{3}} r Y_{1-1}(\theta, \varphi) \\ \alpha_{+1} &= \frac{-1}{\sqrt{2}}(\alpha_1 + i\alpha_2) & \alpha_{-1} &= \frac{1}{\sqrt{2}}(\alpha_1 - i\alpha_2), \end{aligned} \quad (\text{C.7})$$

where α_1 , α_{-1} and α_0 can be written in terms of the Pauli matrix,

$$\alpha_i = \begin{pmatrix} 0 & \sigma_i \\ \sigma_i & 0 \end{pmatrix}. \quad (\text{C.8})$$

One can summarize α_{+1} and α_{-1} as follows:

$$\alpha_{+1} = \frac{-1}{\sqrt{2}} \begin{pmatrix} 0 & \sigma_1 + i\sigma_2 \\ \sigma_1 + i\sigma_2 & 0 \end{pmatrix}, \quad (\text{C.9})$$

$$\alpha_{-1} = \frac{1}{\sqrt{2}} \begin{pmatrix} 0 & \sigma_1 - i\sigma_2 \\ \sigma_1 - i\sigma_2 & 0 \end{pmatrix}. \quad (\text{C.10})$$

Therefore, one can rewrite Eq. (C.6) in the following form:

$$H = C(r) \begin{pmatrix} 0 & (\sigma_1 - i\sigma_2)Y_{11}(\theta, \varphi) + (\sigma_1 + i\sigma_2)Y_{1-1}(\theta, \varphi) \\ (\sigma_1 - i\sigma_2)Y_{11}(\theta, \varphi) + (\sigma_1 + i\sigma_2)Y_{1-1} & 0 \end{pmatrix}, \quad (\text{C.11})$$

where $C(r) = \sqrt{\frac{4\pi}{3}} \frac{iB_e r}{\sqrt{2}}$.

The energy shift in the magnetic field \mathbf{B} can be obtained by using the following matrix element.

$$E = \langle \psi_E(r, \theta, \varphi) | H | \psi_E(r, \theta, \varphi) \rangle, \quad (\text{C.12})$$

where $\psi_E(r, \theta, \varphi)$ in the relativistic representation is defined as follow: [93]

$$\psi_{\mathbf{E}}(\mathbf{r}, \theta, \varphi) = \begin{pmatrix} f_1(r) \chi_{\kappa}^M(\theta, \varphi) \\ i f_2(r) \chi_{-\kappa}^M(\theta, \varphi) \end{pmatrix}, \quad (\text{C.13})$$

and

$$\chi_{\kappa}^{\mathbf{M}}(\theta, \varphi) = \begin{pmatrix} \frac{-\kappa}{|\kappa|} \left(\frac{\kappa+1/2-M}{2\kappa+1} \right)^{1/2} Y_{|\kappa+\frac{1}{2}|-\frac{1}{2}, M-\frac{1}{2}}(\theta, \varphi) \\ \left(\frac{\kappa+1/2+M}{2\kappa+1} \right)^{1/2} Y_{|\kappa+\frac{1}{2}|-\frac{1}{2}, M+\frac{1}{2}}(\theta, \varphi) \end{pmatrix}. \quad (\text{C.14})$$

In the special case $2P_{3/2}$ (with $\kappa = +2$ and $m_j = +3/2$), the radial part of Eq. (C.12) has the following familiar form,

$$M_{rad} = \int_0^\infty r^3 f_1(r) f_2(r) dr, \quad (\text{C.15})$$

where $f_1(r)$ and $f_2(r)$ for $\kappa = -2$ read [93]:

$$\begin{aligned} f_1(r) &= -\frac{\sqrt{j + \frac{1}{2} - \gamma}}{2\gamma} \times \left(\sqrt{j + \frac{1}{2} - \gamma} g_1(r) - \sqrt{j + \frac{1}{2} + \gamma} g_2(r) \right), \\ f_2(r) &= \frac{\sqrt{j + \frac{1}{2} - \gamma}}{2\gamma} \times \left(\sqrt{j + \frac{1}{2} + \gamma} g_1(r) - \sqrt{j + \frac{1}{2} - \gamma} g_2(r) \right). \end{aligned} \quad (\text{C.16})$$

In the above relations, $g_1(r)$ and $g_2(r)$ read

$$\begin{aligned} g_1^{N\kappa}(r) &= N_1 (2r\omega_{N\gamma})^\gamma e^{(-r\omega_{N\gamma})} L_{N-1}^{2\gamma+1}(2r\omega_{N\gamma}), \\ g_2^{N\kappa}(r) &= N_2 (2r\omega_{N\gamma})^{\gamma-1} e^{(-r\omega_{N\gamma})} L_N^{2\gamma-1}(2r\omega_{N\gamma}), \end{aligned} \quad (\text{C.17})$$

where the symbols $L_N^{2\gamma-1}$ refers to the associated Laguerre polynomials. Note that $N_1 = 0$ and $N_2 = 4\gamma \left(\frac{\varepsilon_0 \alpha Z}{|\kappa|} \right)^{3/2} / \sqrt{\Gamma(2\gamma+1)\kappa(\kappa+\gamma)}$. In Eq. (C.18), we have,

$$\begin{aligned} \omega_{N\gamma} &= \sqrt{\varepsilon_0^2 - \varepsilon_{N\gamma}^2}, \\ \omega_{0\gamma} &= \frac{\varepsilon_0}{\kappa} \sqrt{\kappa^2 - \gamma^2}, \end{aligned} \quad (\text{C.18})$$

where $\gamma = \sqrt{\kappa^2 - (\alpha Z)^2}$, $\varepsilon_0 = m$ and $\varepsilon_{0\gamma} = \frac{\varepsilon_0 \gamma}{|\kappa|}$ in atomic unit. Putting Eq. (C.17) into Eq. (C.16) leads the radial part of matrix element of Eq. (C.13).

To calculate angular part of matrix element of Eq. (C.13), the following useful relation can be applied.

$$\sigma_1 | \uparrow \rangle = | \downarrow \rangle, \sigma_2 | \uparrow \rangle = i | \downarrow \rangle, \sigma_3 | \uparrow \rangle = | \uparrow \rangle, \quad (\text{C.19})$$

$$\sigma_1 | \downarrow \rangle = | \uparrow \rangle, \sigma_2 | \downarrow \rangle = -i | \uparrow \rangle, \sigma_3 | \downarrow \rangle = -| \downarrow \rangle. \quad (\text{C.20})$$

Finally for $2P_{3/2}(m_j = +3/2)$, the g factor reads,

$$g_j(2P_{3/2}) = \frac{4}{3} - \frac{2}{15}(Z\alpha)^2. \quad (\text{C.21})$$

One can repeat the above calculation for $2P_{1/2}(m_j = +1/2)$ and reach,

$$g_j(2P_{1/2}) = \frac{2}{3} - \frac{1}{6}(Z\alpha)^2. \quad (\text{C.22})$$

The second part of this appendix is dedicated to the calculation of leading-order QED correction to the bound-electron g factor. To evaluate this correction, one has to obtain $\langle H_{\text{QED}}^{\text{L.O.}} \rangle$, where the Hamiltonian is

$$H_{\text{QED}}^{\text{L.O.}} = -\frac{\alpha}{2\pi} (\boldsymbol{\sigma} \cdot \mathbf{B}) \left(\frac{e}{2m_e} \right). \quad (\text{C.23})$$

To evaluate the expectation value of $\langle H_{\text{QED}}^{\text{L.O.}} \rangle$, we use the fact that the time averaged spin vector is the projection of the spin onto the direction of \mathbf{J} ,

$$\mathbf{S}_{\text{avg}} = \frac{\mathbf{S} \cdot \mathbf{J}}{J^2} \mathbf{J}. \quad (\text{C.24})$$

Therefore, one can obtain $\langle \boldsymbol{\sigma} \cdot \mathbf{B} \rangle$ as follows:

$$\langle \boldsymbol{\sigma} \cdot \mathbf{B} \rangle = \frac{B}{2} \frac{j(j+1) - l(l+1) + S(S+1)}{j(j+1)} m_j. \quad (\text{C.25})$$

As a result, the leading order of QED correction to the bound-electron g factor is

$$\begin{aligned} g_{\text{QED}}^{\text{L.O.}}(2P_{3/2}) &= +\frac{\alpha}{3\pi}, \\ g_{\text{QED}}^{\text{L.O.}}(2P_{1/2}) &= -\frac{\alpha}{3\pi}. \end{aligned} \quad (\text{C.26})$$

Eqs. (C.21), (C.22) and (C.26) give Eqs. (5.17) and (5.22).

We have introduced an alternative method to calculate the leading-order QED correction to the bound-electron g factor. In this method, one should evaluate the expectation value of Eq. (C.23). To do so, one has to utilize the relativistic representation of wave function defined in Eq. (C.13).

$$\begin{aligned} \langle H_{\text{QED}}^{\text{L.O.}} \rangle &= \left\langle \psi_{2P_{3/2}} \left| H_{\text{QED}}^{\text{L.O.}} \right| \psi_{2P_{3/2}} \right\rangle = \\ &= \frac{\mu_0 \alpha B}{2\pi} \left\langle \psi_{2P_{3/2}} \left| \sigma_z \right| \psi_{2P_{3/2}} \right\rangle, \end{aligned} \quad (\text{C.27})$$

where $H_{\text{QED}}^{\text{L.O.}}$ is introduced in Eq. (C.23) and σ_z is the Pauli matrix. Eq. (C.27) reads the following form which just depends on the radial part.

$$\langle H_{\text{QED}}^{\text{L.O.}} \rangle = \frac{\mu_0 \alpha B}{2\pi} \int_0^\infty r^2 \left[f_1(r)^2 - f_2(r)^2 \right] dr, \quad (\text{C.28})$$

where $f_1(r)$ and $f_2(r)$ are defined in Eq. (C.16). This integral can be easily solved. Regarding the prefactors in Eq. (C.23), one can redrive the same value for $g_{\text{QED}}^{\text{L.O.}}$ as appeared in Eq. (C.26).

Appendix D

Relativistic and QED corrections for absolute transition frequencies of ${}^4\text{He}^+$

In this appendix, we deal with the contributions of several relativistic and QED corrections, which modify the energy value of the Hydrogen-like atom given by Schrödinger equation.

We start with the most significant correction due to the relativistic effect illustrated by the Dirac equation. This correction is given by,

$$\Delta E_{\text{rel.}} = \mu \left[f(n, j) - 1 \right] - \frac{\mu^2}{2(M + m)} \left[f(n, j) - 1 \right]^2, \quad (\text{D.1})$$

where $f(n, j)$ is defined as follows:

$$f(n, j) = \left[1 + \frac{(Z\alpha)^2}{\left[n - j - \frac{1}{2} + \sqrt{\left(j + \frac{1}{2} \right)^2 - (Z\alpha)^2} \right]^2} \right]^{-1/2}. \quad (\text{D.2})$$

Here, n is the principal quantum number and m and Z refer to the mass of electron and the number of protons, respectively.

In the following, the contribution of the QED corrections are considered. The recoil corrections that are due to the displacement of the nucleus can modify the energy value of the Hydrogen-like atom. This correction is divided into the pure and radiative recoil corrections. The first part of this correction (pure recoil) comes from the exchange of photons between electron and nucleus, in which the contribution of the self-interaction is neglected. The corresponding Feynman diagram is shown in Fig. D.1. The corresponding result of this correction for nS state reads,[94]

$$\Delta E_{\text{P.R.}} = \frac{m^2}{M} \frac{(Z\alpha)^2}{n^3} \left(4 \ln 2 - \frac{7}{2} \right). \quad (\text{D.3})$$

The second part of the recoil correction, *i.e.*, the radiative recoil correction, is due to the emission and absorption by the same particle or the modification of the photon propagator



Figure D.1: Diagrams for the pure recoil correction. The wavy and dash lines denote the transverse and Coulomb photon, respectively.

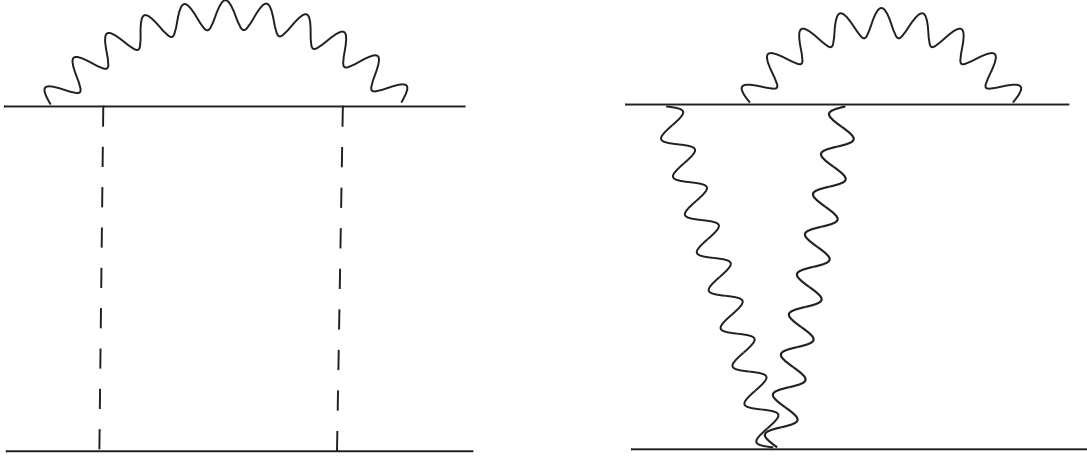


Figure D.2: Diagrams for the radiative correction.

by the the Fermi loop. The corresponding Feynman diagrams are depicted in Fig. D.2. Finally, this correction can be evaluated by the following relation [94],

$$\Delta E_{\text{R.R.}} = -\frac{\alpha(Z\alpha)^5 m^2}{Mn^3} 1.36449 \quad (\text{D.4})$$

The Finite nuclear size correction as another QED correction due to the finite size of the nuclear is [94]

$$\Delta E_{\text{F.N.}} = \frac{2}{3n^3} (Z\alpha)^4 \mu^3 \langle r^2 \rangle, \quad (\text{D.5})$$

where $\langle r^2 \rangle$ denotes the nuclear charge radius. The nuclear self-energy correction is also [94]

$$\Delta E_{\text{S.E.}} = \frac{4\mu^3}{3\pi n^3 M^2} (Z^2\alpha)(Z\alpha)^4 \left[\ln \left(\frac{M}{\mu(Z\alpha)^2} \right) - \ln k_0(n) \right], \quad (\text{D.6})$$

where $\ln k_0(n)$ refers to the Bethe logarithms.

We also consider the radiative recoil induced by one-loop polarization insertions in the exchanged photon lines. The corresponding contribution of this correction is [94]

$$\Delta E = \left(\frac{2\pi^2}{9} - \frac{70}{27} \right) \frac{\alpha(Z\alpha)^5}{\pi^2 n^3} \frac{m}{M} m \delta_{l0} \quad (\text{D.7})$$

In the last part of the QED corrections, we take into account the radiative correction to the leading nuclear size effect. In fact, there are two sources for this correction. The first one is due to one-loop radiative insertions in the electron line, while the second one comes from the one-loop polarization insertions in one of the external Coulomb lines. The first correction is so-called the electron-line correction and the second one is called polarization correction. These two corrections are [94],

$$\begin{aligned} \Delta E_{\text{e-line}} &= -1.985(1) \frac{\alpha(Z\alpha)^5}{n^3} \mu^3 \langle r^2 \rangle \delta_{l0}, \\ \Delta E_{\text{pol.}} &= \frac{\alpha(Z\alpha)^5}{2n^3} \mu^3 \langle r^2 \rangle \delta_{l0}, \end{aligned} \quad (\text{D.8})$$

,respectively. All of the numerical results related to these corrections are summarized in Table 5.3, where they play an essential role in the development of the proposal introduced in Sec. 5.5.1.

Appendix E

Publication

W. Quint, B. Nikoobakht and U. D. Jentschura,
Double-resonance g -factor measurements by quantum jump spectroscopy,
Pis'ma v ZhETF, vol. 87, pp. 36-40.

- E.1 W. Quint, B. Nikoobakht and U. D. Jentschura,
Double-resonance g -factor measurements by quantum jump spectroscopy,
Pis'ma v ZhETF, vol. 87, pp. 36-40.

Double-resonance g -factor measurements by quantum jump spectroscopy

W. Quint, B. Nikoobakht*, U. D. Jentschura*

Gesellschaft für Schwerionenforschung (GSI), 64291 Darmstadt, Germany

*Max-Planck-Institut für Kernphysik, 69029 Heidelberg, Germany
and Institut für Theoretische Physik, Universität Heidelberg, 69120 Heidelberg, Germany

Submitted 12 November 2007

With the advent of high-precision frequency combs that can bridge large frequency intervals, new possibilities have opened up for the laser spectroscopy of atomic transitions. Here, we show that laser spectroscopic techniques can also be used to determine the ground-state g -factor of a bound electron: Our proposal is based on a double-resonance experiment, where the spin state of a ground-state electron is constantly being read out by laser excitation to the atomic L shell, while the spin flip transitions are being induced simultaneously by a resonant microwave field, leading to a detection of the quantum jumps between the ground-state Zeeman sublevels. The magnetic moments of electrons in light hydrogen-like ions could thus be measured with advanced laser technology. Corresponding theoretical predictions are also presented.

PACS: 06.20.Jr, 12.20.Ds, 13.40.Em, 14.60.Cd, 31.15.-p, 31.30.Jv

Recently, there has been a dramatic progress in the precision laser spectroscopy of atomic transitions, with uncertainties on the order of 10^{-14} for two-photon transitions in hydrogen [1] and even 10^{-17} for ultraviolet (UV) electric-quadrupole transitions in the mercury ion [2] (statistical effects led to a limitation on the order of 10^{-16} for the evaluation of the latter measurement). By contrast, microwave measurements of the bound-electron g -factor in hydrogen-like ions [3–5] have been restricted to a comparatively low level of accuracy, namely in the range of 10^{-10} , where the most accurate values have been obtained for bound electrons in hydrogen-like carbon $^{12}\text{C}^{5+}$ and oxygen $^{16}\text{O}^{7+}$ (for an introductory reviews on bound-electron g -factors and various related experimental as well as theoretical techniques, see [6–8]). It is tempting to ask if the accuracy gap between the two categories of measurements might leave room for improvement of the g -factor determination, as both measurements investigate the properties of bound electrons. More specifically, the question arises if the additional “channels” provided by laser excitation among the discrete states of the bound system, and the additional possibilities for the laser cooling of ions (following the experimental methods described in Refs. [9, 10]), can be used as auxiliary devices to improve the accuracy of the g -factor determination via quantum jump spectroscopy. We also note that double-resonance techniques for stored ions have already been shown to open up attractive experimental possibilities with re-

spect to hyperfine transitions as well as electronic and nuclear g -factors [11–13].

The bound-electron (Landé) g_j -factor for an electron bound in an ion with a spinless nucleus is the proportionality constant relating the Zeeman energy ΔE in the magnetic field B (directed along the z axis) and the Larmor precession frequency ω_L to the magnetic spin projection $m_j = -\frac{1}{2}, \frac{1}{2}$ onto that same z axis. In natural units ($\hbar = c = e_0 = 1$), we have

$$\Delta E = m_j \omega_L = m_j g_j \mu_B B, \quad (1)$$

where $\mu_B = -e/2m_e$ is the Bohr magneton, expressed in terms of the electron charge e and the electron mass m_e . Deviations from the Dirac-Breit [14] prediction $g_j(1S) = 2(1 + 2\sqrt{1 - (Z\alpha)^2})/3$ are due to quantum electrodynamics (QED), nuclear and other effects.

The purpose of this note is to answer the following question: “Is it possible to apply ultra-high precision atomic laser spectroscopy to bound-electron g -factor measurements?”. Our answer will be affirmative.

In contrast to the continuous Stern-Gerlach effect [15], and complementing a recent proposal for a high-precision measurement of the g -factor in a highly charged ion [16], the current proposal is based on a Penning trap and will be studied here in conjunction with the hydrogen-like helium ion $^4\text{He}^+$, which seems to be well suited for an experimental realization in the near future. The magnetic field strength B in the Penning trap can be calibrated via a measurement of the cyclotron

frequency ω_c of the trapped ion, and the Landé g -factor for the bound electron is determined by the relation

$$g_f = 2(Z-1) \frac{m_e}{m_{\text{ion}}} \frac{\omega_L}{\omega_c}, \quad (2)$$

where the electron-ion mass ratio m_e/m_{ion} is an external input parameter and Z is the nuclear charge number.

In a Penning trap, a single ${}^4\text{He}^+$ ion is confined by a strong homogeneous magnetic field B in the plane perpendicular to the magnetic field lines and by a harmonic electrostatic potential in the direction parallel to the field lines [17]. The three eigenmotions of a stored ion are the trap-modified cyclotron motion (frequency ω_+), the axial motion (frequency ω_z), and the magnetron motion (frequency ω_-). The free-space cyclotron frequency $\omega_c = qB/m_{\text{ion}}$ of an ion with charge q can be determined from the three eigenfrequencies by [18]

$$\omega_c^2 = \omega_+^2 + \omega_z^2 + \omega_-^2. \quad (3)$$

Experimentally, the eigenfrequencies of the stored ion can be measured by non-destructive detection of the image currents which are induced in the trap electrodes by the ion motion. Measurements on the level of $\delta\omega_c/\omega_c = 7 \cdot 10^{-12}$ are achieved [19–21] by careful anharmonicity compensation of the electrostatic trapping potential, optimizing the homogeneity and temporal stability of the magnetic field close to the Penning trap's center, and cooling the motional amplitudes of the single trapped ion to low temperatures. Further optimization of experimental techniques should make it possible to reach an accuracy of (better than) $\delta\omega_c/\omega_c = 10^{-12}$. In our proposed g -factor measurement, advantage could be taken of the fact that two frequencies of the same particle are measured simultaneously (cyclotron vs. spin-flip), whereas in a mass measurement, the cyclotron frequencies of two different particles have to be determined.

In the following, we concentrate on the ${}^4\text{He}^+$ system, where the total angular momentum is equal to the total electron angular momentum J . In the presence of the magnetic field B in the Penning trap, the Zeeman splitting of the electronic ground state $1S_{1/2}$ of the ${}^4\text{He}^+$ ion is given by Eq. (1). Correspondingly, the excited state $2P_{3/2}$ is split into four Zeeman sublevels $\Delta E = m_j g_f(2P_{3/2}) \mu_B B$, with $m_j = \pm\frac{1}{2}, \pm\frac{3}{2}$. The Landé g -factor can be obtained easily according to a modified Dirac equation which forms a basis for bound-state analysis [22]

$$g_f(2P_{3/2}) = \frac{4}{3} + \frac{\alpha}{3\pi} - \frac{2}{15} (Z\alpha)^2, \quad (4)$$

where we take into account the leading QED and relativistic contributions and use $Z = 2$ for the relativistic

term of order $(Z\alpha)^2$. Suppose now that one single ${}^4\text{He}^+$ ion in the Penning trap is prepared in the Zeeman sublevel $m_j = +\frac{1}{2}$ of the electronic ground state $1S_{1/2}$. Narrow-band UV electromagnetic radiation with σ^+ polarization and angular frequency $\omega_{\text{UV}} = 2\pi \times 9.87 \cdot 10^{15}$ Hz drives the Lyman- α transition $1S_{1/2} (m_j = +\frac{1}{2}) \leftrightarrow 2P_{3/2} (m_j = +\frac{3}{2})$, see Fig. 1. This is a closed cycle because decay by emission of a

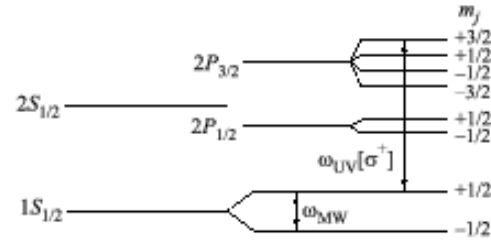


Fig. 1. Laser-microwave double-resonance excitation scheme using circularly polarized UV light for excitation of the $1S_{1/2} \leftrightarrow 2P_{3/2}$ transition and a microwave field for driving the spinflip transition $1S_{1/2} (m_j = +\frac{1}{2}) \leftrightarrow 1S_{1/2} (m_j = -\frac{1}{2})$

fluorescence photon is only possible to the initial state $1S_{1/2} (m_j = +\frac{1}{2})$ (if one ignores one-photon ionization into the continuum). Due to the short lifetime of the upper state $\tau(2P_{3/2}) \approx 99.7$ ps, the fluorescence intensity of $[2 \tau(2P_{3/2})]^{-1} \approx 5.01 \cdot 10^9$ photons/s under saturation conditions makes it possible to detect a single trapped ion with high sensitivity [23]. The Rabi frequency of the UV transition is given by $\Omega_{\text{Rabi}} = 1.308 \cdot 10^7 \text{ Hz} \sqrt{I_{\text{UV}}}$, where I_{UV} is measured in units of W/cm^2 .

Building a continuous-wave (cw) laser that operates at the Lyman- α transition of ${}^4\text{He}^+$, with a wavelength of 30.37 nm, is certainly not a trivial task. However, a cw laser operating at the corresponding Lyman- α transition for atomic hydrogen, with $\lambda = 121.56$ nm, has already been demonstrated [24]. A possible pathway is higher-harmonic generation which has recently been described in Ref. [25] and leads to a pulsed UV excitation with a high repetition rate and a potentially discontinuous probing of the Zeeman ground-state sublevel. Note that a discontinuous probing of the ground-state sublevels does not inhibit the quantum jump detection scheme as outlined below. Groundwork for a detailed analysis of the dynamics of a pulsed excitation scheme in a very much analogous atomic system has recently been laid in Ref. [26]; in principle, one only has to ensure that the light intensity of the Lyman- α source during a single laser pulse is sufficient to discern the presence or absence of fluorescence.

During excitation of the transition $1S_{1/2} (m_j = +\frac{1}{2}) \leftrightarrow 2P_{3/2} (m_j = +\frac{3}{2})$ and detection of the corresponding fluorescence photons, a microwave field with frequency ω_{MW} in resonance with the spinflip transition $1S_{1/2} (m_j = +\frac{1}{2}) \leftrightarrow 1S_{1/2} (m_j = -\frac{1}{2})$ in the electronic ground state is irradiated on the single trapped ${}^4\text{He}^+$ ion (Fig.1). Successful excitation of the spinflip transition results in an instantaneous stop of the fluorescence intensity, because the lower Zeeman level $1S_{1/2} (m_j = -\frac{1}{2})$ is not excited by the narrow-band Lyman- α radiation. A quantum jump is thus directly observed with essentially 100% detection efficiency [27]. A second spinflip $1S_{1/2} (m_j = -\frac{1}{2}) \rightarrow 1S_{1/2} (m_j = +\frac{1}{2})$ restores the fluorescence intensity. A plot of the quantum jump rate versus excitation microwave frequency at $\omega_{MW} \approx \omega_L$ yields the resonance spectrum of the Larmor precession frequency. The cyclotron frequency ω_c , which also enters Eq. (2), is measured simultaneously by non-destructive electronic detection of the image currents induced in the trap electrodes [5].

Table 1

Nuclear charge radius	$1S \leftrightarrow 2P_{3/2}$ frequency
$\langle r^2 \rangle^{1/2} = 1.673(1) \text{ fm}$	9 868 722 559.240(237) MHzs
$\langle r^2 \rangle^{1/2} = 1.680(5) \text{ fm}$	9 868 722 558.650(477) MHzs

Absolute transition frequencies of ${}^4\text{He}^+$ relevant to the excitation scheme given in Fig.1. The Zeeman splitting is excluded

While the UV laser light drives the transition $1S_{1/2} (m_j = +\frac{1}{2}) \leftrightarrow 2P_{3/2} (m_j = +\frac{3}{2})$, the absorption of an additional photon can take place, resulting in ionization through the channel $2P_{3/2} (m_j = +\frac{3}{2}) \Rightarrow \varepsilon D_{5/2} (m_j = +\frac{5}{2})$, where εD are electronic continuum states (see Fig.2). For this process, we obtain an

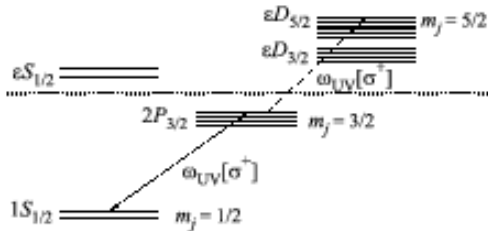


Fig.2. Schematic representation of the excitation scheme including ionization channels. The dotted line represents the ionization continuum threshold, and εD_j are electronic continuum states

ionization cross section of $1.631 \cdot 10^{-23} \text{ m}^2$. This leads to an ionization rate of $\gamma_i = 2.495 \cdot 10^{-2} \text{ s}^{-1} \times I_{UV}$, where I_{UV} is the laser intensity measured in units of W/cm^2 , corresponding to a depletion of the $2P_{3/2} (m_j = +\frac{3}{2})$ state with a time-dependent exponential $\exp(-\gamma_i t)$. Here, we use the notational conventions of Ref. [26]. In principle, since the ionization rate is proportional to the laser intensity, whereas the Rabi frequency is only proportional to its square root, it might be preferable to work at reduced laser intensities in order to increase the lifetime of the hydrogen-like charge state of the ion. However, at an incident typical laser intensity of $100 \text{ W}/\text{cm}^2$, the lifetime of ${}^4\text{He}^+$ is 0.401 s against ionization, and this has to be compared to a Rabi frequency of $1.308 \cdot 10^8 \text{ Hz}$. The ${}^4\text{He}^+$ ion has about 10^8 Rabi cycles before it is ionized, and so the ionization channel does not limit the feasibility of the measurement at all.

Finally, we take notice of the ac Stark shift of the $1S-2P$ transition due to non-resonant levels, which is $0.0968 \text{ Hz} \times I_{UV}$, with I_{UV} given in W/cm^2 . The ac Stark shift of the UV transition affects the two ground-state Zeeman levels slightly differently, but the relative shift of the spinflip transition frequency between them is a fourth-order effect and is suppressed with respect to the ac Stark shift by a factor of $\omega_L/\omega_{UV} < 10^{-4}$ and thus negligible on the level 10^{-12} in units of the microwave frequency, at a typical laser intensity of $100 \text{ W}/\text{cm}^2$. Also, experimental procedures for previous g -factor measurements [4, 5] have included an extrapolation to zero intensity of the microwave fields, and the same can be done with the driving UV laser field in the proposed measurement scheme. Alternatively, one can perform the excitation of the Lyman- α and the spinflip transitions in a time sequence, thus eliminating any systematic uncertainties of the g -factor determination related to the intensity of the UV laser light.

In order to lay a theoretical ground for the evaluation of the ${}^4\text{He}^+$ measurement, we present theoretical predictions for the transition frequencies and for the g -factor. According to the recent compilations [31–33], the ground state ${}^4\text{He}^+$ Lamb shift values are $\mathcal{L}(1S) = 107692.522(228) \text{ MHz}$ for the “old” value [34] of the nuclear charge radius $\langle r^2 \rangle^{1/2} = 1.673(1) \text{ fm}$ and $\mathcal{L}(1S) = 107693.112(472) \text{ MHz}$ for the “new” value of the charge radius [35], which is $\langle r^2 \rangle^{1/2} = 1.680(5) \text{ fm}$. (The uncertainty estimate for the “old” value has given rise to discussions, see Ref. [31].) For the $2P_{3/2}$ states, the Lamb shift is independent of the current uncertainty in the nuclear radius on the level of one kHz and reads $\mathcal{L}(2P_{3/2}) = 201.168 \text{ MHz}$ (see Tables 3 and 4 of Ref. [33]). Using a proper definition of the Lamb shift

Table 2

g -factor contribution ($^4\text{He}^+$)	
$\alpha^{-1} = 137.035\,999\,070(98)$	$\alpha^{-1} = 137.035\,999\,11(46)$
Dirac eigenvalue	
1.999 857 988 825 2(2)	1.999 857 988 825 3(9)
Finite nuclear size	
0.000 000 000 002 3	0.000 000 000 002 3
One-loop QED	$(Z\alpha)^0$
0.002 322 819 466 0(17)	0.002 322 819 465 4(76)
	$(Z\alpha)^2$
0.000 000 082 462 2	0.000 000 082 462 2
	$(Z\alpha)^4$
0.000 000 001 976 7	0.000 000 001 976 7
	h.o.,SE
0.000 000 000 035 1(2)	0.000 000 000 035 1(2)
	h.o.,VP-EL
0.000 000 000 002 0	0.000 000 000 002 0
	h.o.,VP-ML
0.000 000 000 000 2	0.000 000 000 000 2
\geq two-loop QED	$(Z\alpha)^0$
-0.000 003 515 096 9(3)	-0.000 003 515 096 9(3)
	$(Z\alpha)^2$
-0.000 000 000 124 8	-0.000 000 000 124 8
	$(Z\alpha)^4$
0.000 000 000 002 4(1)	0.000 000 000 002 4(1)
Recoil	m/M
0.000 000 029 198 5	0.000 000 029 198 5
Radiative recoil	$(m/M)^2$
-0.000 000 000 025 3	-0.000 000 000 025 3
Hadronic/weak interaction	
0.000 000 000 003 4	0.000 000 000 003 4
Total	
2.002 177 406 727 1(17)	2.002 177 406 726 5(77)

Individual contributions to the $1S$ bound-electron g -factor for $^4\text{He}^+$. In the labeling of the corrections, we follow the conventions of Ref. [28]. The abbreviations used are as follows: “h.o.” stands for a higher order contribution, “SE” for a self energy correction, “VP-EL” for the electric-loop vacuum-polarization correction, and “VP-ML” for the magnetic-loop vacuum-polarization correction. The value of $\alpha^{-1} = 137.035\,999\,070(98)$ is the currently most accurate value from Ref. [29], whereas the value of $\alpha^{-1} = 137.035\,999\,11(46)$ is the 2002 CODATA recommended value [30].

as given, e.g., in Eq. (10) of Ref. [33], we then obtain the transition frequencies as given in Table 1.

The ground-state g -factor can be described naturally in an intertwined expansion in the QED loop expansion parameter α and the electron-nucleus interaction strength $Z\alpha$ [28]. We follow the conventions of Ref. [28] and take into account all corrections that are relevant at the 10^{-12} level of accuracy (see Table 2).

The entry for the “ $(Z\alpha)^0$ one-loop QED” is just the Schwinger term $\alpha/2\pi$ and it carries the largest theoretical uncertainty, because of the uncertainty in the fine-structure constant α itself [36, 37].

In this note, we attempt to formulate a proposal by which ultra-accurate g -factor measurements in hydrogen-like systems with low nuclear charge number might be accessible to laser spectroscopic techniques. Within the next decade, it is realistic to assume that the necessary requirements for experiments will be provided that fully profit from both the electric coupling of the electron (via optical electric-dipole allowed Lyman- α transitions) and from the magnetic coupling of the electron (via spin-flip transitions among the Zeeman sub-levels of the ground state, see Fig.1). The accuracy of the measurement of the free-electron g -factor has recently been increased to a level of $7.6 \cdot 10^{-13}$ [38, 29]. Within our proposed setup, an accuracy on the level of $10^{-12} \dots 10^{-13}$ seems to be entirely realistic for bound-electron g -factors in hydrogen-like ions with a low nuclear charge number. It might be very beneficial if the extremely impressive, ultra-precise new measurement of the free-electron g -factor [29] could be supplemented by a potentially equally accurate measurement of the bound-electron g -factor in the near future, as an alternative determination of the fine-structure constant is urgently needed in conjunction with an improved determination of the electron mass.

The authors acknowledge helpful discussions with V.A. Yerokhin and K. Pachucki, and support from DFG (Heisenberg program) as well as from GSI (contract HD-JENT).

1. M. Fischer, N. Kolachevsky, M. Zimmermann et al., Phys. Rev. Lett. **92**, 230802 (2004).
2. W.H. Oskay, S.A. Diddams, E.A. Donley et al., Phys. Rev. Lett. **97**, 020801 (2006).
3. H. Häffner, T. Beier, N. Hermanspahn et al., Phys. Rev. Lett. **85**, 5308 (2000).
4. T. Beier, H. Häffner, N. Hermanspahn et al., Phys. Rev. Lett. **88**, 011603 (2001).
5. J. Verdú, S. Djekić, S. Stahl et al., Phys. Rev. Lett. **92**, 093002 (2004).
6. W. Quint, Phys. Scr. T **59**, 203 (1995).
7. T. Beier, Phys. Rep. **339**, 79 (2000).
8. S.G. Karshenboim, Phys. Rep. **422**, 1 (2005).
9. S.V. Andreev, V.I. Balykin, V.S. Letokhov, and V.G. Minogin, JETP Lett. **34**, 442 (1981); D.J. Wineland, H. Dehmelt, Bull. Am. Phys. Soc. **20**, 637 (1975).
10. V.I. Balykin, V.S. Letokhov, and A.I. Sidorov, JETP Lett. **40**, 1026 (1984).

11. W. M. Itano and D. J. Wineland, *Phys. Rev. A* **24**, 1364 (1981).
12. D. J. Wineland, J. J. Bollinger, and W. M. Itano, *Phys. Rev. Lett.* **50**, 628 (1983).
13. G. Marx, G. Tommaseo, and G. Werth, *Eur. Phys. J. D* **4**, 279 (1998).
14. G. Breit, *Nature (London)* **122**, 649 (1928).
15. N. Hermanspahn, H. Häffner, H. J. Kluge et al., *Phys. Rev. Lett.* **84**, 427 (2000).
16. V. M. Shabaev, D. A. Glazov, N. S. Oreshkina et al., *Phys. Rev. Lett.* **96**, 253002 (2006).
17. H. Dehmelt, *Rev. Mod. Phys.* **62**, 525 (1990).
18. L. S. Brown and G. Gabrielse, *Phys. Rev. A* **25**, 2423 (1982).
19. S. Rainville, J. K. Thompson, and D. E. Pritchard, *Science* **303**, 334 (2004).
20. R. S. van Dyck, Jr., S. L. Zafonte, S. Van Liew, and P. B. S. D. B. Pinegar, *Phys. Rev. Lett.* **92**, 220802 (2004).
21. W. Shi, M. Redshaw, and E. G. Myers, *Phys. Rev. A* **72**, 022510 (2005).
22. M. I. Eides, H. Grotch, and V. A. Shelyuto, *Phys. Rep.* **342**, 63 (2001).
23. The discussed excitation scheme is in principle applicable to any low- Z hydrogen-like ion with a spinless nucleus (for higher Z , it appears that the laser required to drive the $1S-2P_{3/2}$ transition is still far from experimental possibilities in the foreseeable future). Therefore, it is adequate to indicate the scaling of the relevant physical quantities for the scheme with the nuclear charge number Z . These are as follows: laser frequency: Z^2 ; Rabi frequency: Z^{-1} for constant I_{las} ; lifetime of the upper state: Z^{-4} ; AC Stark shift: Z^{-4} , again for constant I_{las} ; ionization rate coefficient: Z^{-4} , and ionization cross section: Z^{-2} . All values given in the text are for $Z = 2$.
24. K. S. E. Eikema, J. Walz, and T. W. Hänsch, *Phys. Rev. Lett.* **86**, 5679 (2001).
25. C. Gohle, T. Udem, M. Hermann et al., *Nature (London)* **436**, 234 (2005).
26. M. Haas, U. D. Jentschura, C. H. Keitel et al., *Phys. Rev. A* **73**, 052501 (2006).
27. W. Nagourney, J. Sandberg, and H. Dehmelt, *Phys. Rev. Lett.* **56**, 2797 (1986).
28. K. Pachucki, A. Czarnecki, U. D. Jentschura, and V. A. Yerokhin, *Phys. Rev. A* **72**, 022108 (2005).
29. B. Odom et al., *Phys. Rev. Lett.* **97**, 030801 (2006); G. Gabrielse et al., *Phys. Rev. Lett.* **97**, 030802 (2006); G. Gabrielse et al., *Phys. Rev. Lett.* **99**, 039902 (2007); T. Aoyama et al., e-print hep-ph/0706.3496.
30. P. J. Mohr and B. N. Taylor, *Rev. Mod. Phys.* **77**, 1 (2005).
31. A. van Wijngaarden, F. Holuj, and G. W. F. Drake, *Phys. Rev. A* **63**, 012505 (2000).
32. U. D. Jentschura and G. W. F. Drake, *Can. J. Phys.* **82**, 103 (2004).
33. U. D. Jentschura and M. Haas, *Can. J. Phys.* **85**, 531 (2007).
34. E. Borie and G. A. Rinker, *Phys. Rev. A* **18**, 324 (1978).
35. I. Sick, talk given at the PSAS-2006 conference (precision physics of simple atomic systems), Venice (June 2006) and private communication (2007). A further reevaluation of scattering data, according to I. Sick, has meanwhile revealed that the radius uncertainty could be decreased further to $\langle r^2 \rangle^{1/2} = 1.681(4)$ fm. However, in order to remain fully consistent with the tables 3 and 4 of Ref. [33], we use the more conservative uncertainty estimate of $\langle r^2 \rangle^{1/2} = 1.680(5)$ fm as given at PSAS-2006 by I. Sick. Note that the precise value of the nuclear-size correction to the transition frequency is important for our proposal only insofar as the UV laser has to be tuned to the transition $1S_{1/2} (m_j = +\frac{1}{2}) \leftrightarrow 2P_{3/2} (m_j = +\frac{3}{2})$.
36. This observation illustrates that if two g_f -factors could be measured to sufficient accuracy in the low- Z region, then the fine-structure constant could be inferred in addition to the electron mass. Namely, we would have two equations of type (2) and two unknowns: the fine-structure constant and the electron mass. See also [37].
37. U. D. Jentschura, A. Czarnecki, K. Pachucki, and V. A. Yerokhin, *Int. J. Mass Spectrometry* **251**, 102 (2006).
38. R. S. van Dyck, Jr., P. B. Schwinberg, and H. G. Dehmelt, *Phys. Rev. Lett.* **59**, 26 (1987).

Bibliography

- [1] P. A. M. Dirac in *Proceedings of The Royal Society of London Series A*, vol. CXVII, p. 610. 1928.
- [2] W. V. Houston *Phys. Rev.* **51** (1937) 446.
- [3] R. C. Williams *Phys. Rev.* **54** (1938) 558.
- [4] W. E. Lamb, JR., and R. C. Retherford *Phys. Rev.* **79** (1950) 549.
- [5] H. A. Bethe and E. E. Salpeter, *Quantum mechanics of one- and two electron atoms*. (Springer, Berlin and Academic press, New York, 1957).
- [6] T. W. Hänsch, S. A. Lee., R. Wallenstein, and C. Wieman *Phys. Rev. Lett.* **34** (1975) 307.
- [7] T. Kinoshita and L. W. B. *Phys. Rev. Lett* **47** (1981) 1573.
- [8] M. G. Boshier, P. E. G. Baird, C. J. Foot, *et al.* *Phys. Rev. A* **40** (1989) 6169.
- [9] T. Beier *et al.* *Phys. Rev. A.* **62** (2000) 032510.
- [10] G. Gabrielse *et al.* *Phys. Rev. Lett.* **97** (2006) 030802.
- [11] G. Gabrielse *et al.* *Phys. Rev. Lett.* **99** (2007) 039902.
- [12] C. Cohen-Tannoudji, R. Dupont-Roc, and G. Grynberg *Phys. Rev. A* **5** (1972) 968.
- [13] M. Haas, U. D. Jentschura, and C. H. Keitel *Am. J. Phys* **74** (2006) 77.
- [14] M. Haas *et al.* *Phys. Rev. A.* **73** (2007) 052501.
- [15] J. C. Garreau, M. Allegrini, L. Julien, and F. Biraben *J. Phys. (France)* **51** (1990) 2263.
- [16] J. C. Garreau, M. Allegrini, L. Julien, and F. Biraben *J. Phys. (France)* **51** (1990) 2275.
- [17] J. C. Garreau, M. Allegrini, L. Julien, and F. Biraben *J. Phys. (France)* **51** (1990) 2293.

-
- [18] M. O. Scully and M. S. Zubairy, *Quantum optics*. (Cambridge university, Cambridge, U.K., 1997).
- [19] J. J. Sakurai, *Modern quantum mechanics*. (Addison-Wesley, Reading, MA, 1994).
- [20] D. H. Kobe *J. Phys. B: At. Mol. Phys* **16** (1983) 1159.
- [21] M. Fox, *Quantum optics*. (Oxford university Press Inc. New York, 2006).
- [22] E. Merzbacher, *Quantum mechanics*. (John Wiley and sons, New York, 1970).
- [23] J. Evers, U. D. Jentschura, and C. H. Keitel *Phys. Rev. A* **70** (2004) 062111.
- [24] H. Bateman, *Higher Transcendental Functions*. (McGraw– Hill, New York, 1953).
- [25] C. Schwob *et al. Phys. Rev. Lett.* **82** (1999) 4960–4963.
- [26] R. Niering *et al. Phys. Rev. Lett.* **84** (2000) 5496–5499.
- [27] B. de Beauvoir *et al. Eur. Phys. J. D* **12** (2000) 61.
- [28] D. P. Dewangan *J. Phys. B: At. Mol. Opt. Phys* **35** (2002) L427.
- [29] S. P. Goldman and W. F. Drake *Phys. Rev. Lett.* **68** (1992) 1683.
- [30] G. W. F. Drake *Phys. Rev. A.* **45** (1992) 70.
- [31] A. Poquerusse *Phys. Lett. A.* **82** (1981) 232.
- [32] U. D. Jentschura and P. J. Mohr *Phys. Rev. A* . **72** (2005) 012110.
- [33] H. Rinneberg *et al. Phys. Rev. Lett* **51** (1983) 1546.
- [34] H. Rinneberg *et al. Phys. Rev. Lett* **55** (1985) 382.
- [35] B. Bransden and C. J. Joachain, *Physics of atoms and molecules*. (Longman, 1983).
- [36] R. A. Swainson and G. W. F. Drake *J. Phys. A: Math. Gen* **24** (1991) 95.
- [37] H. Friedrich, *Theoretical Atomic Physics*. (Springer, Heidelberg, 2nd edn., 1994).
- [38] G. B. Arfken and H. J. Weber, *Mathematical Methods For Physics*. (Academic Press, New York, 4th edn, 1995).
- [39] H. Bateman, *Tabels of Integrals Transforms*. (McGraw– Hill, New York, 1953).
- [40] F. B. Hildebrand, *Advanced Calculus For Applications*,. (Prentice– Hall, Inc. Englewood cliffs, New Jersey, 1976).
- [41] Y. V. Gott, M. S. Ioffe, and V. G. Telkovskii *Nucl. Fusion, Suppl. Pt* **3** (1962) 1045.

- [42] D. E. Pritchard *Phys. Rev. Lett* **51** (1983) 1336.
- [43] W. Petrich, M. H. Anderson, J. R. Ensher, and Cornell *Phys. Rev. Lett* **74** (1995) 3352.
- [44] R. C. Thompson *Adv. At. Mol. Opt* **31** (1993) 63.
- [45] P. Aniello *arXiv:quant-ph* **0301138v2** (2003) –.
- [46] M. H. Prior and E. C. Wang *Phys. Rev. A* **16** (1977) 6.
- [47] F. M. Penning *Physica* **3** (1936) 873.
- [48] S. L. Brown and G. Gerald *Phys. Rev. Mod* **58** (1986) 233.
- [49] D. J. Wineland *Precision Measurement and Fundamental constants II* **83** (1984) 83.
- [50] G. Gräff and E. Klempt *Z. Naturforschung* **22a** (1967) 1960.
- [51] G. Gräff, F. G. Major, R. W. H. Roeder, and G. Werth *Phys. Rev. Lett* **21** (1968) 340.
- [52] H. G. Dehmelt and F. L. Walls *Phys. Rev. Lett* **21** (1968) 127.
- [53] M. H. Prior *Phys. Rev. Lett* **29** (1972) 611.
- [54] R. Van Dyck, JR, P. Ekstrom, and H. Dehmelt *Nature* **262** (1976) 776.
- [55] D. J. Wineland, R. E. Drullinger, and F. L. Walls *Phys. Rev. Lett* **40** (1978) 1639.
- [56] D. J. Wineland and M. I. Wayne *Phys. Lett. A* **82** (1981) 75.
- [57] J. J. Bollinger, J. D. Prestage, M. I. Wayne, and D. J. Wineland *Phys. Rev. Lett* **54** (1985) 54.
- [58] S. L. Gilbert, J. J. Bollinger, and D. J. Wineland *Phys. Rev. Lett* **60** (1988) 2022.
- [59] R. G. Hulet *et al. Phys. Rev. A* **37** (1988) 4544.
- [60] N. Hermanspahn *et al. Phys. Rev. Lett.* **84** (2000) 427.
- [61] T. Beier *et al. Phys. Rev. Lett.* **88** (2002) 011603.
- [62] J. Verdû *et al. Phys. Rev. Lett.* **92** (2004) 093002.
- [63] D. Hanneke, S. Fogwell, and G. Gabrielse *Phys. Rev. Lett.* **100** (2008) 120801.
- [64] A. A. Sokolov and Y. G. Pavlenko *Opt. Soc. Am* **XXII** (1967) 1.
- [65] S. L. Brown and G. Gerald *Phys. Rev. A* **25** (1982) 2423.

- [66] B. Odom, B. D’Urso, and G. Gabrielse *Phys. Rev. Lett* **97** (2006) 030801.
- [67] R. S. Van Dyck, P. B. Schwinberg, and H. G. Dehmelt *Phys. Rev. Lett.* **59** (1987) 26.
- [68] V. M. Hughes and T. Kinoshita *Rev. Mod. Phys.* **71** (1999) 133.
- [69] P. J. Mohr and B. N. Taylor *Rev. Mod. Phys.* **77** (2005) 1.
- [70] G. Werth, H. Häffner, and W. Quint *Adv. At. Mol. Opt. Phys.* **48** (2005) 191.
- [71] T. Beier *et al.* *Phys. Rev. Lett* **88** (2002) 011603.
- [72] V. A. Yekrokhin, P. Indelicato, and V. M. Shabaev *Phys. Rev. Lett* **89** (2002) 143001.
- [73] H. Häffner *et al.* *Phys. Rev. Lett* **85** .
- [74] D. J. Wineland, J. J. Bollinger, and W. M. Itano *Phys. Rev. Lett.* **50** (1983) 628.
- [75] G. Werth, H. Häffner, and W. Quint *Adv. At. Mol. Opt.* **48** (2002) 191.
- [76] H. Häffner *et al.* *Eur. Phys. J. D.* **22** (2003) 163.
- [77] S. S. Schweber, *An introduction to relativistic quantum feild theory.* (Row, Peterson and company, Evanston, IL, 1961).
- [78] P. Kusch and H. M. Foldy *Phys. Rev.* **72** (1947) 1256.
- [79] P. Kusch and H. M. Foldy *Phys. Rev.* **74** (1948) 250.
- [80] A. Czarnecki *et al.* *Can. J. Phys* **84** (2006) 453.
- [81] T. Kinoshita and M. Nio *hep-ph/0507249* .
- [82] K. Pachucki, U. D. Jentschura, and V. A. Yerokhin *Phys. Rev. Lett* **93** (2004) 150401.
- [83] U. D. Jentschura and J. Evers *Can. J. Phys.* **83** (2005) 375.
- [84] S. G. Karshenboim *Phys. Lett. A* **266** (2000) 380.
- [85] W. Quint, B. Nikoobakht, and U. D. Jentschura *Pis’ma ZhETF* **87** (2008) 36.
- [86] K. Pachucki, A. Czarnecki, U. D. Jentschura, and V. A. Yerokhin *Phys. Rev. A.* **72** (2005) 022108.
- [87] G. Breit *Nature (London)* **122** (1928) 649.
- [88] C. Gohle *et al.* *Nature (London)* **426** (2005) 234.
- [89] U. D. Jentschura *Phys. Rev. A* **69** (2000) 052118.

- [90] T. Udem, A. Huber, B. Gross, *et al.* *Phys. Rev. Lett* **79** (1997) 2646.
- [91] F. Biraben, B. Cagnac, and G. Grynberg *Phys. Rev. Lett.* **79** (1974) 643.
- [92] U. D. Jentschura and M. Haas *Can. J. Phys* **85** (2007) 531.
- [93] R. A. Swainson and W. F. Drake *J. Phys. A* **24** (1991) 79.
- [94] M. I. Eides, H. Grotch, and V. A. Shelyuto *Phys. Rep.* **342** (2001) 63.

Acknowledgments

I would like to express my gratitude to Prof. Ulrich D. Jentschura for giving me the opportunity to work on this thesis, his contagious enthusiasm for theoretical atomic physics and all the guidance over the years.

I am also very grateful that PD. Dr. W. Quint kindly agreed to act as a referee for this thesis. Many thanks for the time and effort required for this task.

Further thanks go to all people I have directly worked with them in the last years. Of special mention are Dr. Wolfgang Quint and Dr. Shumin Li for the countless and fruitful discussion providing insight and guidance. But the support from the research groups at the institute of theoretical physics in Heidelberg university and at the Max- Planck- Institute in Heidelberg should not go unmentioned.

I like to thank Dr. Andrey Surzhykov, Dr. Babak Nikoobakht and Matthias Kronenwett, who read this thesis and made many constructive comments. The last but not the least, I would like to express my deepest gratitude and appreciation to my wife and parent for their encouragements and tolerating me during my education.

I would like to acknowledge support from GSI (contract HD-JENT).